

# CLAS ANALYSIS-NOTE 2015

Cross section of the reaction

$$\gamma p \rightarrow p\pi^+\pi^-$$

from G11A run period data

*E. Golovach*

Nuclear Physics Institute of the Moscow State University

# Contents

<b>1</b>	<b>Introduction</b>	<b>3</b>
<b>2</b>	<b>g11a run period</b>	<b>3</b>
<b>3</b>	<b>Particle identification and event selection</b>	<b>4</b>
3.1	Initial fiducial cuts . . . . .	4
3.2	Energy and momentum corrections . . . . .	7
3.2.1	Momentum corrections . . . . .	9
3.2.2	Photon energy corrections . . . . .	10
3.3	Kinematic fit . . . . .	10
3.4	Photon flux . . . . .	16
<b>4</b>	<b>Monte Carlo simulation</b>	<b>17</b>
4.1	Event generator . . . . .	17
4.2	Efficiency correction and fiducial cuts . . . . .	21
<b>5</b>	<b>Cross section</b>	<b>24</b>
5.1	Cross section calculation . . . . .	24
5.2	Cross section $\alpha$ symmetry . . . . .	24
5.3	Cross section from different topologies . . . . .	24
5.4	Three pion admixture . . . . .	27
5.5	Cross section extrapolation into CLAS dead area . . . . .	28
5.5.1	Simple approach . . . . .	29
5.5.2	Model approach . . . . .	37
<b>6</b>	<b>Systematic uncertainties</b>	<b>49</b>
<b>7</b>	<b>Comparison with the available world data</b>	<b>49</b>
<b>8</b>	<b>Results</b>	<b>53</b>
8.1	1-fold differential cross sections . . . . .	53
8.2	2-fold differential cross sections . . . . .	53
<b>9</b>	<b>Conclusion</b>	<b>54</b>

# 1 Introduction

The goal of this analysis is to obtain fully integrated, 1-fold and 2-fold differential cross sections of the reaction  $\gamma p \rightarrow p\pi^+\pi^-$  in the kinematics region  $1.6 < W < 2.7$  GeV within CLAS acceptance. Attempts were performed to extrapolate certain observables into CLAS dead region and have them in the whole kinematics space.

The  $N^*$  program with CLAS detector represents an important part of efforts focused on exploration of strong interaction in the non-perturbative regime. The studies of  $N^*$  spectrum in the meson photoproduction off nucleons extend our knowledge on  $N^*$  photocouplings and enhance the capabilities for "missing" baryon states search through extraction of the reaction amplitudes under minimal model assumptions [1, 2].

The studies of the charged double pion photoproduction play an important role in this activity. Single and charged double pion channels are two major contributors in  $N^*$  excitation region. They are strongly coupled by the hadronic final state interactions. The charged double pion channel is preferable in exploration of  $N^*$  states with masses above 1.6 GeV, since many of them decay preferentially with two pion emission.

Analysis of these data with the framework of the JM reaction model [3, 4] will extend an access to essential mechanisms contributing to this complex exclusive channel. These data offer additional opportunities to explore the signals from  $3/2^+(1720)$  candidate state, which were observed for the first time in the CLAS  $\pi^+\pi^-$  electroproduction off proton [5]. Two pion photo- or electroproduction off protons is one of the most suitable reaction channels for this purpose, because CQM calculations [6] predict that "missing" states are weakly coupled to the  $\pi N$  channel, while they should have substantial decays to the final states with two pions.

Data on single and double pion photoproduction are strongly coupled by the final state interaction to channels with smaller cross sections and, therefore, may affect other channels, such as  $\eta N$ ,  $KY$ , and  $\omega N$ . Thus, the information on the reactions of single and double pion photo- and electroproduction is important for global multichannel analysis within the framework of coupled channel approaches [7].

High statistic of G11A data set allow us to obtain nine single differential and twenty four double differential cross sections in  $W$ -bins with 25 MeV width. To study resonances it is important to have cross sections in narrow bins in  $W$ , as their width should be smaller than the typical resonance width 100–300 MeV.

## 2 g11a run period

Data of g11a run period consists of runs 43490 through 44133. Electron beam energy was 4.019 GeV. This beam allowed to produce tagged photons with the energies from 1.6 to 2.6 which were directed to the LH<sub>2</sub> target. Beam current ranged from 60 to 75.1 nA.

Commissioning runs as well as the runs with special trigger configuration were excluded from the analysis. We also eliminated runs with 5.021 GeV beam energy, as the statistics of such runs is small and does not reduce statistics notably. The run log book notes were

examined and runs that had problems with DC, TOF or DAQ were also excluded. We also excluded runs which were excluded in the analysis of reaction  $\gamma p \rightarrow p\pi^+\pi^-\pi^0$  [11] with the data from the same g11a run period.

The g11a trigger required coincidence between the tagger Master OR and the CLAS Level 1 trigger. The first 40 (highest energy) tagger T-counters were enabled in the trigger, but the whole E- and T-counter planes of the tagger were kept on. Level 1 trigger required a signal from from any of the 4 start counter paddles and any of the 48 TOF paddles within a coincidence window of 150 ns. As a whole Level 1 trigger was passed if at least two CLAS sectors satisfied the above conditions (two charged track requirement). Additional requirement for the trigger was a coincidence between the tagger MOR and the start counter OR within a timing window of 15 ns.

In total g11a data set comprised  $\approx 20 \times 10^9$  triggers.

Selected run list is:

43556–43557, 43561–43571, 43574–43596, 43598–43601, 43603–43604, 43608–43626, 43629–43656, 43666, 43672, 43677–43679, 43681–43687, 43692–43710, 43718–43722, 43725, 43726, 43728–43735, 43737, 43739–43741, 43744, 43745, 43747–43749, 43751–43759, 43761–43764, 43766, 43767, 43769–43773, 43776, 43781–43794, 43796–43803, 43807–43810, 43812–43824, 43827, 43832–43846, 43851–43860, 43862–43867, 43871, 43874, 43875, 43877, 43879, 43880–43883, 43885, 43886, 43888–43892, 43894–43897, 43901–43906, 44000–44002, 44007, 44008, 44010–44012, 44014, 44017–44023, 44025, 44038, 44043–44052, 44055–44069, 44072–44079, 44080–44099, 44103–44107.

## 3 Particle identification and event selection

### 3.1 Initial fiducial cuts

As a starting point initial CMU fiducial cuts [9] were applied to the data. These fiducial cuts do not depend on momentum modulus of a particle. Selection is based on polar ( $\theta$ ) and azimuthal ( $\phi$ ) angles of a particle in laboratory frame. These cuts include hard cut in forward direction at  $\theta = 27^\circ$  and a sector-dependent cut in the backwards direction. Plots in Figs. 2,1 demonstrate distributions of  $\theta$ .vs. $\phi$  for protons and charged pions.

Another necessary cut involves removing problematic TOF paddles. Histograms in Fig. 3 show numbers of hits per TOF paddle, after dead or hot paddles has been removed. The list of removed TOFs is given in Table 1.

These cuts are considered to be preliminary. More reliable separation of the fiducial volume can be achieved by comparing experimental and simulated single particle detection efficiencies (see section 4.2).

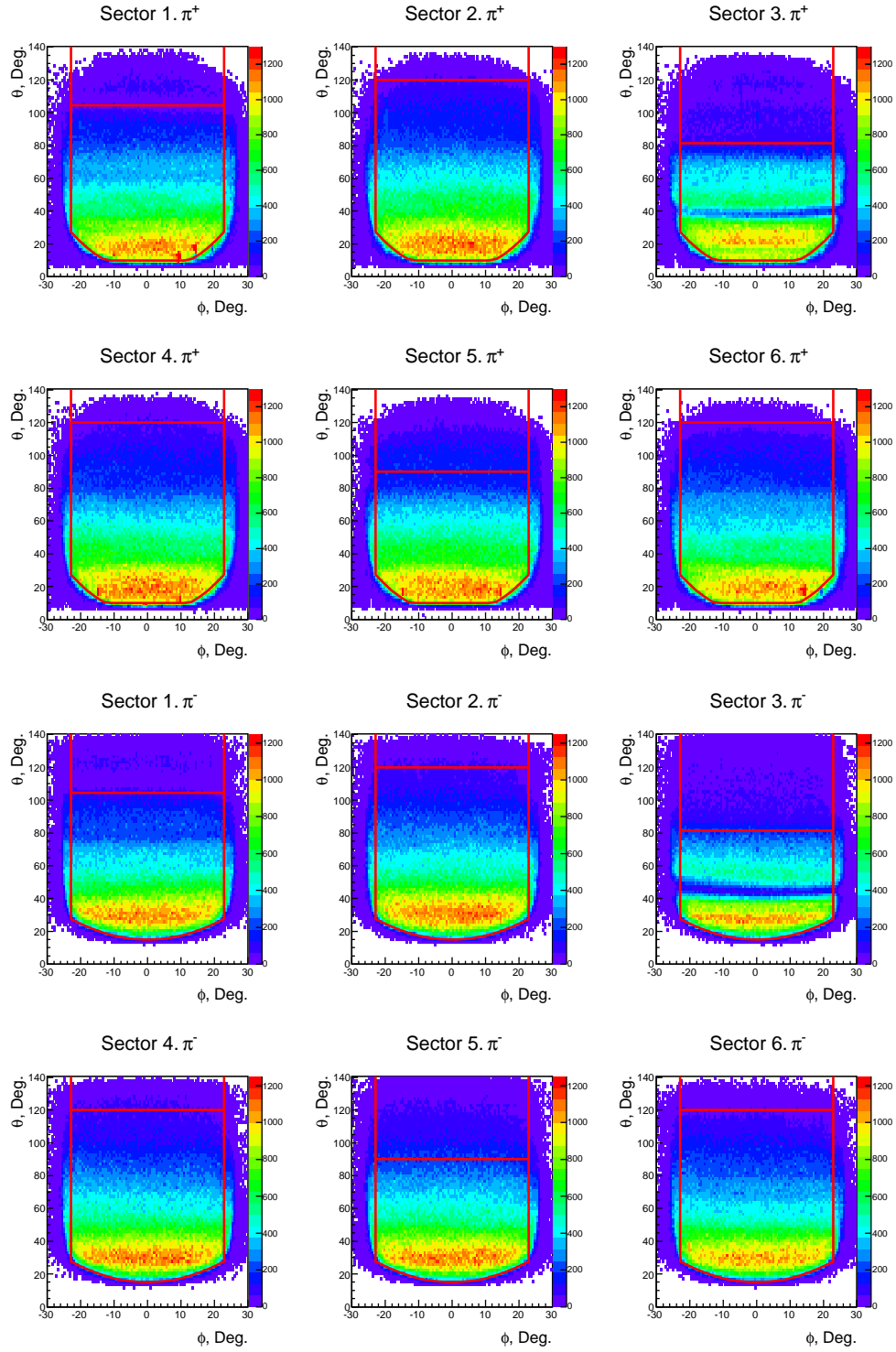


Figure 1:  $\theta$ .vs. $\phi$  distributions for pions in 6 sectors for runs 43739–43744. Initial fiducial cuts are shown in red lines.

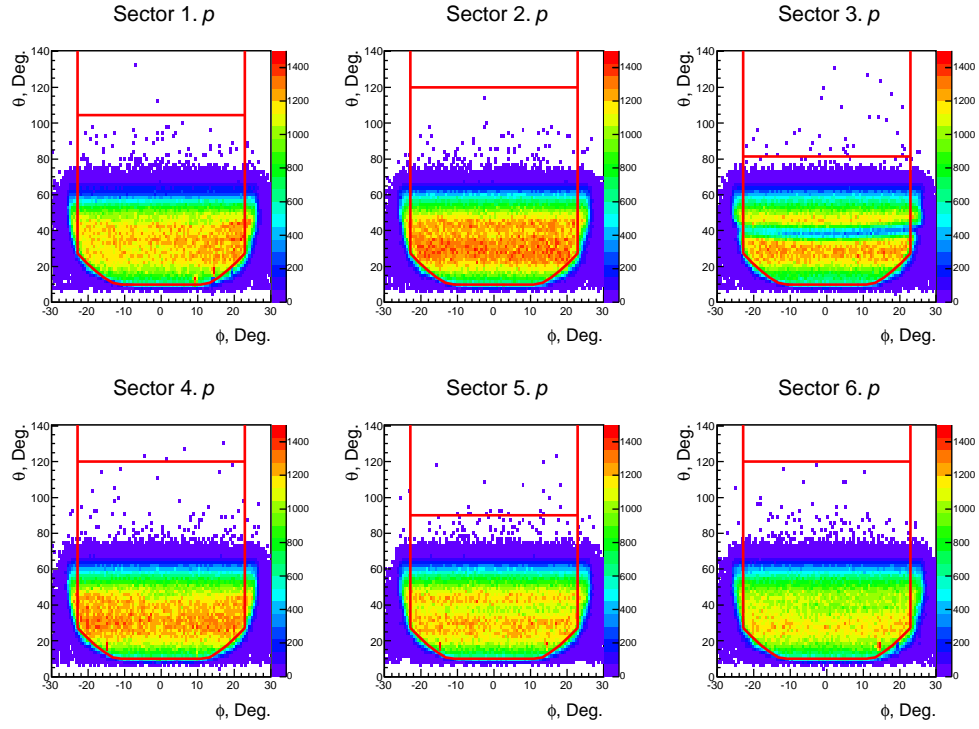


Figure 2:  $\theta$ .vs. $\phi$  distributions for protons in 6 sectors for runs 43739–43744. Initial fiducial cuts are shown in red lines.

Table 1: The list of removed TOF counters.

Sector	TOF counters
1	17, 18, 23, 26, 27, 33
2	23
3	10, 11, 23, 24, 25, 26
4	8, 23, 26
5	13, 20, 23
6	23, 25, 30

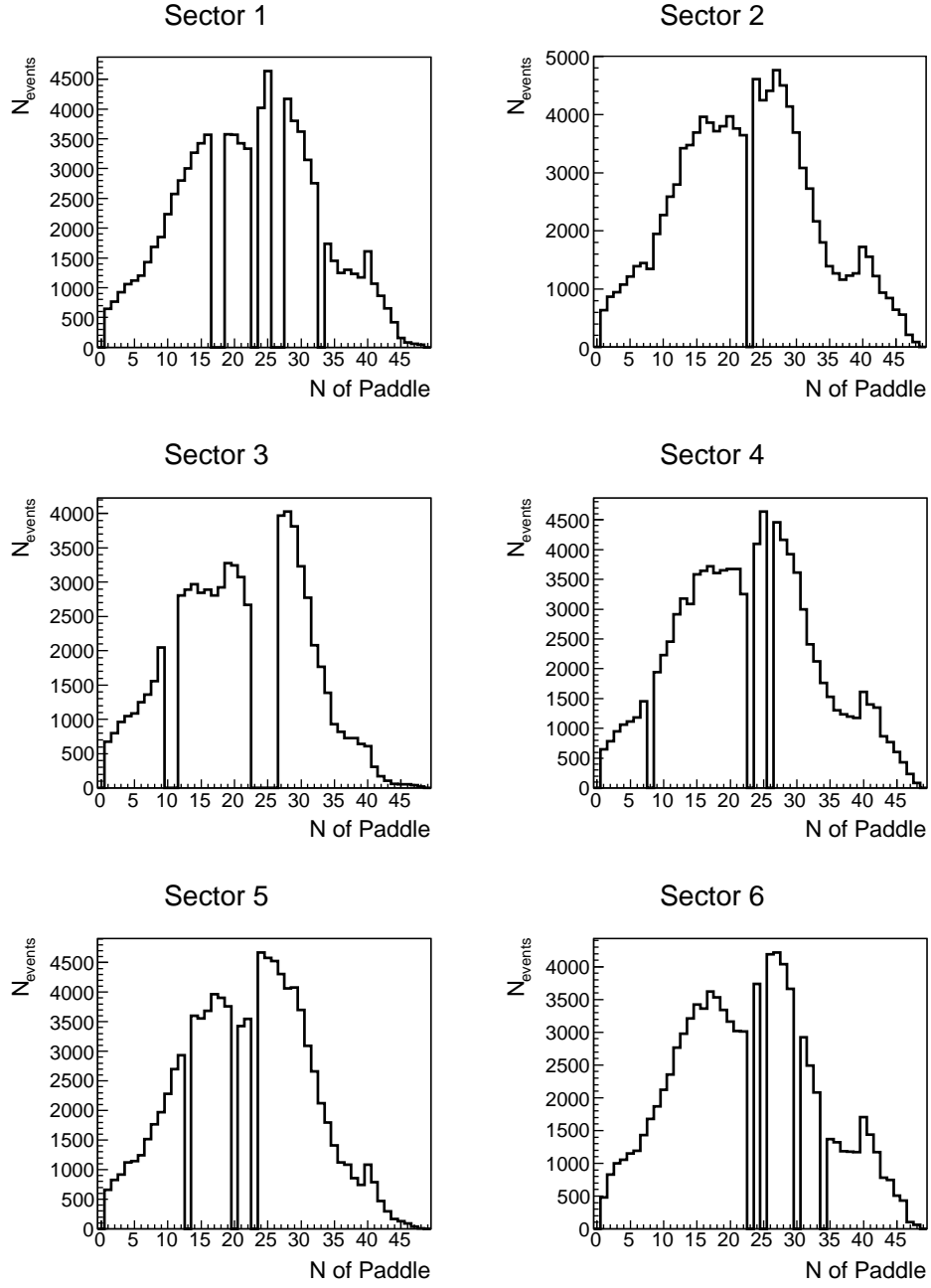


Figure 3: Number of events as a function of TOF paddle number. Dead and hot TOF counters were cut out.

### 3.2 Energy and momentum corrections

To proceed with particle identification we need firstly to correct energy of the initial photon as well as momenta of the final state particles.

To keep all corrections under control we used the standard technique of comparing the photon energy given by the tagger ( $E(t)$ ) with the same energy calculated from the reconstructed 4-momenta of the final state particles ( $E(p)$ ). For this purpose the reaction  $\gamma p \rightarrow p' \pi^+ \pi^-$  is used with requirement that all final state particles are detected.

Upper left pad (**A**) in Fig. 4 demonstrates the histogram of  $E(t)/E(p)$  versus E-counter event distributions and its projection to the  $(E(t)/E(p))$ -axis. The number of E-counter is related to the energy of a photon. One can clearly see that upper distribution (2-dim. plot) is distorted and its projection (1-dim plot) is not centered at unity.



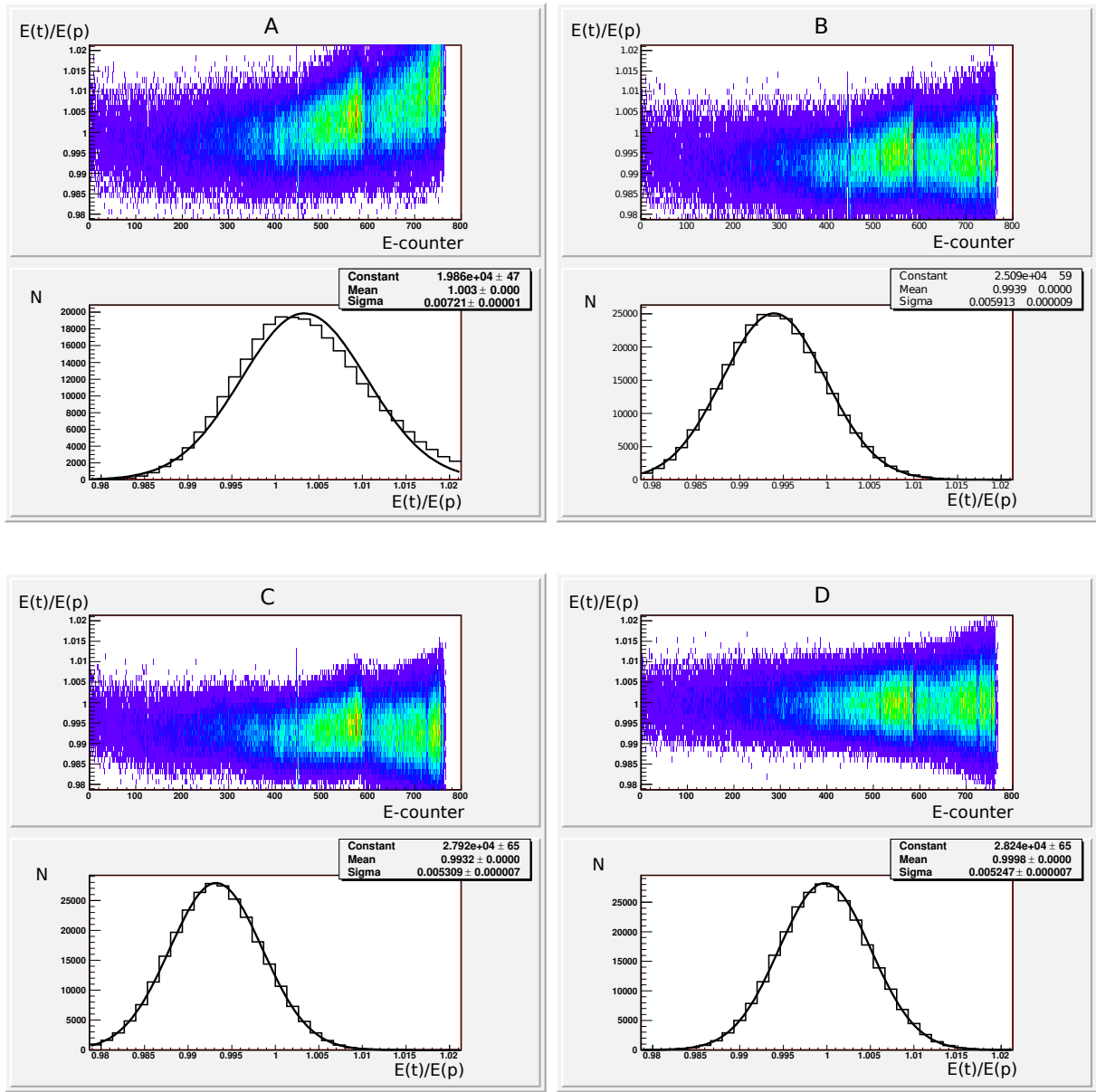


Figure 4:  $E(t)/E(p)$  versus E-counter event distributions (2-dim. plots) and their projections to the  $(E(t)/E(p))$ -axis (1-dim. plots). The plots were made in four situations: (A) no corrections had been applied (upper left pad); (B) energy loss corrections had been applied (upper right pad); (C) energy loss and momentum corrections had been applied (lower left pad); (D) photon energy corrections had been applied in addition to the previous corrections (lower right pad).

### 3.2.1 Momentum corrections

Momenta of the reconstructed charged particles were corrected for the energy loss in materials of the target assembly [14]. The standard *eloss* package was used. Plots on the upper right

pad (**B**) in Fig. 4 were made after energy loss corrections had been applied. The width of a peak of the  $E(t)/E(p)$  distribution decreased from 0.0072 to 0.0059.

Additional momentum corrections can be applied using kinematic fit [11]. They are typically less than 1%. Lower left plots (**C**) in Fig. 4 were made after both energy loss and momentum corrections had been applied. Distortion of the event distribution on the plot  $E(t)/E(p)$  versus  $E$ -counter still remains.

### 3.2.2 Photon energy corrections

Necessity for the energy corrections of tagged photons is caused by the fact that the tagger construction has been deformed with time, due to the gravitational sag. Procedure of determining of adjustments to the photon energies is described in [15] and correction factors are provided for every  $E$ -counter. Lower right plots (**D**) in Fig. 4 present distributions after photon energy as well as momentum corrections have been applied. No notable distortions of the event distribution are observed on the plot  $E(t)/E(p)$  versus  $E$ -counter. The distribution of  $E(t)/E(p)$  is centered at unity and well fit with a Gaussian function. The half width of  $E(t)/E(p)$  distribution is 0.52%. It can be expressed in terms of uncertainty as  $\Delta E/E = 0.52\%$ . This is a combined uncertainty related to the reconstruction of the initial photon energy and particle momenta.

## 3.3 Kinematic fit

Kinematic fit [11, 12] was used for event selection to isolate the reaction  $\gamma p \rightarrow p\pi^+\pi^-$ . The COBRA package [13] is used for this purpose. Kinematic fit allows to improve results of the of measurements of physical quantities by enforcing energy and momentum conservation and taking into account the errors of measurements in every event.

For the reaction  $\gamma p \rightarrow p\pi^+\pi^-$  the measured quantities are photon energy  $E_\gamma$  and momenta of particles in the final state. Using data from drift chambers the track momenta are reconstructed in terms of momentum modulus  $p$  and two angles  $\lambda$  and  $\phi$  in the sector-dependent tracking coordinate system, see [11, 12] for details. Momentum  $\vec{p}$  of a particle in the LAB frame is expressed in terms of  $p$ ,  $\lambda$ ,  $\phi$ . (In this section  $\phi$  stands for an angle in tracking coordinate system.)

The  $n$  measurable quantities are put in the vector  $y$ . They are energy  $E_\gamma$  and  $p$ ,  $\lambda$  of  $\phi$  of detected particles. The actual measured quantities and their errors are put in vectors  $\eta$  and  $\epsilon$ .

$$\eta = y + \epsilon. \quad (1)$$

There are  $r$  constraint functions for  $y$  (energy and momentum conservation), where  $r$  is equal to four in the topology, when all particles are detected and  $r$  is equal to unity, when one particle is missing. The values of  $y$  are found by least-squares fitting and vector  $y$  gives improved measurements of  $\eta$ , see [11, 12] for details.

The primary result of the kinematic fit is the value of *confidence level* (CL). Confidence

level of fit results is defined as,

$$CL = \int_{\chi^2}^{\infty} f(x; n) dx, \quad (2)$$

where  $f(z; n)$  is the  $\chi^2$  probability density function with  $n$  degrees of freedom. It is a measure of the probability that a  $\chi^2$  from the theoretical distribution is greater than the  $\chi^2$  obtained from the fit. So, CL is the measure of the *goodness* of fit. The more the value of CL, the better is the quality of the fit.

For a data set consisting of events which satisfy the fit hypothesis with normally distributed errors, the confidence level distribution is flat and ranges from zero to unity. Events that do not satisfy the fit hypothesis (*false* events) have small confidence levels. Thus, cutting events with small values of confidence level provides a way to eliminate the majority of *false* events while losing defined amount of *true* events.

For reliable usage of CL to cut *false* events the good understanding of the errors of the measured quantities is necessary. The quality of error estimation can be examined using pull distributions. The pull for the  $i$ -th fit quantity is defined as

$$z_i = \frac{\epsilon_i}{\sigma(\epsilon_i)} = \frac{\eta_i - y_i}{\sqrt{\sigma^2(\eta_i) - \sigma^2(y_i)}}, \quad (3)$$

where  $\sigma^2(y_i)$  is a standard deviation of  $y_i$  and it is found during the fit.  $z_i$  should be normally distributed around zero with standard deviation equal to unity. So, pull distribution can be used as an indicator that the errors of measured quantities were correctly estimated.

Charges and momenta of reconstructed particle were taken from the SEB bank. All negative tracks are hypothesized to be from negative pions and positive tracks from protons or positive pions. Tagger can have more than one hit in one event. All tagger hits are tried in the fit. Kinematic fit was applied to all possible topologies: all particles are detected —  $p\pi^+\pi^-(0)$ , proton is missing —  $(p)\pi^+\pi^-$ ,  $\pi^+$  is missing —  $p(\pi^+)\pi^-$  and  $\pi^-$  is missing —  $p\pi^+(\pi^-)$ . Loose cuts were applied on reconstructed missing mass before fitting:  $|M_{true} - M_{det}| < 0.3$  GeV, where  $M_{true}$  and  $M_{det}$  stand for true and reconstructed missing masses.  $M_{true}$  is equal either to zero or to the mass of proton or pion, depending on the used topology.

Pull distributions are demonstrated in Figs. 5–8. The peaks are well fitted with Gaussian. They all are centered at  $0. \pm 0.05$  and their standard standard deviations are  $1. \pm 0.1$ .

Confidence level distributions are demonstrated in Fig. 9 for both data and simulation. We use the CL cut at 0.1. Simulation included only two pion events with no background. One can see that both experimental and simulated CL distributions have sharp rise at small CL values. That tail for experimental data is supposed to be formed by *false* events. However, simulated events in ideal case should have uniform CL distributions, as there are no *false* events. Therefore, if we cut off events with  $CL < 0.1$ , then more than 10% of true events are cut off. Thus, more detailed study is required to be sure the kinematic fit cuts off the same amount of events in experimental data and in simulation. Studies in [8] give 3% systematic error on yield extractions due to mismatches of the effects of the kinematic fit between data and Monte Carlo.

Estimation of the percentage of the cut off events can be done in straightforward way for simulation. As only two pion events are generated for GSIM, then all events forming spike at small CL are *true* two pion events. The left pad of the Fig. 10 shows CL distribution for simulation. Events which passed the cut  $CL < 0.1$  are marked out in red and they amount to 72%.

There is no way to select *true* two pions events from experimental data. Although, we can use additional physics information to isolate such events. Consider  $\rho$  meson production in the intermediate state. It decays with almost 100% probability into  $\pi^+$ ,  $\pi^-$ . So, events corresponding to the sub-channel  $\gamma p \rightarrow p\rho^0 \rightarrow p\pi^+\pi^-$ , assures us they are true two pion events.

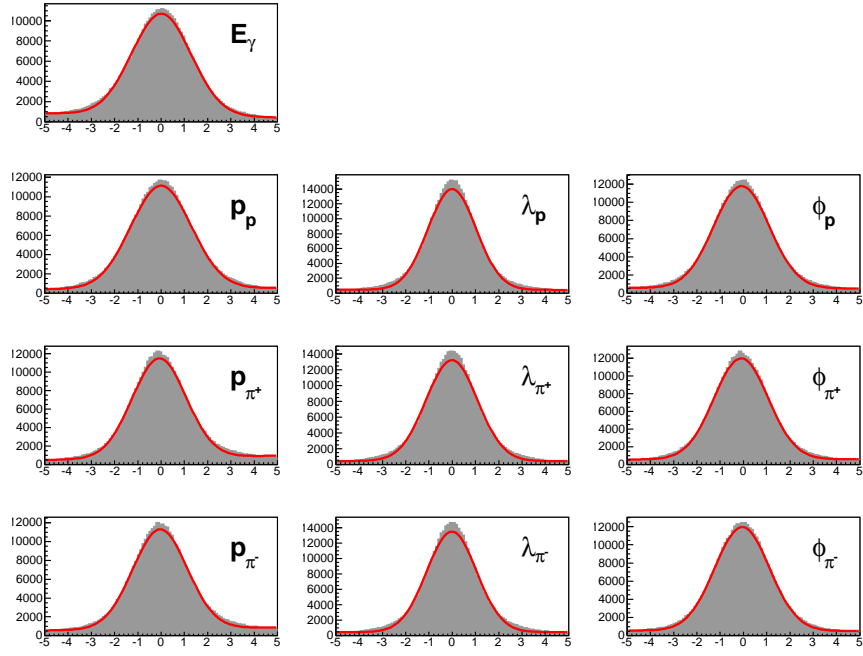


Figure 5: Pull distributions for the topology  $p\pi^+\pi^-(0)$ . See text for designations of measured quantities.

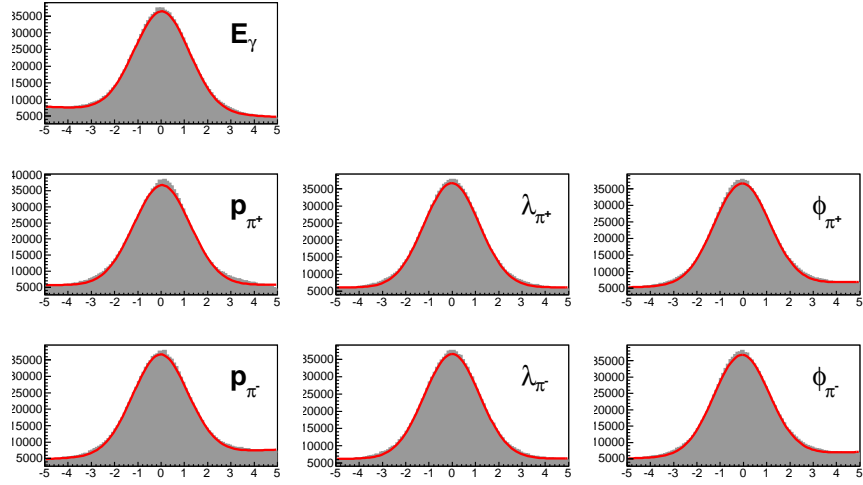


Figure 6: Pull distributions for the topology  $(p)\pi^+\pi^-$ . See text for designations of measured quantities.

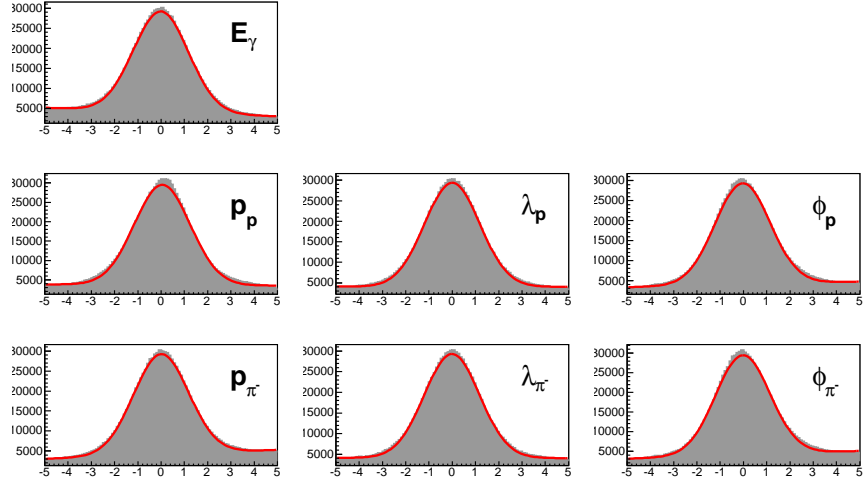


Figure 7: Pull distributions for the topology  $p(\pi^+)\pi^-$ . See text for designations of measured quantities.

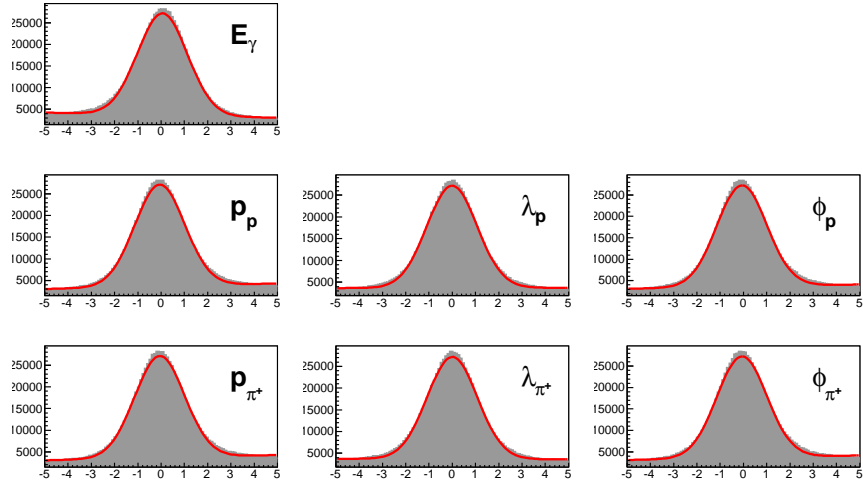


Figure 8: Pull distributions for the topology  $p\pi^+(\pi^-)$ . See text for designations of measured quantities.

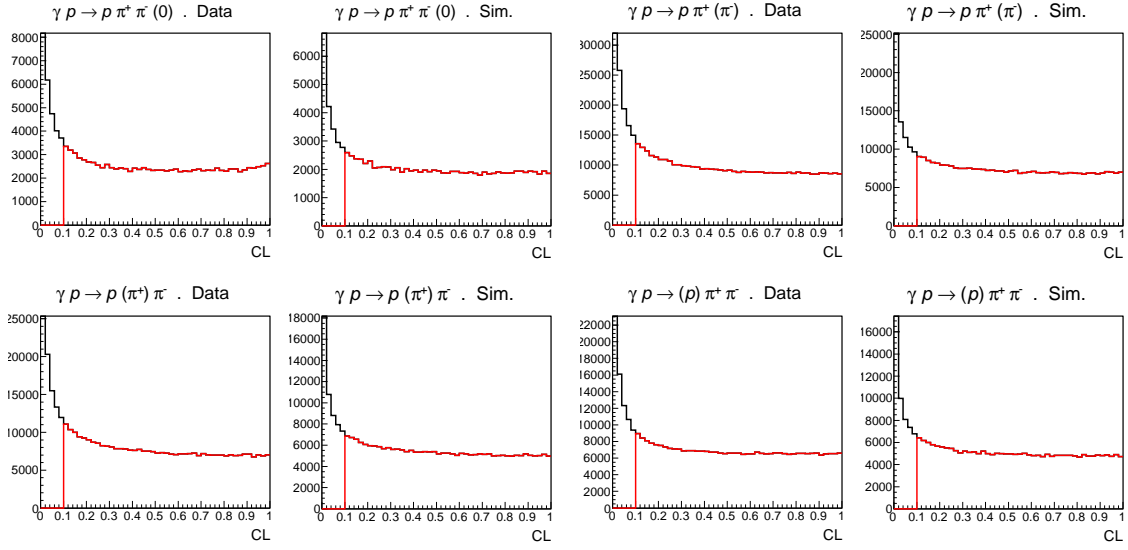


Figure 9: Confidence level (CL) distributions of a sample of events for experimental data (labeled **Data**) and simulation (labeled **Sim.**) Distributions are presented for four topologies.

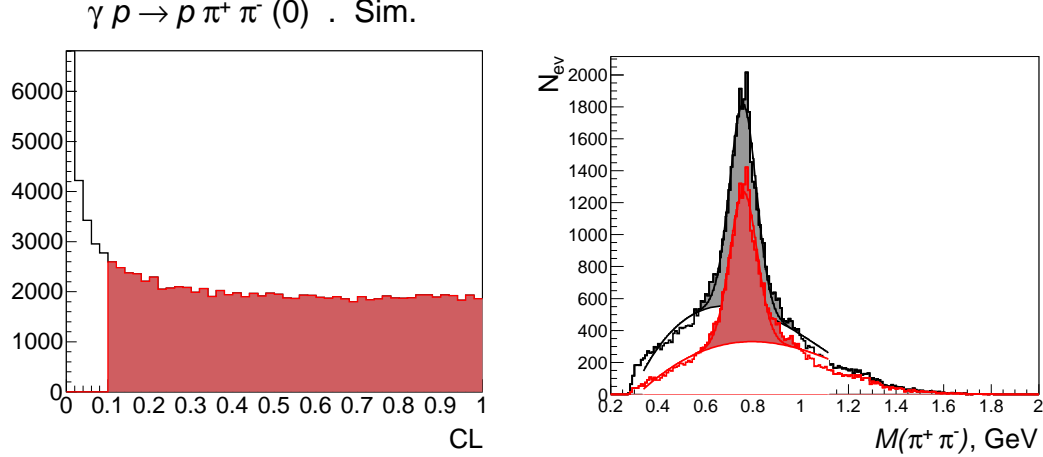


Figure 10: Plot at the left: Confidence level (CL) distributions of a sample of events for simulation. Plot at the right: Invariant mass  $M(\pi^+, \pi^-)$  distribution of experimental data of one run with no CL cut (black) and 10% CL cut (red). Both plots were obtained after loose cuts on missing mass had been applied (see text for details).

If we plot the histogram of  $M(\pi^+, \pi^-)$  distribution, where  $M(\pi^+, \pi^-)$  is the invariant mass of  $\pi^+$  and  $\pi^-$ , then events generating the peak at the mass of rho ( $\approx 0.77$  GeV) are *true* two pion events.

The right pad in Fig. 10 presents two  $M(\pi^+, \pi^-)$  distributions for the topology  $p\pi^+\pi^-$ . Loose cut on missing mass has been applied before CL cut for both distributions. Distribution

with no CL cut and with the cut  $CL < 0.1$  are shown in black and red respectively. Distributions are fit with Gaussian ( $\rho$  peak) plus polynomial (background) functions. In this manner the square of the area under the peaks gives the number of events with production of  $\rho$  in intermediate state, and consequently they are true two pion events. It should be noted that we can not separate events with and without  $\rho$  production, but we do can determine the quantity of such events.

Comparing the squares under the peaks we found that  $\approx 75\%$  of true two pion events pass the CL cut at 0.1. So, simulated and experimental data has given close results: 72% and 75% events pass the CL cut at 0.1. It is consistent with the studies in [8], where 3% systematic error is used to account for the mismatch in the kinematic fit behavior between data and Monte Carlo. Thus, kinematic fit can be reliably used with 3% systematic error.

Probably the the reason for the fact that *true* two pion events form a tail at small CL is that reliable covariance matrix can hardly be obtained for all possible kinematics of particles in CLAS.

### 3.4 Photon flux

Photon flux from the tagger was obtained with standard *gflux* [17] method during cooking of g11a data.

Data analysis of the reactions  $\gamma p \rightarrow p\omega \rightarrow p\pi^+\pi^-\pi^0$  [16] and  $\gamma p \rightarrow p\rho^0 \rightarrow p\pi^+\pi^-$  [9] from g11a data with different beam current revealed dependence of  $\omega$  and  $\rho$  yields on electron beam current. Observed dependence can be fit with linear function: the *lost yields*  $= 1 - 0.0026 \times \text{current}(\text{ns})$  with uncertainty of slope coefficient about 6%. Thus the correction for a typical run with 60 na beam current is about 15% and the systematic uncertainty is about 1%.

As mentioned above, only first 40 T-counters of the tagger were included in the g11a trigger, although the data acquisition collected information from the whole set of T- and E-counters. Events caused by electrons hitting counters 41–60 could be written into the data stream if there was another hit of any of the first 40 counters during the trigger time window. Thus, events of the whole set of T-counters may be used in an analysis. The flux rate corresponding to the T-counters 41–60 is obviously expected to be lower than to the first 40 counters. In [11] the probability that at least one electron hit any of the first 40 T-counters during the trigger time window was evaluated, based on the T-counter rates. This probability is 0.46669. Therefore we must scale the yield by  $1/0.46669 = 2.143$  for events caused by the hits in counters 41–60, i.e. for  $W > 1.956$ . Fig. 11 demonstrates normalized yield of two pion events per E-counter, i.e. the number of events divided by the flux, after the mentioned above correction factor has been applied.

A number of hot or dead E-counter are excluded from the analysis. Apart for that malfunctioning E-counters we can clearly see in Fig. 11 see two dips located at counter numbers  $\approx 80$ –90 and 185–195. The widths of the dips suggests that they are related to low efficient T-counters. Moreover their behavior was unstable from run to run.

In the following analysis the final cross section in the areas corresponding to the problematic E- or T-counters (or ranges of counters) was calculated by scaling the cross



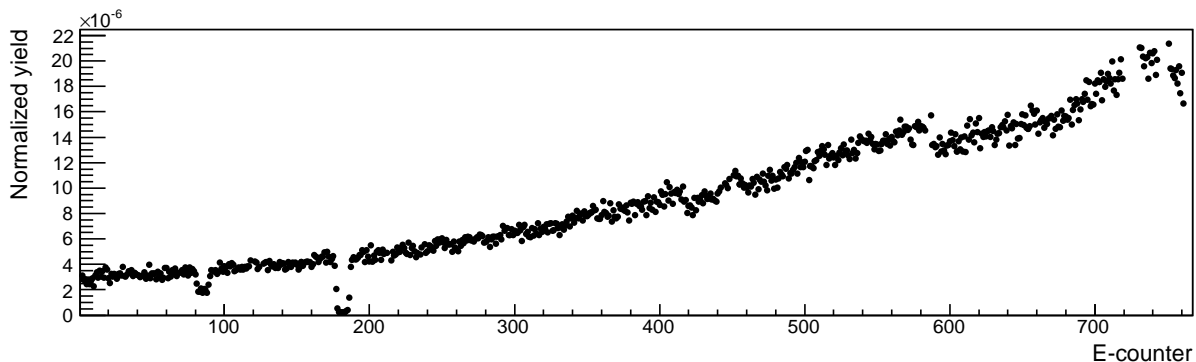


Figure 11: Normalized yield of a sample of two pion events per E-counter. Malfunctioning E-counters has been cut out. Factor 2.143 is applied for counters  $> 586$ .

section in that area. The scaling factor was obtained in such a way that the resulting cross section has to be equal to the averaged value of the cross sections in the left and right side adjacent bins.

## 4 Monte Carlo simulation

CLAS efficiency is obtained with the help of simulation with standard CLAS GSIM package. The output of GSIM was processed by CLAS GPP. Smearing parameter for scintillators was 0.5 and for all regions of drift chambers that parameters were 1.0. Additional empirical smearing algorithm was applied to match the resolution in CLAS and GSIM. See [11] for details.

### 4.1 Event generator

Event generator for GSIM is based on the JM model [3, 4]. At the first step preliminary cross section was obtained using the model distributions in event generator. Then, distributions provided by the model were adjusted to the preliminary calculated single differential cross sections. This adjusted model cross section was used in the simulation.

Fig. 12, 13, demonstrates examples of comparisons of the final experimental cross sections with the distributions of event generator. (See section 5.1 for kinematics variable definitions.) Event generator reproduces well single differential distribution for  $W < 2.0$  GeV, as the model was adjusted at small  $W$ , and probably it reproduces basic features of the 4-fold differential cross section for  $W < 2.0$  GeV. For  $W < 2.0$  GeV the model prediction was used and single differential cross sections were manually adjusted.

It was not possible to adjust manually all nine single differential cross section together corresponding to large  $W$ , since they are strongly correlated. Kinematics of the two pion photoproduction with unpolarized particles is described with four variables. Consequently,

four single differential distributions can be fit to any four given functions. Adjustments of nine single differential distributions together requires knowledge of the 4-fold differential cross section which is unknown and can not be measured at present.

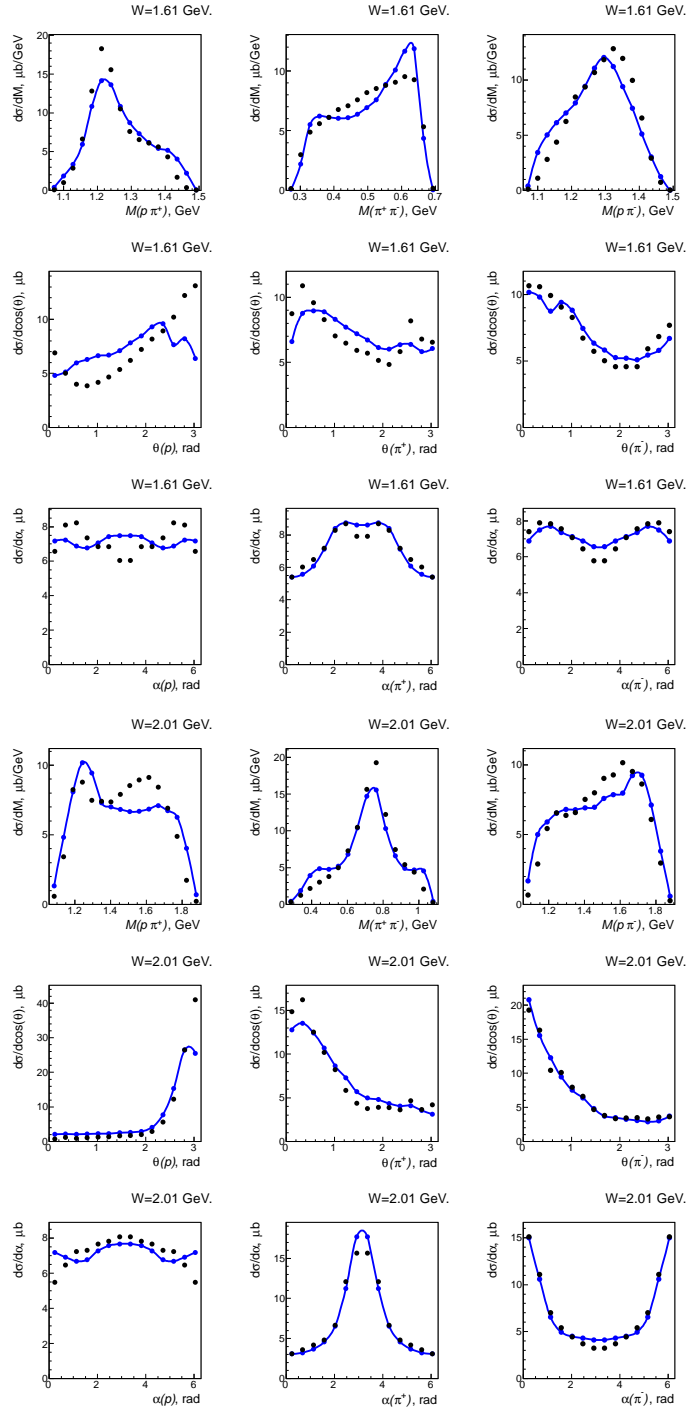


Figure 12: Comparison of experimental differential cross sections (black points) with distributions from the event generator (blue lines) for  $W$  intervals 1.6–1.625 GeV and 2.0–2.025 GeV. Distributions are scaled to have the same integrated value. Kinematics variables are defined in section 5.1.

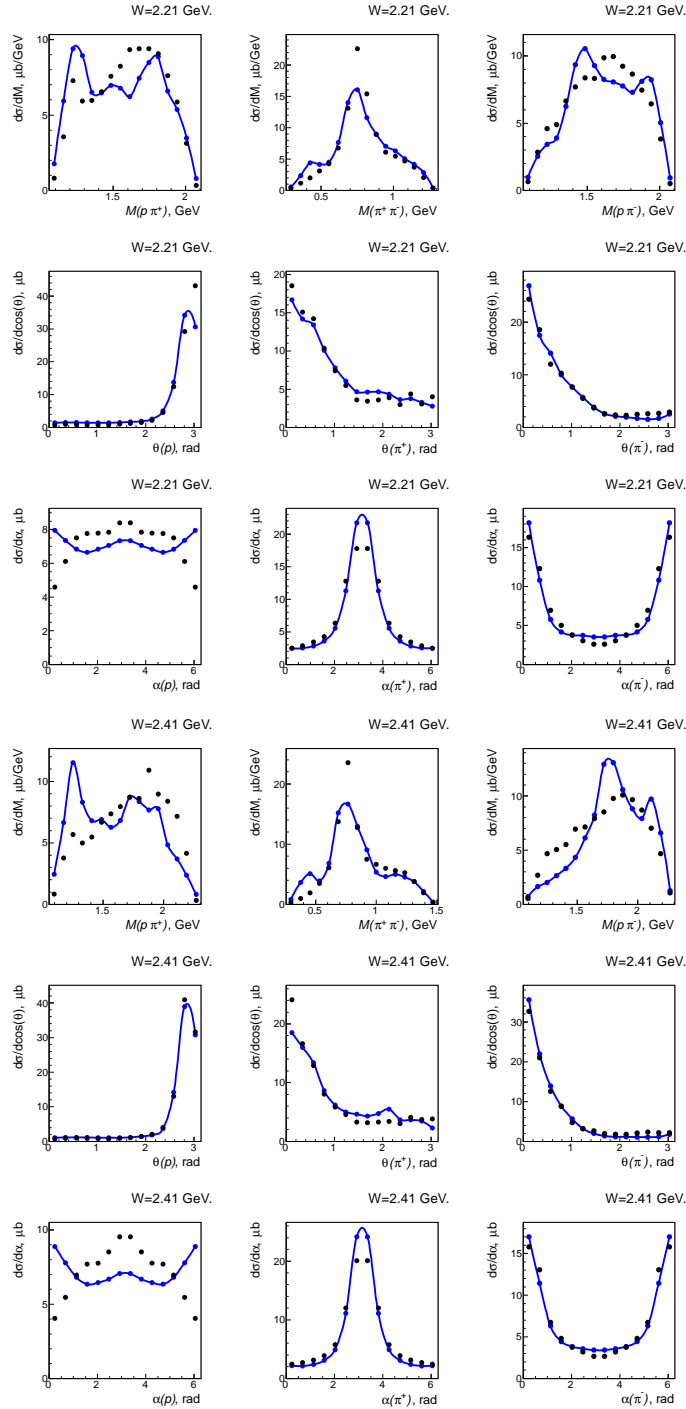


Figure 13: Comparison of experimental differential cross sections (black points) with distributions from the event generator (blue lines) for  $W$  intervals 2.2–2.225 GeV and 2.4–2.425 GeV. Distributions are scaled to have the same integrated value. Kinematics variables are defined in section 5.1.

## 4.2 Efficiency correction and fiducial cuts

Detector efficiency may not be reproduced exactly with GSIM, as there can exist a number of detector components which did not operated properly during runs. It is also possible that certain components had unstable behavior from run to run. In addition efficiency may not be calculated correctly from simulation if the event generator does not reproduce well multidifferential cross section, as distributions from event generator were fit to the only single differential cross section.

Employing the cross section obtained from different topologies we can try to improve efficiency evaluation. Let us denote true detection efficiency as  $\varepsilon_{true}$  and efficiency obtained from simulation as  $\varepsilon_{sim}$ . Normally  $\varepsilon_{sim}$  is calculated in simulation as a ratio of reconstructed over generated events. Efficiencies are assumed to be dependent on the particle momenta in laboratory frame.

The cross section of a reaction with tree particles in the final state depends on five kinematics variables. Consider three independent variables to be particle momentum modulus  $|p|$  and spherical angles  $\theta, \phi$  in in laboratory frame. Any particle may be chosen. Denote other two variables by  $x$ .

The cross section in a certain bin in  $|p|, \theta, \phi$  and  $x$  is calculated as:

$$\frac{d\sigma}{d|p|d\theta d\phi dx} = C \frac{N_{det}}{\varepsilon_{sim}}, \quad (4)$$

where  $C$  is a production of all factors which do not depend on efficiency or number of events,  $N_{det}$  is a number of detected events.  $N_{det}$  can be transcribed as  $N_{det} = N_{true}\varepsilon_{true}$ , where  $N_{true}$  is a true number of reaction events.

The cross section for unpolarized photons is  $\phi$  independent ( $N_{true}$  does not depend on  $\phi$ ), we assume all cross sections are integrated over  $\phi$ :

$$\frac{d\sigma}{d|p|d\theta dx} = C N_{true} \int \frac{\varepsilon_{true}}{\varepsilon_{sim}} d\phi, \quad (5)$$

Select a set of events, when all particles are detected. Consider the cross section for the topology, when all particles are detected ( $p\pi^+\pi^-(0)$ ). With a reasonable accuracy we can suppose that detection efficiency of a many particle event is a product of single particle efficiencies. So, for the topology  $p\pi^+\pi^-(0)$  the efficiency of the detection of three particles is  $\varepsilon(p\pi^+\pi^-) = \varepsilon(p)\varepsilon(\pi^+)\varepsilon(\pi^-)$ , where  $\varepsilon(p) \equiv \varepsilon(|p|_p, \theta_p, \phi_p)$  is a proton detection efficiency and so on. Then (5) can be rewritten as:

$$\left. \frac{d\sigma}{d|p|_p d\theta_p dx_p} \right|_{p\pi^+\pi^-(0)} = C \cdot N_{true} \int \frac{\varepsilon_{true}(\pi^+)\varepsilon_{true}(\pi^-)\varepsilon_{true}(p)}{\varepsilon_{sim}(\pi^+)\varepsilon_{sim}(\pi^-)\varepsilon_{sim}(p)} d\phi_p. \quad (6)$$

On the other hand we can calculate this cross section for the topology, when one particle is missing, exploiting the same set of events. In this case we assume one of the particle is missing, although it is detected. In this way we need efficiencies for two particles out of tree.

Say proton is missing ( $(p)\pi^+\pi^-$ ), then

$$\left. \frac{d\sigma}{d|p|d\theta dx_p} \right|_{(p)\pi^+\pi^-} = C \cdot N_{true} \int \frac{\varepsilon_{true}(\pi^+)\varepsilon_{true}(\pi^-)}{\varepsilon_{sim}(\pi^+)\varepsilon_{sim}(\pi^-)} d\phi_p. \quad (7)$$

The integrated over  $x$  ratio of (6) over (7) is

$$r_p(|p|_p, \theta_p) = \int \left( \int \frac{\varepsilon_{true}(\pi^+)\varepsilon_{true}(\pi^-)\varepsilon_{true}(p)}{\varepsilon_{sim}(\pi^+)\varepsilon_{sim}(\pi^-)\varepsilon_{sim}(p)} d\phi_p \right) / \left( \int \frac{\varepsilon_{true}(\pi^+)\varepsilon_{true}(\pi^-)}{\varepsilon_{sim}(\pi^+)\varepsilon_{sim}(\pi^-)} d\phi_p \right) dx. \quad (8)$$

In (8)  $\varepsilon(\pi^+)$  and  $\varepsilon(\pi^-)$  depend on  $\phi_p$  implicitly. We can make an approximation that

$$r_p(|p|_p, \theta_p) \approx \frac{1}{2\pi} \int \frac{\varepsilon_{true}(p)}{\varepsilon_{sim}(p)} d\phi_p \quad (9)$$

is the averaged ratio of *true* over *simulation* efficiencies. In the same way the ratios  $r_{\pi^+}$  over  $r_{\pi^-}$  can be obtained as functions of  $|p|$  and  $\theta$  of corresponding particle. Then efficiencies obtained from simulation can be corrected for each particle:

$$\varepsilon_{sim} \rightarrow r \times \varepsilon_{sim} = \varepsilon_{true}. \quad (10)$$

The validity of the made above approximation can be verified if we compare the cross sections from different topologies after the correction has been applied. If the approximation is valid then corrected cross sections should coincide.

Plots with values of  $r$  are demonstrated in the left column in Fig. 14 for  $p$ ,  $\pi^+$  and  $\pi^-$ . Right column shows recalculated values of  $r$  that were obtained using corrected (10) simulation efficiencies. Corrections are applied for all three particles. One can see on the plots in the right column that efficiency ratios are not equal to exact unity. Single particle efficiencies can not be ideally corrected. On the average, the deviation from unity is about 1.5%. Thus, the systematic uncertainty related to the efficiency correction is  $\approx 1.5\%$ .

Efficiency ratios  $r$ -s was used to define fiducial volume of CLAS for this given reaction. Fiducial volume isolation is based on the assumption that if  $r = \varepsilon_{true}/\varepsilon_{sim}$  is close enough to unity for all detected particles of an event in a certain kinematics region, then this region should be included into fiducial volume.

Fiducial volume was selected with the following criteria:  $|r(|p|, \theta) - 1| \leq 30\%$  before correction and  $|r(|p|, \theta) - 1| \leq 5\%$  after correction. We found out that regions with very low efficiencies should not be taken into account. So, additionally regions, where  $\varepsilon_{sim} \leq 0.02$  were cut off.

It should be noted that the described procedure is limited to the acceptance area, where all three particles are detected. Efficiency in the kinematics space, when one of the particle goes at small or large  $\theta$  angles can not be verified and corrected. However, the cross section at small or large angles has considerable contribution of dead zones of CLAS detector (see section 5.5). Therefore, the uncertainties in the cross sections corresponding that area are large (see section 5.5) and we can assume they account, at least partly, for the uncertainties associated with efficiency mismatch in experimental data and Monte Carlo.

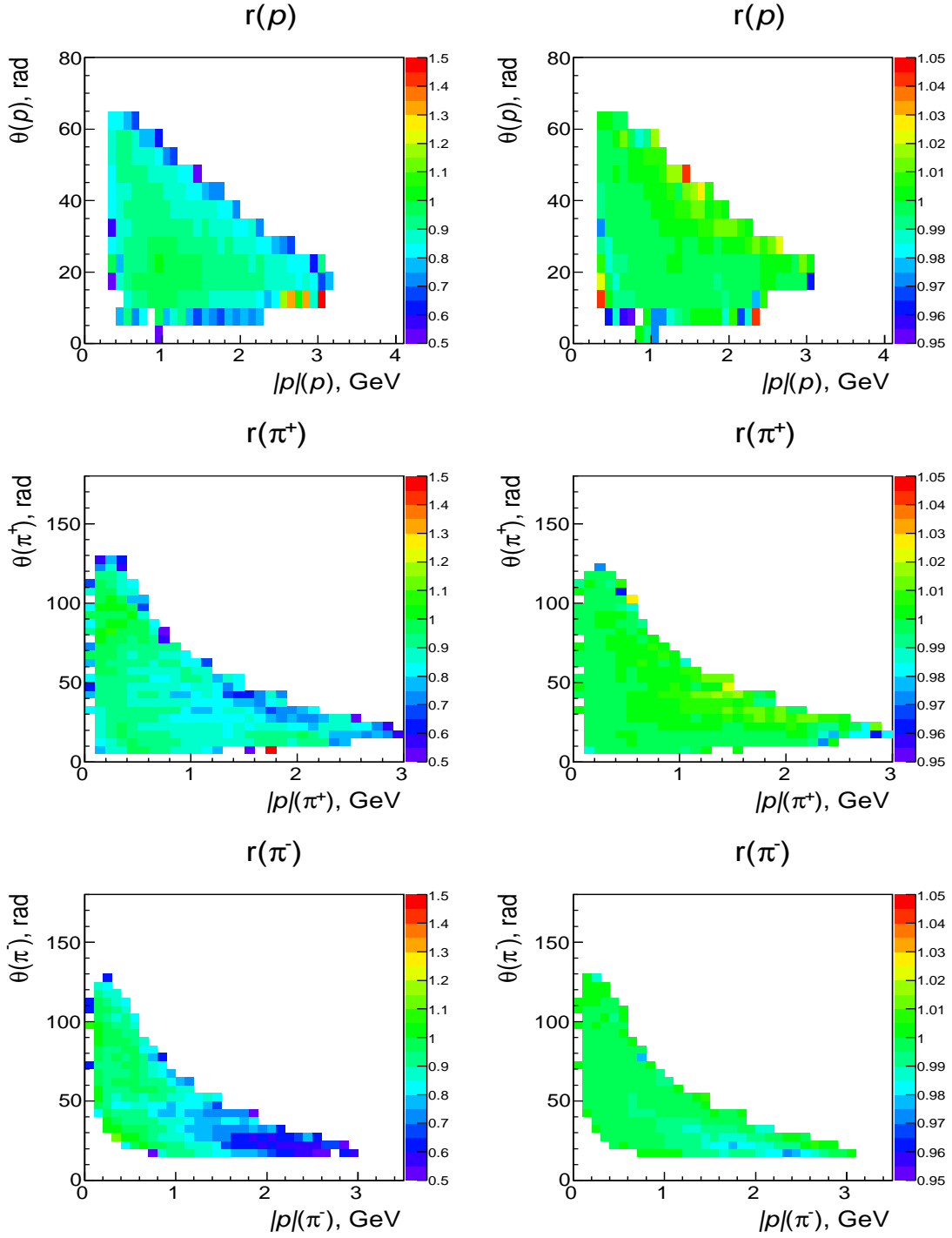


Figure 14: The ratio of cross sections  $r$  calculated for two topologies (see text). Initial values of  $r$  are presented in the left column. Recalculated values of  $r$ , when using using corrected (10) simulation efficiencies are presented in the right column.

## 5 Cross section

### 5.1 Cross section calculation

Final state kinematics of the reaction  $\gamma p \rightarrow p\pi^+\pi^-$  is described by 5 independent variables. Our choice is three sets of variables:

- $M(p, \pi^+), M(\pi^+, \pi^-), \theta_p, \phi_p, \alpha_p$
- $M(\pi^+, \pi^-), M(\pi^-, p), \theta_{\pi^+}, \phi_{\pi^+}, \alpha_{\pi^+}$
- $M(\pi^-, p), M(p, \pi^+), \theta_{\pi^-}, \phi_{\pi^-}, \alpha_{\pi^-}$

$M(x, y)$  is invariant mass of two particles  $x$  and  $y$ .  $\theta_x$  and  $\phi_x$  are spherical angles of momentum direction of particle  $x$  in CMS.  $\alpha_x$  is rotation angle of the plane formed by momenta vectors of particles  $y$  and  $z$  around the momentum vector of the particle  $x$  in CMS. The cross section for unpolarized  $\gamma$  and initial proton is  $\phi$ -independent. Thus, from here on, all distributions are assumed to be integrated over  $\phi$ .

The 4-fold differential cross section is calculated in usual way. In terms of the first set of kinematics variables it is:

$$\frac{d^4\sigma}{dM(p, \pi^+) \cdot dM(\pi^+, \pi^-) \cdot d\cos(\theta_p) \cdot d\alpha_p} = \frac{A}{N_a \rho l} \cdot \frac{1}{F} \cdot \frac{N_{det}}{\varepsilon}, \quad (11)$$

where  $A \equiv$  atomic weight,  $N_a \equiv$  Avogadro's number,  $\rho \equiv$  target density,  $l \equiv$  target length and  $F \equiv$  photon flux. G11A runs used target of a liquid hydrogen of 40 cm length.  $\varepsilon \equiv$  is efficiency determined from simulation and corrected as described in section 4.2. The photon flux was calculated during cooking by gflux package [17].

### 5.2 Cross section $\alpha$ symmetry

Integrated over  $\phi$  cross section is symmetrical with respect to  $\alpha$  angle. This fact can be used to test the accuracy of the calculations. In Fig. 15 one can see  $\alpha$  distributions. Asymmetry is negligible. We can use this to increase statistics. From here on, when calculating the cross section the numbers of detected events in each symmetric with respect to  $\alpha$  bins are put to be as the sum of events in that bins divided by two. The same is applied to the numbers of generated in simulation and reconstructed events. This procedure duplicates statistics and forces the the cross section to be ideally symmetrical.

### 5.3 Cross section from different topologies

Comparison of the cross section calculations obtained when using different topologies can be used as a good test of reliability of the results and a check of the systematic error estimation.

There are four topologies for two pion production: all particles are detected, proton is missing, positive or negative pion is missing. Denote them by: (0), ( $p$ ), ( $\pi^+$ ) and ( $\pi^-$ ) respectively.



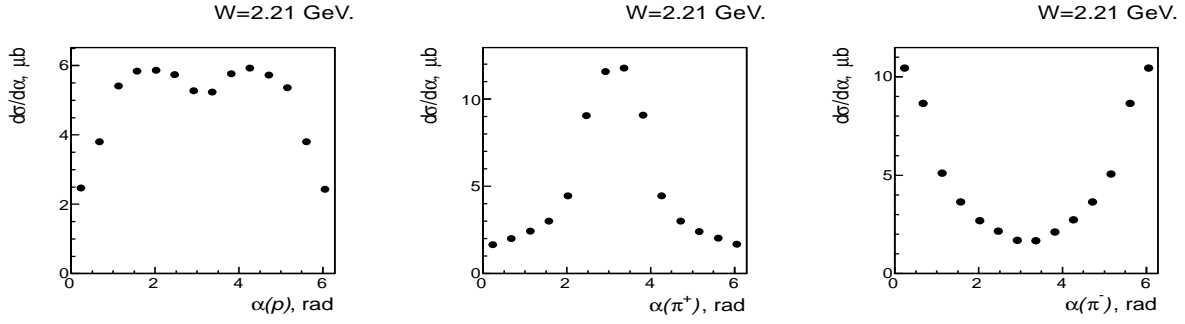


Figure 15:  $\alpha$  distributions with CLAS acceptance.

Each topology has its own acceptance. To be consistent, when comparing cross sections for two or more topologies, the cross section evaluation must be done in the same kinematics region of acceptance for all that topologies. Therefore, acceptance region must be isolated so, that none of the compared topologies has inefficient areas within that region. Inefficient area means area that is out of the detector acceptance and a cross section can not be measured in it.

Comparison of the cross sections has been made for topologies (0), ( $p$ ), ( $\pi^+$ ) and ( $\pi^-$ ), as well as for pairs: ( $p$ )-( $\pi^+$ ), ( $p$ )-( $\pi^-$ ) and ( $\pi^+$ )-( $\pi^-$ ). Typical results of such comparison for  $W$  bin [2.0; 2.025] GeV are shown in Fig.16.

Fig. 16 demonstrates reasonable agreement between cross sections for different topologies. This comparison can also be used as an independent check for the estimation of systematic errors. On the average the difference between cross sections is  $\approx 4\%$ . Though, in few points which are mostly located at small  $\theta(\pi^+)$  the difference between cross sections is as large as  $\approx 20\%$ . It will be shown later that in these points the contribution of inefficient multidimensional bins into a bin of a single differential cross section is large and the cross section can not be measured with high precision in that bins, see section 5.5.

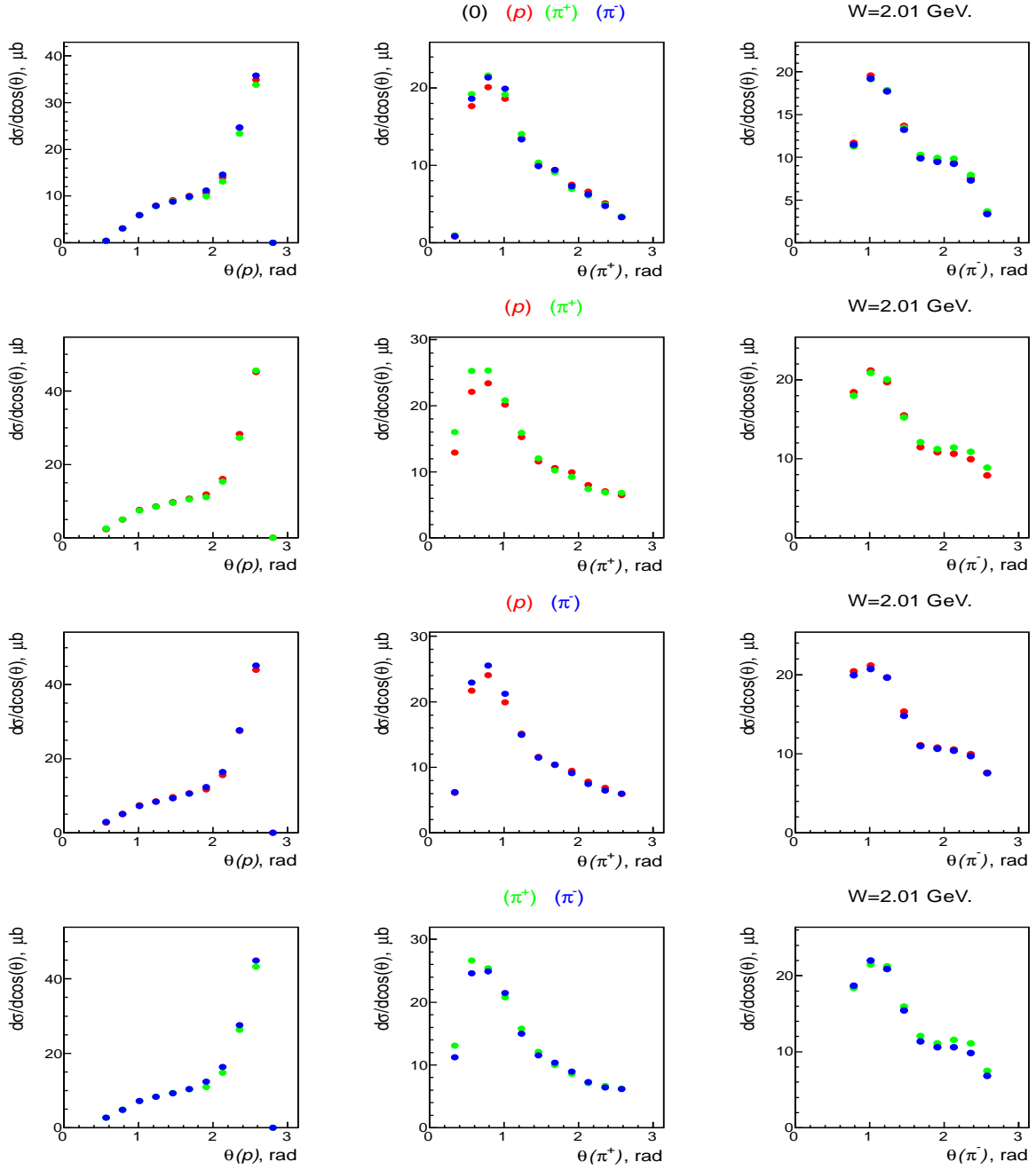


Figure 16: Comparison of differential cross section  $d\sigma/d\cos(\theta)$  for different topologies, where  $\theta$  is polar angles of proton or pion. The color of a point indicate topology. Topology types are shown on tops of the center plots in corresponding colors. (See text for designations.) Top row of plots shows the comparison of the cross section for four topologies (0), ( $p$ ), ( $\pi^+$ ) and ( $\pi^-$ ). Other plots show comparisons between cross sections for pairs of topologies. Note the black points are not seen on the top plots, as they are covered by the other points.

## 5.4 Three pion admixture

Selection of two pion events  $\gamma p \rightarrow p\pi^+\pi^-$  relies upon kinematic fit. However, there is still possibility of wrong event identification. The most probable contamination comes from three pion events  $\gamma p \rightarrow p\pi^+\pi^-\pi^0$ .

Three pion event may be reconstructed as two pions event. This effect can be seen from simulation. Both two and three pion events were included into simulation. Realistic event generator was used for two pion events, see section 4.1. Three pion events were generated in phase space approximation. In the event generator the ratio of fully integrated cross sections of both reactions was fit to the experimental data, see Fig. 17.

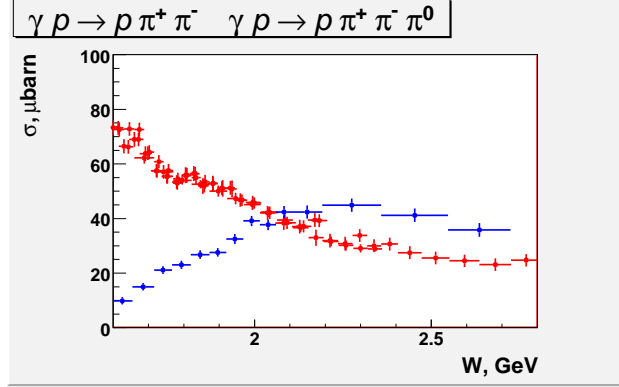


Figure 17: Experimental fully integrated cross sections for two (red) [18] and three pion (blue) [19] photoproduction.

In Fig. 18. you can see missing mass distributions for three topologies. Kinematic fit modifies momenta of detected particles to fit the missing mass to its true value, so kinematic fit was used to select events, but the missing mass distributions were obtained from unmodified momenta. Falsely reconstructed three pion events do not produce extra bumps or any background in that distributions. Thus, they are indistinguishable from true events. Missing mass distribution is not shown for the topology, when all particles are detected. In this topology three pion events do not pass kinematic fit. It is expectable, since kinematic fit is more restrictive in this case, as it is a 4-constrain fit.

The final cross section should be corrected due to the tree pion contamination. Correction factor can be obtained from simulation, where event generator includes both two and three pion channels with realistic relative fractions of them.

Denote  $N(p\pi^+\pi^-)$  as the number of reconstructed 2 pion events and  $N(p\pi^+\pi^-\pi^0)$  as the number of 3 pions events reconstructed as 2 pion events, then correction factor is

$$R_{3\pi} = \frac{N(p\pi^+\pi^-)}{N(p\pi^+\pi^-) + N(p\pi^+\pi^-\pi^0)} . \quad (12)$$

Then obtained experimental cross section should be multiplied by this factor. Fig. 19 presents calculated  $W$  dependence of  $R_{3\pi}$ . We limited ourselves to the only  $W$  dependence of the

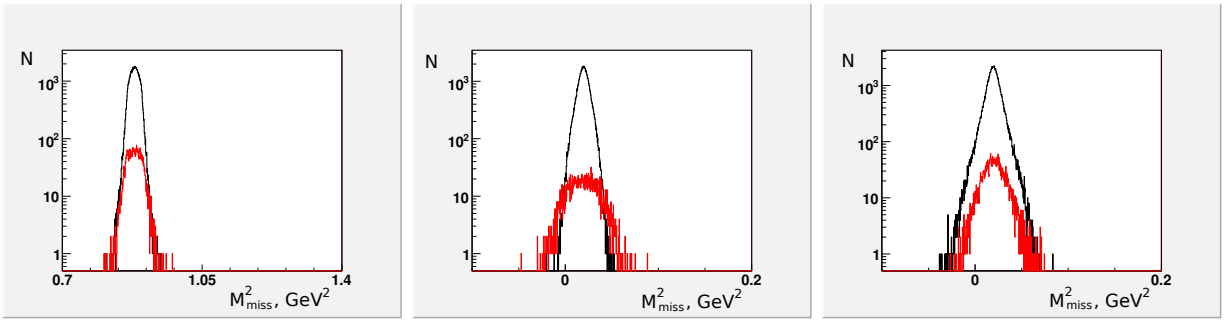


Figure 18: Missing mass squared distribution (all  $W$ ) from simulation for three topologies:  $(p)\pi^+\pi^-$  (left plot),  $p(\pi^+)\pi^-$  (center plot) and  $p\pi^+(\pi^-)$  (right plot). Black line corresponds to the true 2 pion events and red line to the 3 pion events which were reconstructed as 2 pion events.

correction factor  $R_{3\pi} = R_{3\pi}(W)$ , since in the three pion event generator not realistic phase space approximation was used. Therefore, dependence of the correction factor on other kinematics variables is not reliable.

Correction factor accounting for tree pion admixture is close to unity at  $W = 1.6$  GeV, but it increases to  $\approx 15$  % at  $W = 2.8$  GeV.

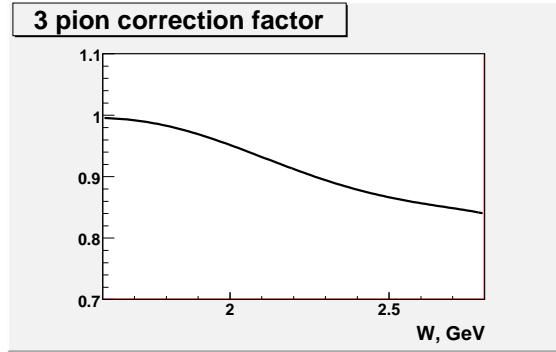


Figure 19:  $W$  dependence of the correction factor accounting for three pion admixture into the two pion photoproduction cross section.

## 5.5 Cross section extrapolation into CLAS dead area

CLAS has *dead* area. *dead* area or *dead* multidimensional bin in kinematics variables is an area or a bin, where two out of three final state particles come into inefficient area of the CLAS detector and the cross section can not be obtained. Dead bins can be determined with the help of simulation. We define multidimensional bin as a dead bin if there are generated but no reconstructed events.

Dead areas are located at forward and backward angles of CLAS. Dead zones between sectors do not create problems, as the cross section does not depend on  $\phi$  and all distributions

are integrated over  $\phi$ . ( $\phi$  in CMS are equal to  $\phi$  in laboratory frame). Simulation accounts for the lost part of the cross section in the area between sectors.

So, the multidifferential cross section corresponding to the kinematics, when at least two final state particles pass the CLAS detector at forward or backward angles remains unknown. As it will be shown later, uncertainties related to the presence of dead areas are the largest for the fully integrated cross section.

Two attempts were made to take into account for the lost part of the cross section, they are based on simple and model approaches.

### 5.5.1 Simple approach

Consider single differential cross sections. Contribution of dead multidimensional bins into every bin of single differential cross sections can be estimated in the following procedure.

The cross section in each bin in single differential distribution is obtained by summation over the multidimensional bins. For example, the value of the cross section in the  $i$ -th bin in distribution over  $\cos(\theta)$  is

$$\frac{d\sigma}{d\cos(\theta_i)} = \int \frac{d^4\sigma \cdot dM^1 dM^2 d\alpha}{dM^1 \cdot dM^2 \cdot d\cos(\theta) \cdot d\alpha} \approx \frac{1}{\Delta(\cos(\theta_i))} \sum_{jkl} \Delta\sigma(M_j^1, M_k^2, \theta_i, \alpha_l), \quad (13)$$

where  $M^1$ ,  $M^2$ ,  $\theta$  and  $\alpha$  are kinematics variables from one of the set listed in section 5.1.

There are certain quantities of dead multidimensional bins ( $N_{dead}^i$ ), where  $\Delta\sigma(M_j^1, M_k^2, \theta_i, \alpha_l)$  can not be measured, and bins with non zero acceptance ( $N_{acc}^i$ ) among bins contributing to  $\frac{d\sigma}{d\cos(\theta_i)}$ . The sum of all kinematically allowed bins ( $N_{tot}^i$ ) is equal to  $N_{acc}^i + N_{dead}^i$ . Exact quantities of  $N_{dead}^i$  and  $N_{acc}^i$  are determined from simulation.

Factor  $R_i$

$$R_i = \frac{N_{dead}^i + N_{acc}^i}{N_{acc}^i} = \frac{N_{tot}^i}{N_{acc}^i} \quad (14)$$

can be used to take into account for contribution of dead bins under simple assumption that the relative contribution of the values of  $\Delta\sigma(M_j^1, M_k^2, \theta_i, \alpha_l)$  in dead multidimensional bins into  $\frac{d\sigma}{d\cos(\theta_i)}$  is proportional to its quantity, i.e. equal to  $N_{dead}^i/N_{tot}^i$ . This assumption is based on the naive approach that dead multidimensional bins are randomly distributed among all bins, and percentage of dead bins with large or small values of  $\Delta\sigma(M_j^1, M_k^2, \theta_i, \alpha_l)$  values are approximately equal to such percentage of all bins.

The cross section obtained within CLAS acceptance can be corrected to take into account dead zone contribution:

$$\frac{d\sigma}{d\cos(\theta_i)} \rightarrow R_i \times \frac{d\sigma}{d\cos(\theta_i)}. \quad (15)$$

Uncertainty related to this procedure is taken to be the half in the increase of the cross section.

In much the same correction procedure is applied to fully integrated and 2-fold differential cross sections. The procedure has certain inconsistency, because integration of 1- or 2-fold

corrected differential cross sections at the same  $W$  may cause the integrals to be different, even though the integrals of the cross sections before correction are equal. Corrected differential cross sections were scaled in such a way as their integrals to be equal to the corrected integrated cross section.

Results of the application of the described simple approach are demonstrated in Figs. 20–22, where corrected differential cross sections are compared to the cross sections obtained within CLAS acceptance. As it was expected, dead multidimensional bins are located mostly at small and large  $\theta$  angles. Contribution from dead bins to the cross sections is more uniform in invariant mass and  $\alpha$  angle distributions.

Described above procedure was tested with the use of artificial dead zones. Suppose, that interval of *theta* angle in CMS from 1.12 rad to 1.80 rad is dead area for protons or positive pions. Experimental event when either a  $\theta_{p^-}$  or  $\theta_{\pi^+}$  are in “dead” interval, then the event is not reconstructed. Then correction procedure is applied to the **only artificial** dead area, ignoring real CLAS dead areas.

Figs. 23–25 demonstrate results of corrections to the artificial dead area. Initial cross section within CLAS acceptance are shown in red. Calculated cross section with added artificial dead area is shown in blue. You can see two dips in  $d\sigma/d\cos(\theta_p)$  and  $d\sigma/d\cos(\theta_{\pi^+})$  distributions (blue dots). This situation is close to the experimental one. Contribution of the the cross section from dead bins is  $\approx 30\text{--}50\%$  in the regions of dips. Corrected cross section is shown in black. It demonstrates reasonable agreement with the initial cross section (red dots) within uncertainties. The agreement is worse in the regions, where the contribution of of dead bins is large. If this contribution is more than 50 % then the describe above approach, probably, becomes not reliable.

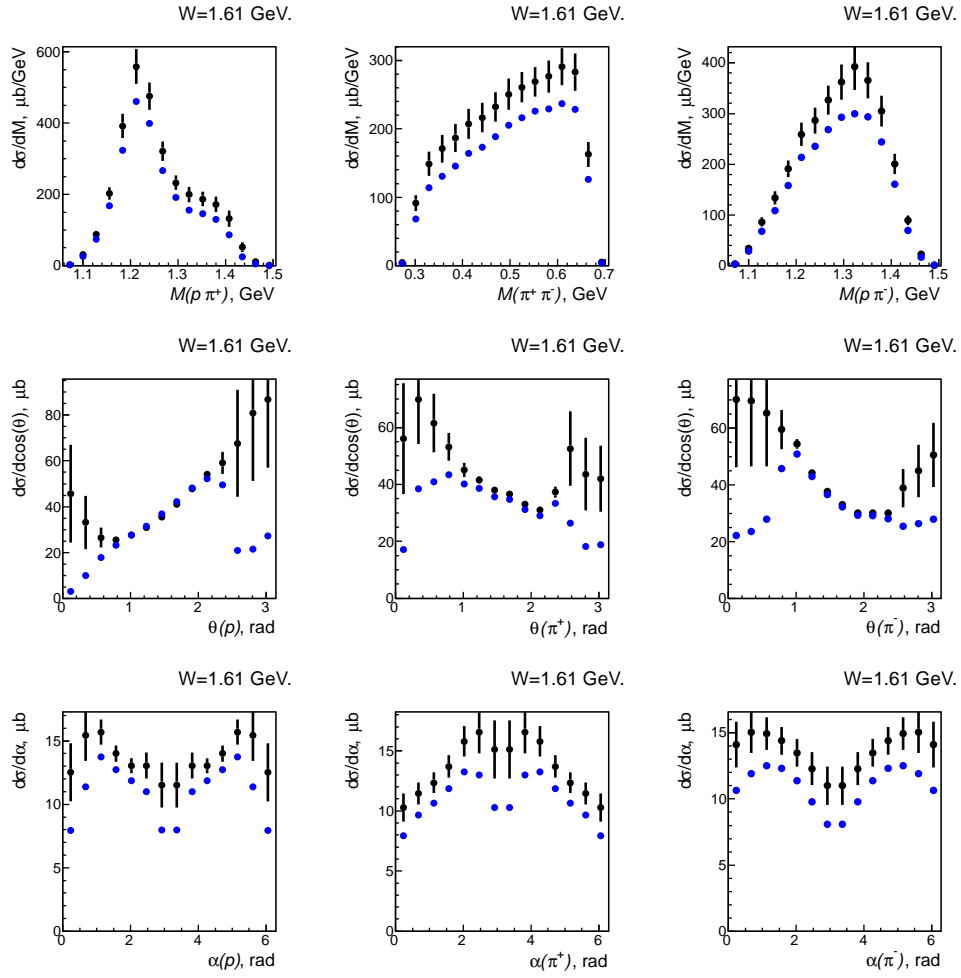


Figure 20: Single differential cross sections for  $1.6 \text{ GeV} < W < 1.625 \text{ GeV}$ . Cross section within CLAS acceptance is in blue. Cross section accounted for dead area in simple approach is in black. Statistical errors are negligible. See text for estimation of uncertainties for black dots.

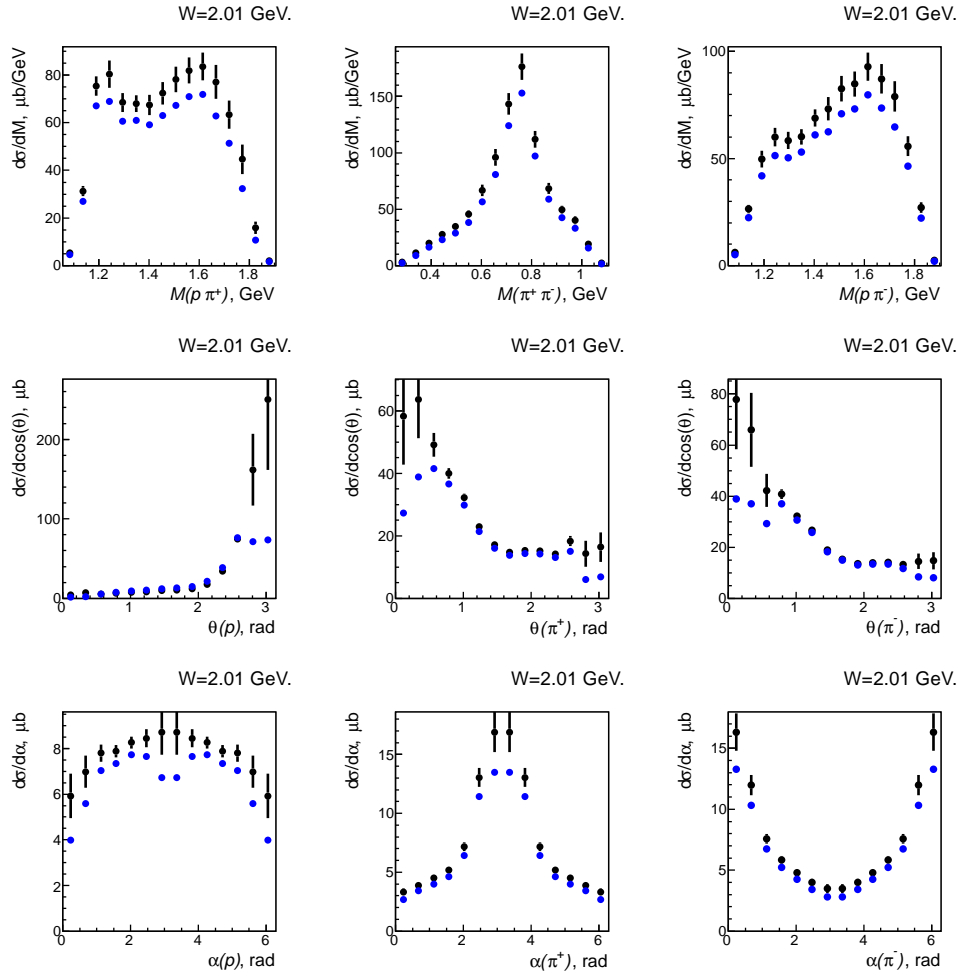


Figure 21: Single differential cross sections for  $2.0 \text{ GeV} < W < 2.025 \text{ GeV}$ . Cross section within CLAS acceptance is in blue. Cross section accounted for dead area in simple approach is in black. Statistical errors are negligible. See text for estimation of uncertainties for black dots.



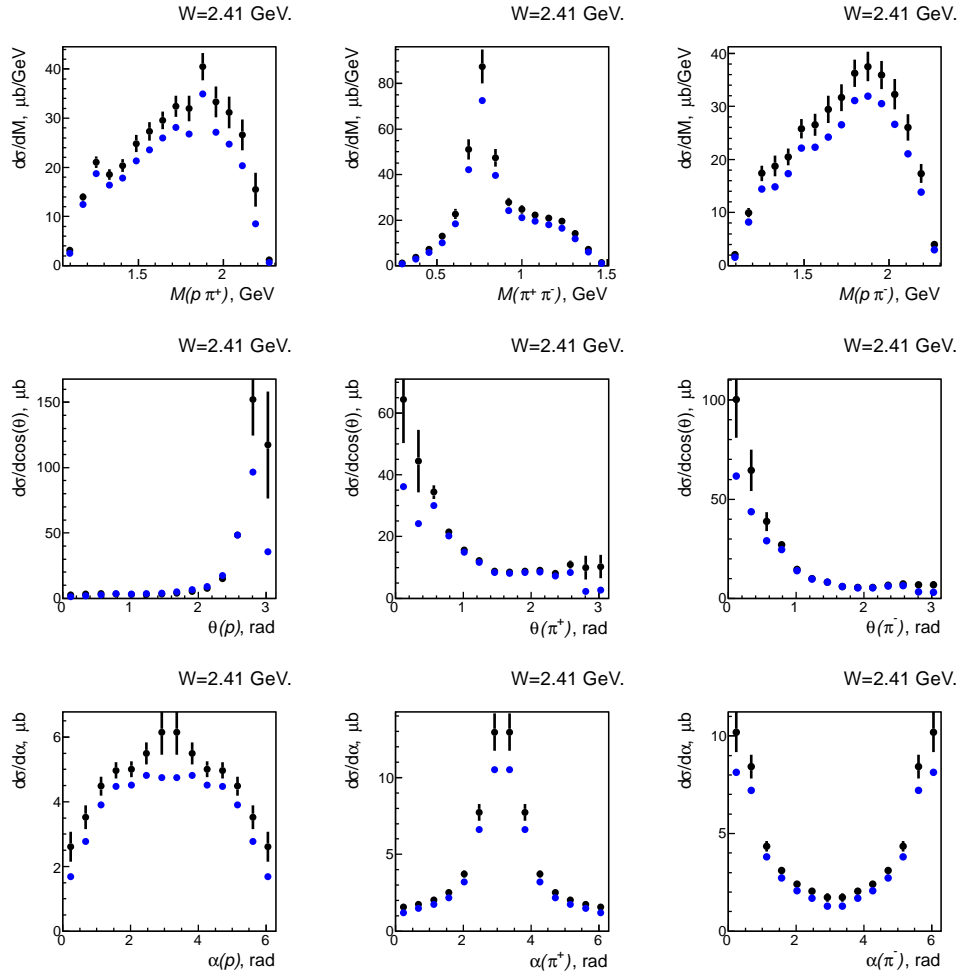


Figure 22: Single differential cross sections for  $2.4 \text{ GeV} < W < 2.425 \text{ GeV}$ . Cross section within CLAS acceptance is in blue. Cross section accounted for dead area in simple approach is in black. Statistical errors are negligible. See text for estimation of uncertainties for black dots.

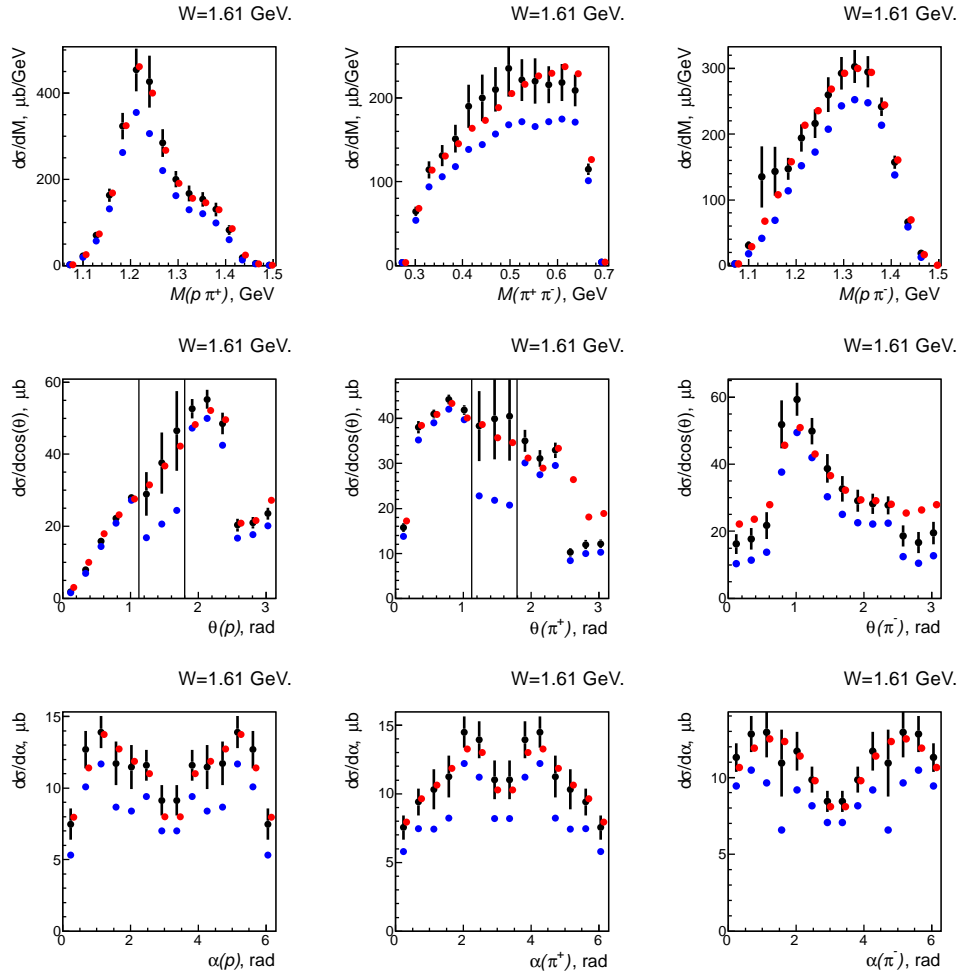


Figure 23: Single differential cross sections for  $1.6 \text{ GeV} < W < 1.625 \text{ GeV}$ . Cross section within CLAS acceptance is in red. Cross section with an artificial dead area is in blue. Artificial dead regions are marked with vertical lines, see text. Cross section accounted for **only artificial** dead area in simple approach is in black. See text for estimation of uncertainties for black dots.

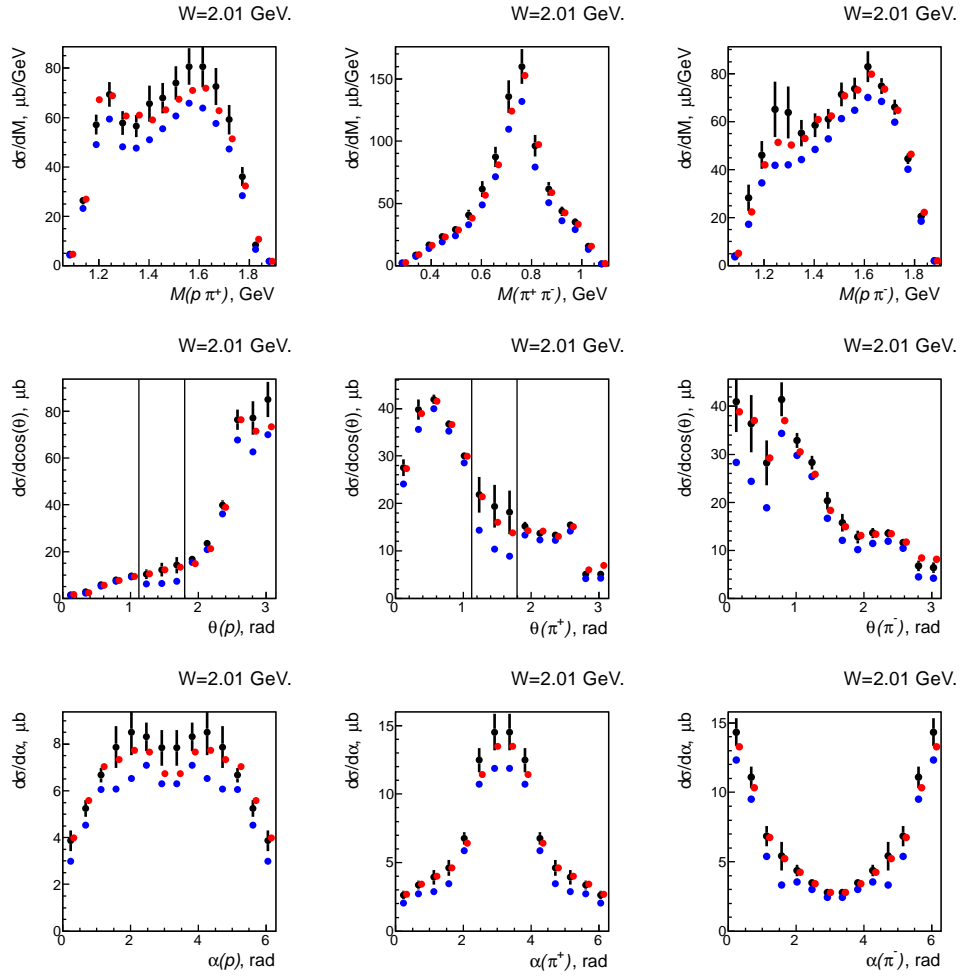


Figure 24: Single differential cross sections for  $2.0 \text{ GeV} < W < 2.025 \text{ GeV}$ . Cross section within CLAS acceptance is in red. Cross section with an artificial dead area is in blue. Artificial dead regions are marked with vertical lines, see text. Cross section accounted for **only artificial** dead area in simple approach is in black. See text for estimation of uncertainties for black dots.

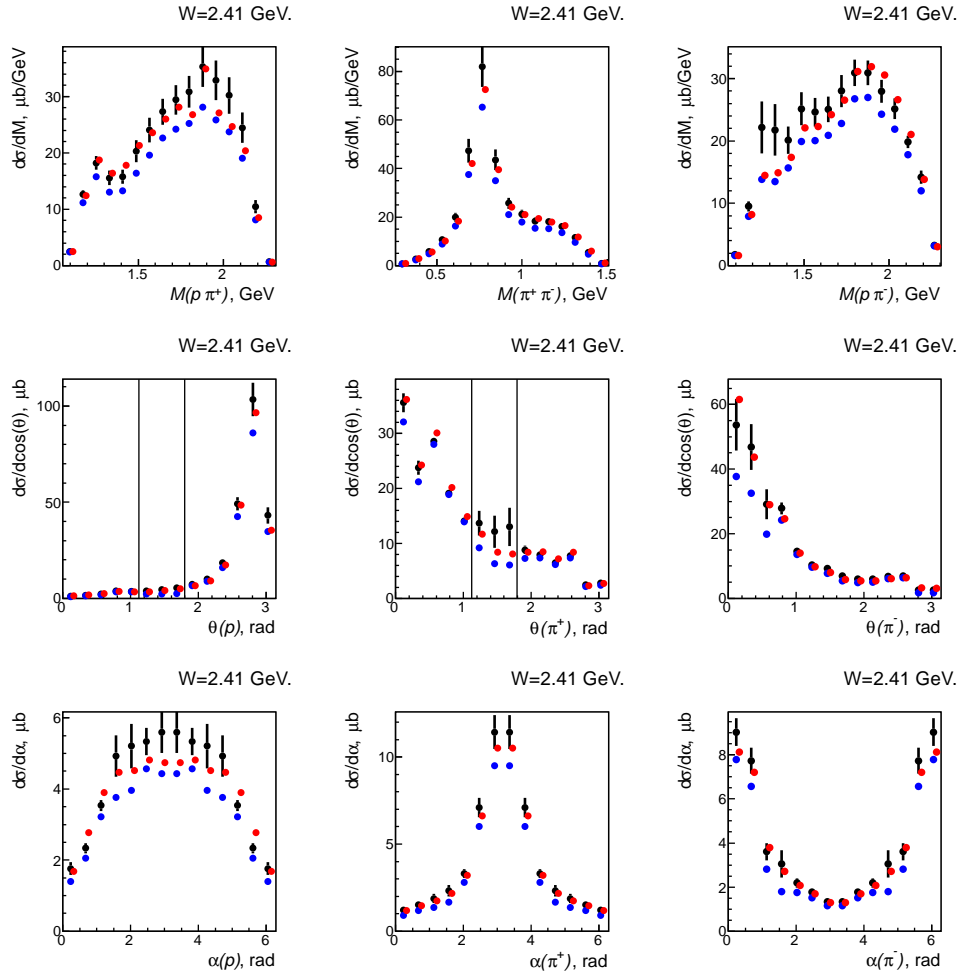


Figure 25: Single differential cross sections for  $2.4 \text{ GeV} < W < 2.425 \text{ GeV}$ . Cross section within CLAS acceptance is in red. Cross section with an artificial dead area is in blue. Artificial dead regions are marked with vertical lines, see text. Cross section accounted for **only artificial** dead area in simple approach is in black. See text for estimation of uncertainties for black dots.

### 5.5.2 Model approach

An other attempt to extrapolate the cross section into dead area of CLAS is to use model approach. Phenomenological model was developed in JLAB-MSU collaboration to describe two charged pion photo- and electroproduction off proton [4]. The model was successfully applied to describe the cross section of electroproduction in  $Q^2$  range from 0.25 GeV<sup>2</sup> to 1.5 GeV<sup>2</sup> [4]. All ingredients of the model are the same when describing reactions induced by real or virtual photons. Therefore, it was used for model extrapolation of the cross section.

The model has been adjusted to the experimental cross section in two steps. At first step we manually adjusted the model to the obtained cross section within CLAS acceptance. Since we do not know cross section in dead area the comparison of experiment data and model calculation can be done only within CLAS acceptance. Dead bins were determined in simulation and the model cross sections in that bins were set to be zero. Calculations were conducted with the same binning as it was used in experimental analysis. Results of the adjustment within CLAS acceptance are shown in Figs. 26–28. (We used slightly different acceptance in this fit.) Systematic uncertainties related to the kinematic fit are  $\approx 3\%$  of the integrated cross section. Therefore, we set uncertainties in differential cross sections to be  $0.03 \times \sqrt{N_p}$ , where  $N_p$  is the number of points in single differential cross sections.

Experimental cross section was extrapolated into dead area by setting the cross section in dead multidimensional bins to be equal to the model cross section. Extrapolated cross section is demonstrated in Figs. 29–31. It is compared with the cross section obtained in simple approach. Errors for the extrapolated cross are taken to be the half in the increase of the cross section with respect to the cross section within CLAS acceptance. Simple and model approaches give reasonably similar results. This gives us confidence that extrapolation works.

In second step the model cross section was adjusted to the extrapolated cross section obtained in first step. In this case adjustment was performed in full kinematics space. Results are demonstrated in Figs. 32–34. Quality of the fit is notably increased in comparison to the fit at the first step. Phenomenological JM model can describe general features of the cross section for  $W < 2$  GeV. Model extrapolation was not performed for higher  $W$ , as the model requires further development to describe the cross section for  $W > 2$  GeV.

Model extrapolation can be tested with the use of artificial dead zones in the same way as it was done in section 5.5.1. Figs. 35–36 demonstrate results of such test.

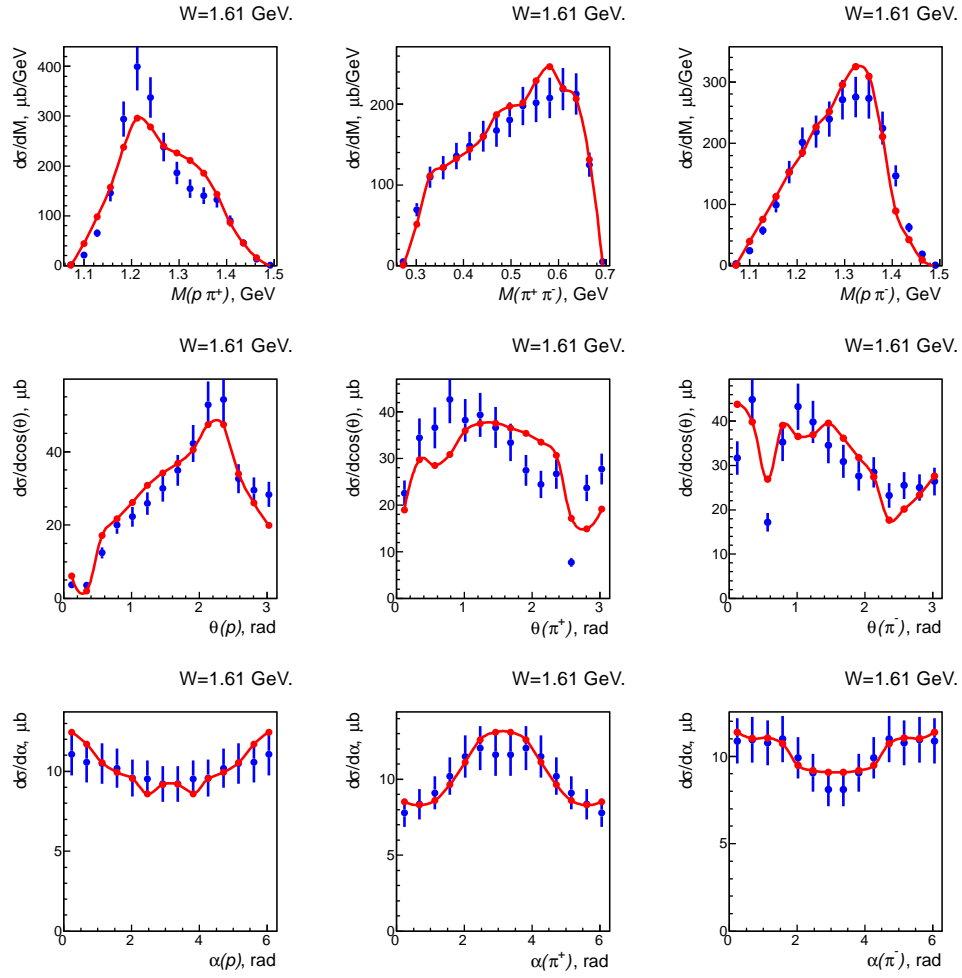


Figure 26: First step of model adjustment. Experimental (blue) and model (red) cross sections within CLAS acceptance for  $1.6 \text{ GeV} < W < 1.625 \text{ GeV}$ .

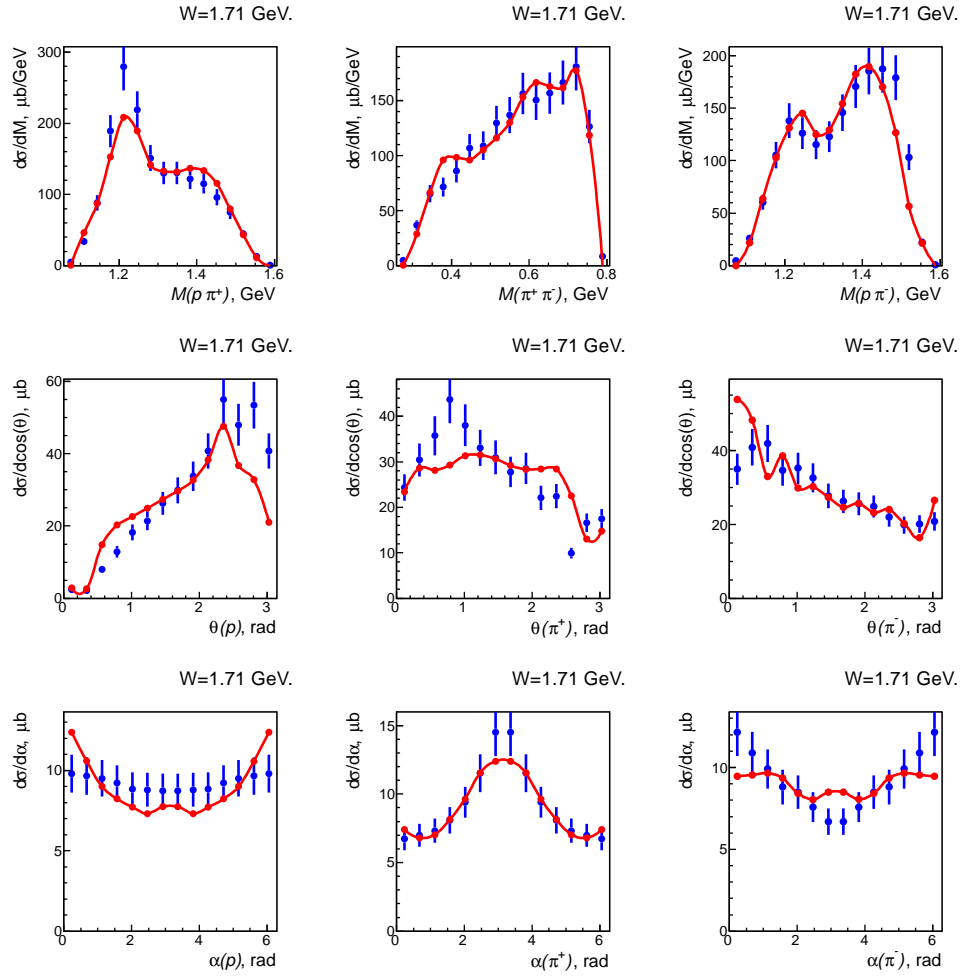


Figure 27: First step of model adjustment. Experimental (blue) and model (red) cross sections within CLAS acceptance for  $1.7 \text{ GeV} < W < 1.725 \text{ GeV}$ .

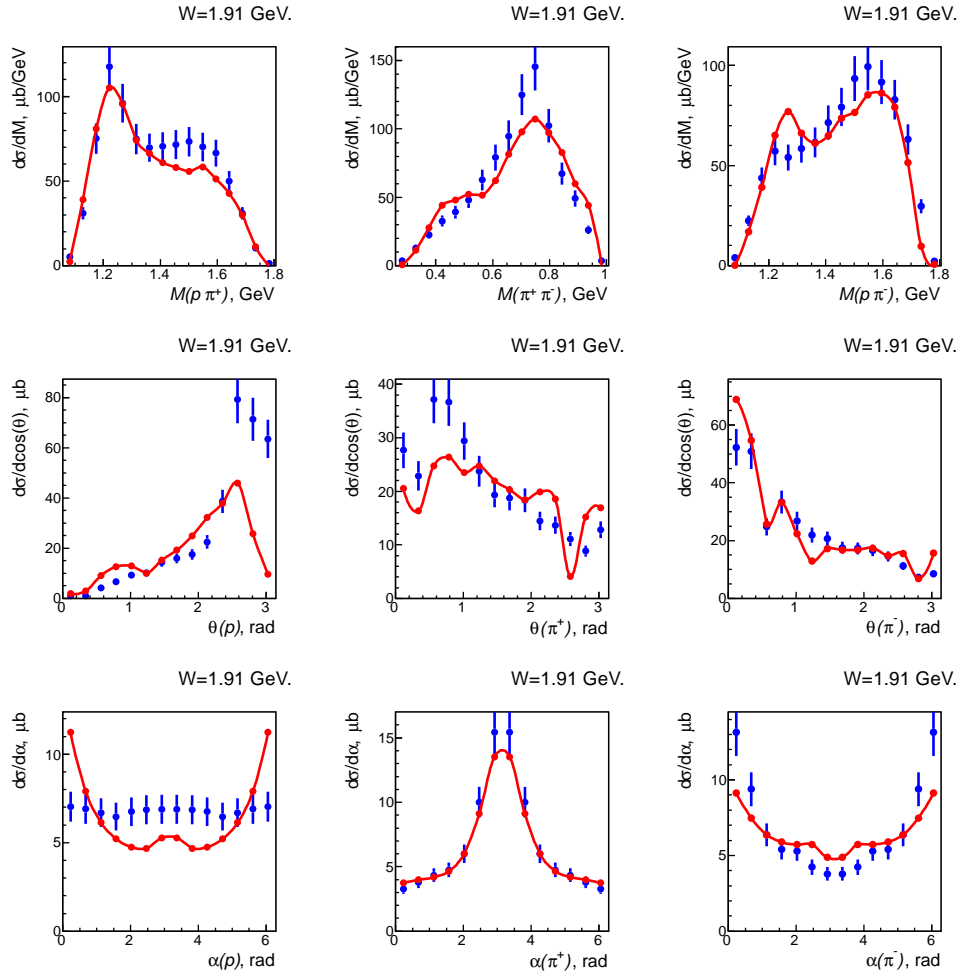


Figure 28: First step of model adjustment. Experimental (blue) and model (red) cross sections within CLAS acceptance for  $1.9 \text{ GeV} < W < 1.925 \text{ GeV}$ .



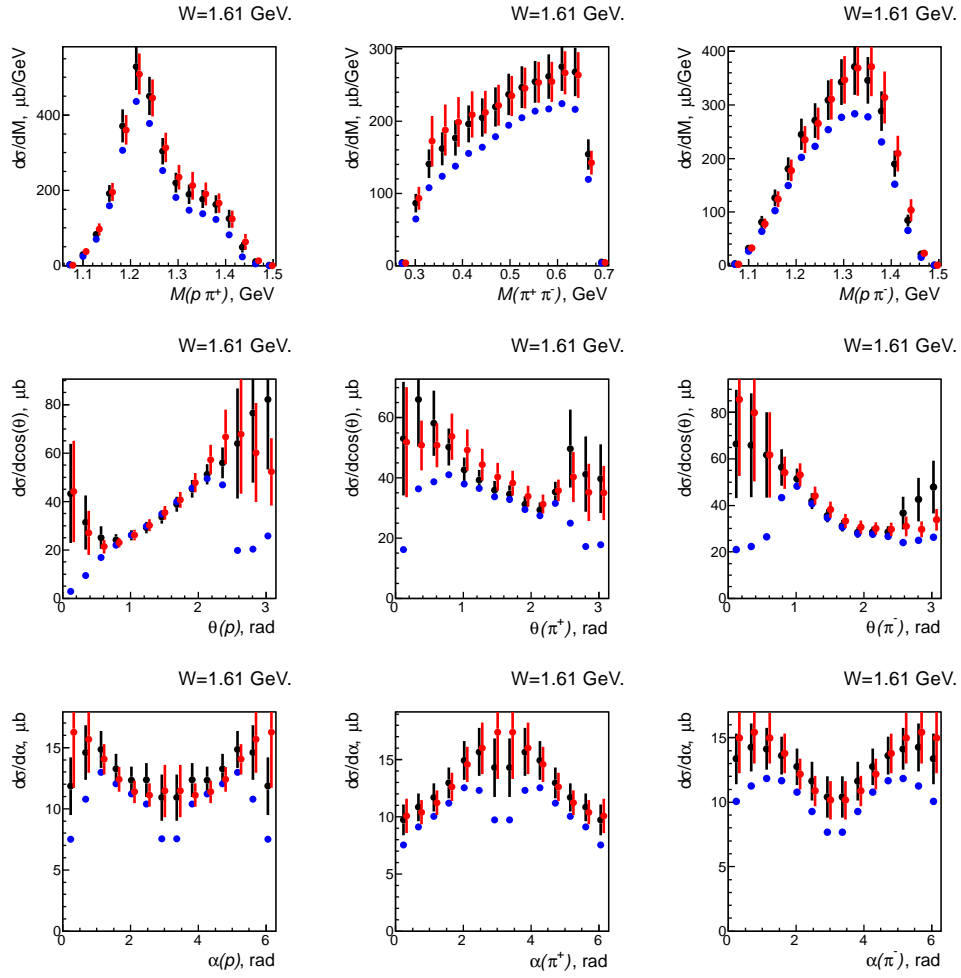


Figure 29: First step of model adjustment. Experimental cross section within CLAS acceptance is in blue. Cross section accounted for dead zone in simple approach is in black. Model extrapolated cross section is in red. Data are for  $1.6 \text{ GeV} < W < 1.625 \text{ GeV}$ .

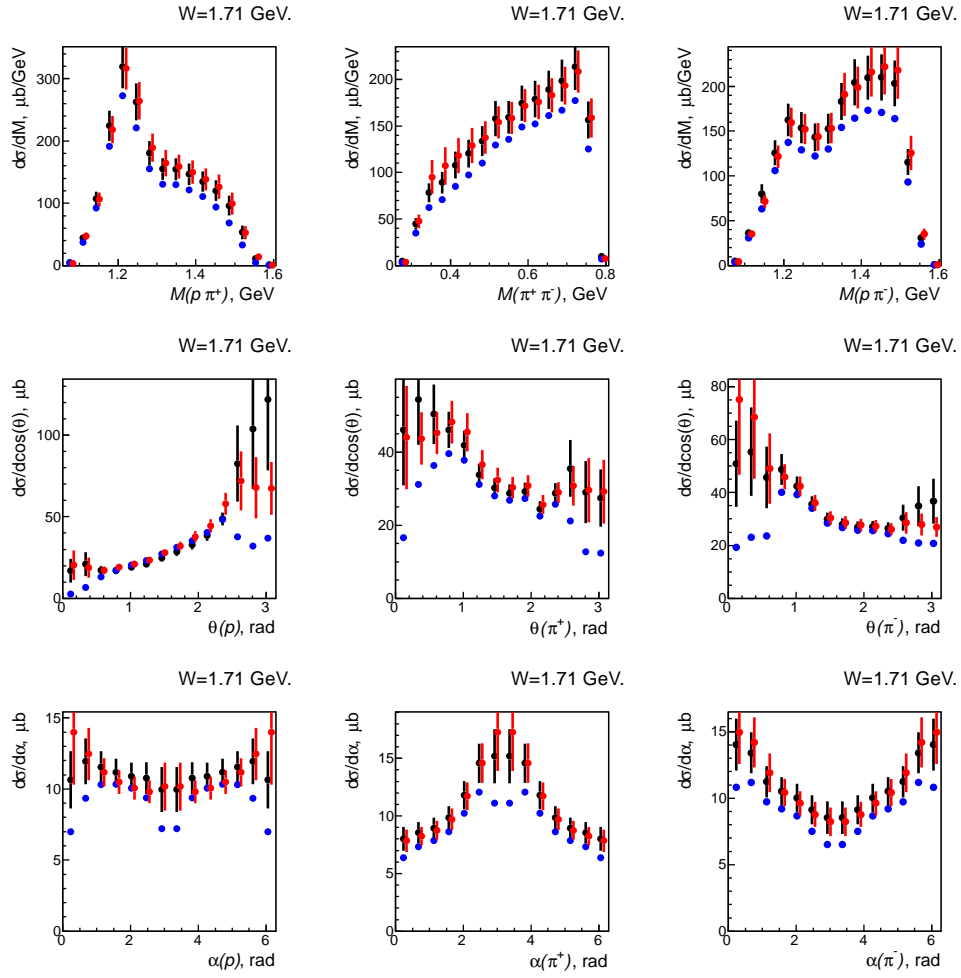


Figure 30: First step of model adjustment. Experimental cross section within CLAS acceptance is in blue. Cross section accounted for dead zone in simple approach is in black. Model extrapolated cross section is in red. Data are for  $1.7 \text{ GeV} < W < 1.725 \text{ GeV}$ .

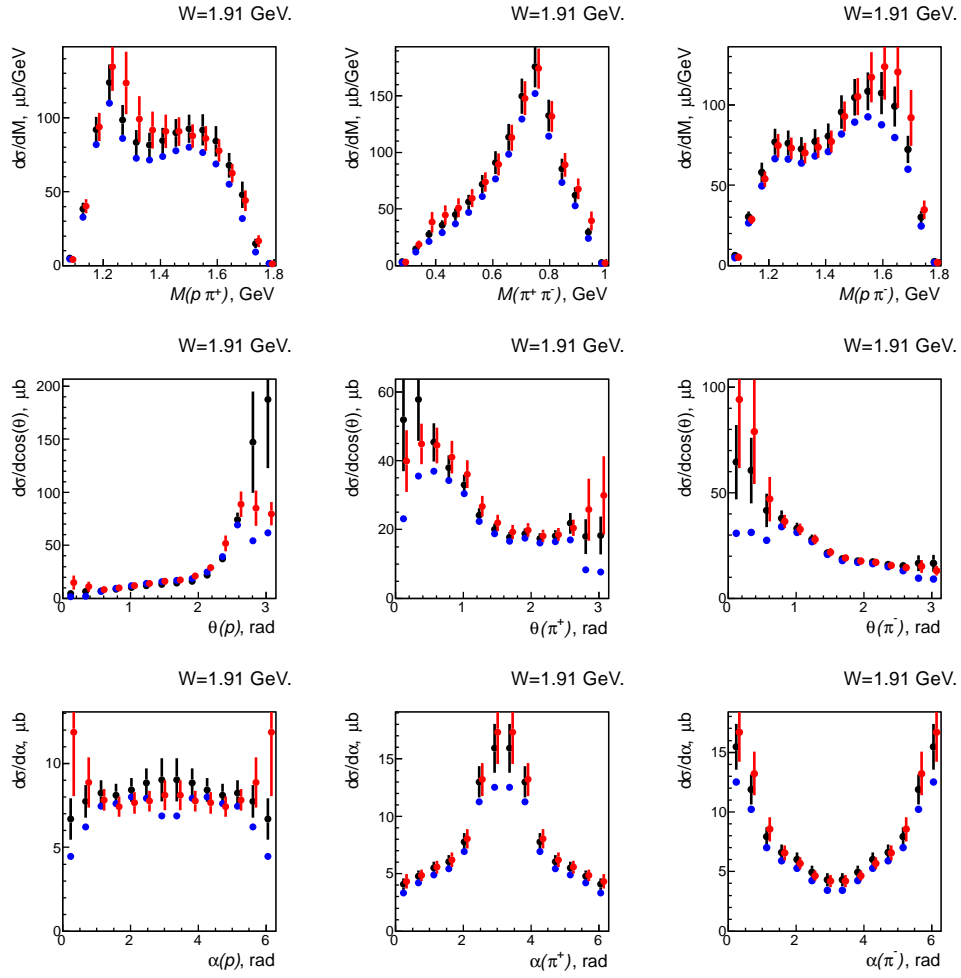


Figure 31: First step of model adjustment. Experimental cross section within CLAS acceptance is in blue. Cross section accounted for dead zone in simple approach is in black. Model extrapolated cross section is in red. Data are for  $1.9 \text{ GeV} < W < 1.925 \text{ GeV}$ .

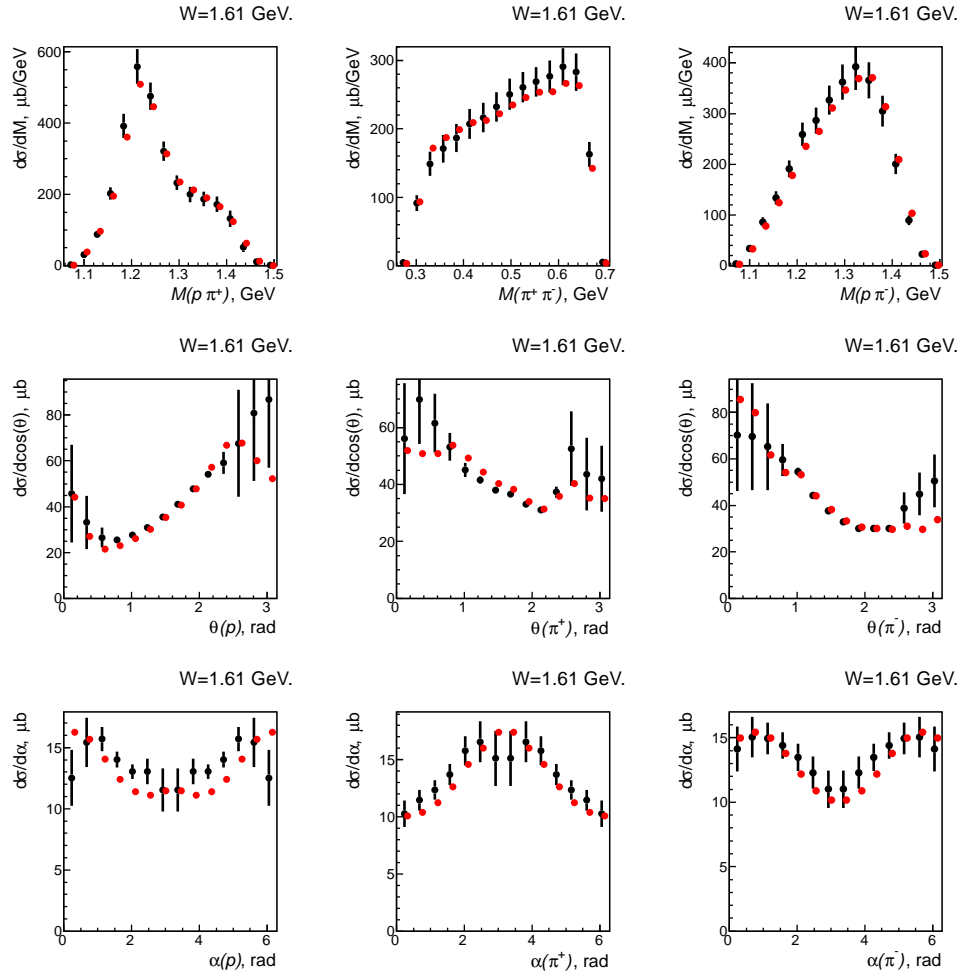


Figure 32: Comparison of the model cross sections adjusted in the second step (in red) with cross section accounted for dead zones in simple approach (in black). for  $1.6 \text{ GeV} < W < 1.625 \text{ GeV}$ .

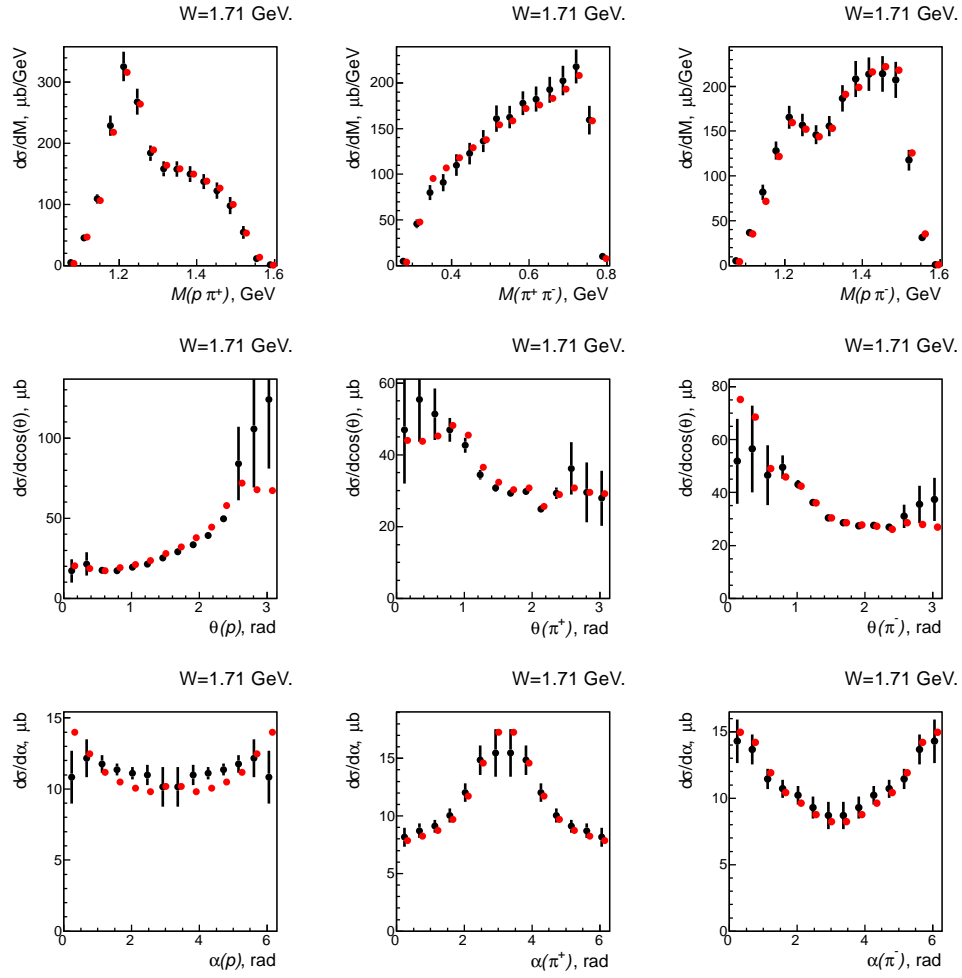


Figure 33: Comparison of the model cross sections adjusted in the second step (in red) with cross section accounted for dead zones in simple approach (in black). for for  $1.7 \text{ GeV} < W < 1.725 \text{ GeV}$ .

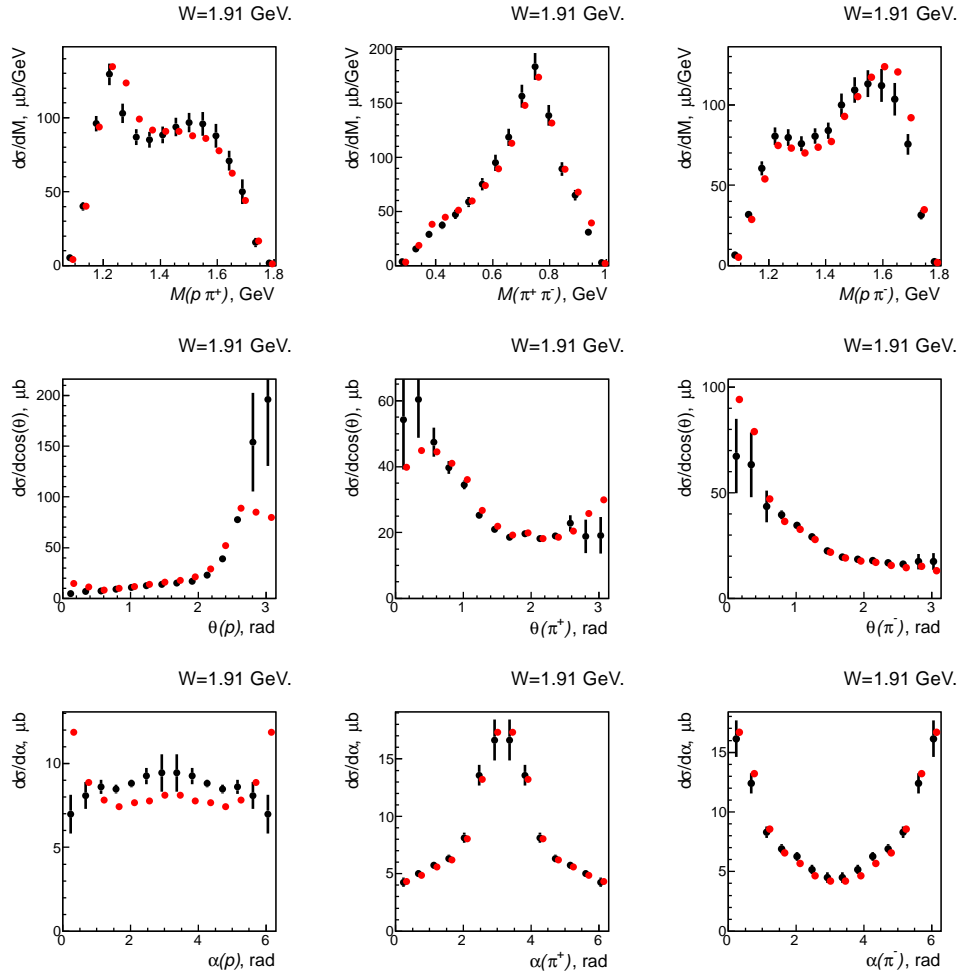


Figure 34: Comparison of the model cross sections adjusted in the second step (in red) with cross section accounted for dead zones in simple approach (in black). for  $1.9 \text{ GeV} < W < 1.925 \text{ GeV}$ .

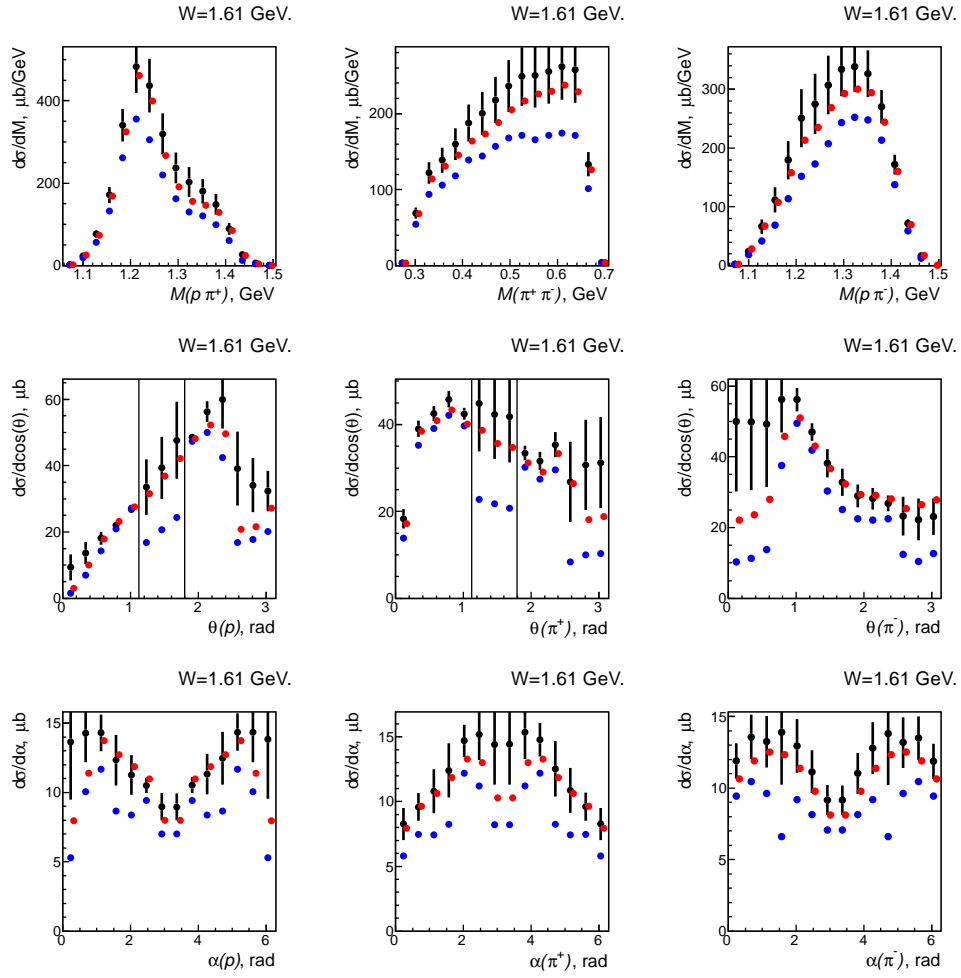


Figure 35: Single differential cross sections for  $1.6 \text{ GeV} < W < 1.625 \text{ GeV}$ . Cross section within CLAS acceptance is in red. Cross section with an artificial dead area is in blue. Artificial dead regions are marked with vertical lines, see text. Cross section accounted for **only artificial** dead area in model approach is in black. See text for estimation of uncertainties for black dots.

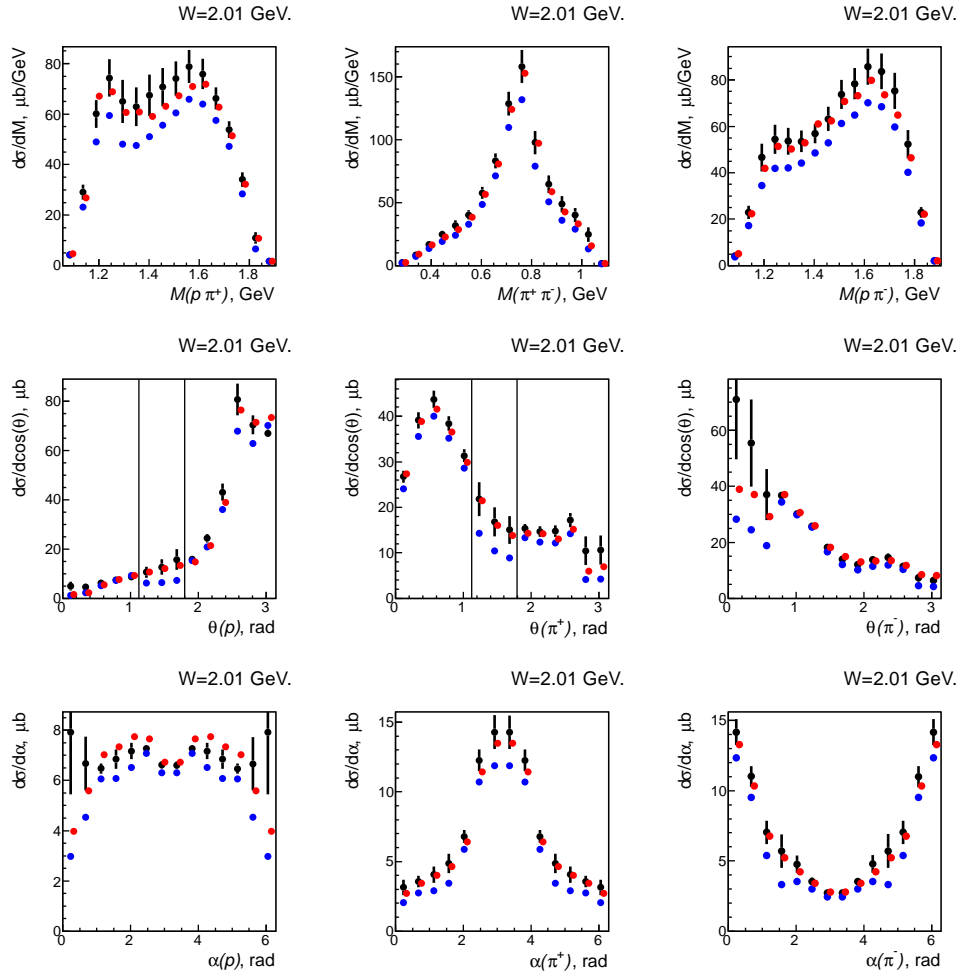


Figure 36: Single differential cross sections for  $2.0 \text{ GeV} < W < 2.025 \text{ GeV}$ . Cross section within CLAS acceptance is in red. Cross section with an artificial dead area is in blue. Artificial dead regions are marked with vertical lines, see text. Cross section accounted for **only artificial** dead area in model approach is in black. See text for estimation of uncertainties for black dots.



## 6 Systematic uncertainties

Systematic uncertainties result from inaccuracy in the measurement inherent to the detector system. Systematic uncertainties are summarized in Table 2. These are uncertainties for the integrated cross section. The distributions over kinematic variables of the uncertainties represented in first three lines of the table are not known.

Comparison of the cross sections obtained from different topologies (see section 5.3) provides a good test for an accuracy of the cross section calculation and can be used as a cross check for the total systematic uncertainty apart for uncertainties related to the accounting for dead area. Averaged errors of cross sections from different topologies was estimated to be  $\approx 4\%$  and it is consistent with Table 2, as the combination of uncertainties except for the uncertainties related to the accounting for dead area of CLAS is 3.5%.

The largest source of uncertainties is related to the presence of dead area in the CLAS detector and the cross section can not be measured in the whole kinematics space. Extrapolation of the cross section can be done in model way and procedure of accounting for dead area introduce substantial uncertainties. The distribution of these uncertainties is highly non uniform in the differential cross sections. They vary from few percent to 50 percent. Statistical errors are negligible in comparison with other errors.

Since data have reasonably low uncertainties ( $< 3\text{--}4\%$ ) only in a limited kinematic space, then physic analysis can be restricted to that space. Alternatively, data in the whole kinematic space may be used taking an account large errors in certain area.

Table 2: Systematic uncertainties for the integrated cross section.

Source	Systematic error
Photon flux correction	1.0%
Particle detection efficiency correction	1.5%
Kinematic fit	3.0%
Accounting for CLAS dead area	12.0%

## 7 Comparison with the available world data

The most recent data on the reaction  $\gamma p \rightarrow p' \pi^+ \pi^-$  proton with photons from 1.6 to 2.8 GeV are obtained using SAPHIR spectrometer at ELSA [21]. There are also data for the integrated cross section from ABBHHM collaboration [18].

Fully integrated cross cross section in comparison with available world data is presented in Fig. 37. Cross section within CLAS acceptance are about 10% lower than ELSA and

ABBHHM data for  $W < 2.6$  GeV. Extrapolated data coincide with world data within uncertainties. Integrated cross section is not reliable for  $W$  more that  $\approx 2.6$  GeV, as the more is  $W$  the larger part of the cross section is in the kinematics space with considerable contribution of dead area and the accuracy of extrapolation is impaired.

Percentage of the “lost” cross section can be estimated as a difference between blue and black dots, see Fig. 37. Statistical errors are negligible and the main source of systematic uncertainties is related to the extrapolation procedure.

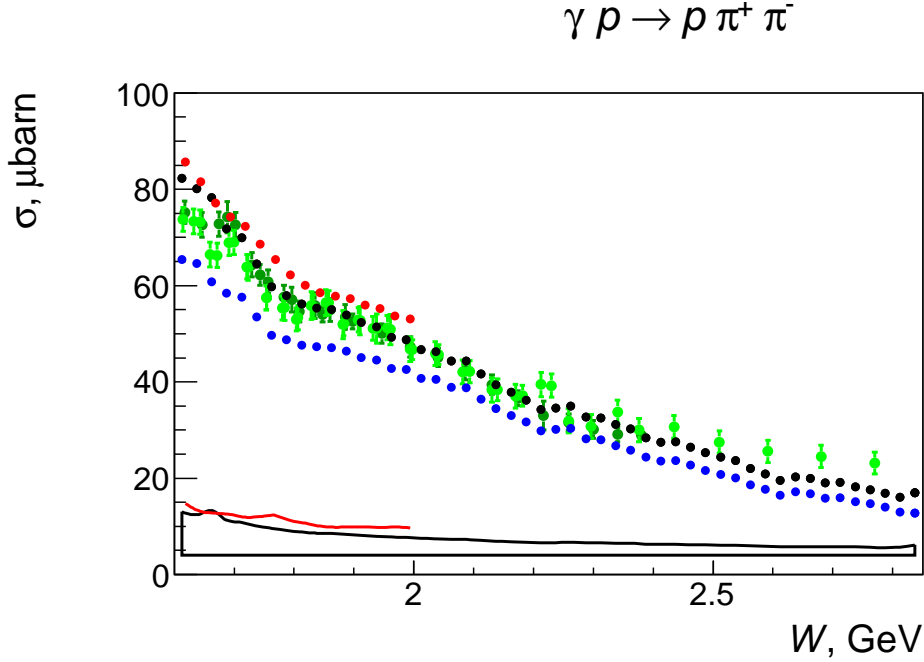


Figure 37: Comparison of the obtained integrated cross section with the world data. Cross section within CLAS acceptance is shown in blue. Cross section accounted for dead zone contribution is shown in black (simple approach) and red (model extrapolation). Green dots correspond to the experiments from [21] (dark green) and 37 (light green). Statistical errors are negligible. Uncertainties related to the accounting for dead area are shown at the bottom of the plot.

A big interest is to compare differential cross section  $\frac{d\sigma}{d\theta}$ , since the CLAS inefficient area is located at small and large polar angles of particles. In [21] data are presented as a function of Mandelstam variable  $t_{\pi^+\pi^-} = (p_p - p_{p'})^2$ . Cross section  $\frac{d\sigma}{d\theta_p}$  can not be calculated from  $\frac{d\sigma}{dt_{\pi^+\pi^-}}$ , therefore, we compare distributions  $\frac{d\sigma}{dt_{\pi^+\pi^-}}$ . There is a correlation between  $\frac{d\sigma}{d\theta_p}$  and  $\frac{d\sigma}{dt_{\pi^+\pi^-}}$  in the sense, that on the average small values of  $t_{\pi^+\pi^-}$  correspond to large values of  $\theta_p$  and vice versa.

Comparison of  $t$ -distribution from CLAS and SAPHIR data is shown in Fig. 38. One can see a reasonable coincidence in the range of  $t$  from  $\approx 0.2$  to  $\approx 1.1$  GeV. This range correspond to the CLAS acceptance area. Out of that range the cross section has substantial contribution of dead area and one can see notable discrepancy at small and large  $t$ . In part disagreement may be due to somewhat different binning in  $W$  that were used in CLAS and SAPHIR data. In general, obtained cross section is not much reliable in areas with large contribution of dead area also because particle detection efficiency in CLAS may not exactly coincide with efficiency derived from Monte Carlo, see section 4.2.

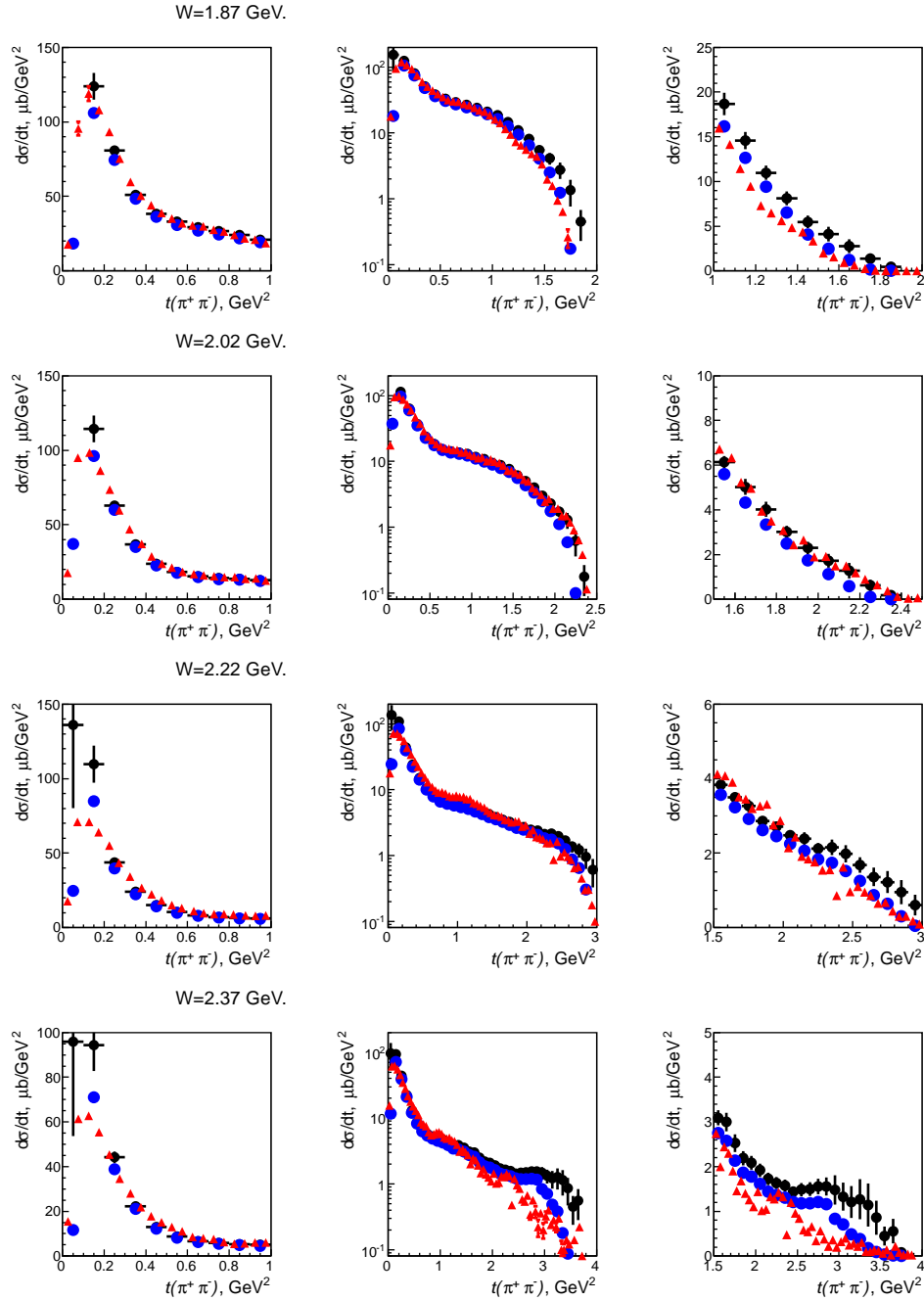


Figure 38: Comparison of distributions over  $t \equiv t_{\pi^+\pi^-}$  from [21] (red triangles) with CLAS data. Cross section within CLAS acceptance is shown in blue. Cross section accounted for dead area in simple approach is shown in black. Distribution in each  $W$  bin is plotted in three variants: the cross section for small  $t$  (left column), in the whole range of  $t$  in logarithmic scale (central column) and for large  $t$  (right column). CLAS data are in  $W$  intervals:  $[1.850; 1.875]$ ,  $[2.000; 2.025]$ ,  $[2.200; 2.225]$  and  $[2.350; 2.375]$ . Data from [21] are in  $W$  intervals:  $[1.82; 1.87]$ ,  $[2.02; 2.06]$ ,  $[2.20; 2.24]$  and  $[2.36; 2.40]$ .

## 8 Results

Fully integrated as well as 1-fold and 2-fold differential cross sections for the reaction  $\gamma p \rightarrow p\pi^+\pi^-$  were obtained in  $W$  range 1.6–2.5 GeV. For  $W > 2.5$  GeV the cross sections are not reliable due to big contribution of dead zones. Attempts were made to extrapolate the cross sections into inefficient CLAS zones. In total  $\approx 5 \times 10^8$  reaction events were selected out of  $\approx 20 \times 10^8$  triggers with two charged track requirement.

Fully integrated cross section has been presented in section 7.

### 8.1 1-fold differential cross sections

Nine 1-fold differential cross sections were obtained:  $\frac{d\sigma}{dM}$ ,  $\frac{d\sigma}{d\theta}$  and  $\frac{d\sigma}{d\alpha}$ , where  $M$  is  $M(p, \pi^+)$ ,  $M(\pi^+, \pi^-)$  or  $M(\pi^-, p)$ ;  $\theta$  is  $\theta_p$ ,  $\theta_{\pi^+}$  or  $\theta_{\pi^-}$  and  $\alpha$  is  $\alpha_p$ ,  $\alpha_{\pi^+}$  or  $\alpha_{\pi^-}$ . Figs. 39 through 44 demonstrate examples of single differential cross sections obtained for  $W$  from 1.6 to 2.8 GeV with 25 MeV bin width.

The cross sections accounting for dead area of CLAS in simple and model approaches are shown in black and red respectively. Blue dots display the cross sections within CLAS acceptance. Model extrapolation was performed for  $W < 2.1$  GeV, since model needs further development to describe the reaction mechanisms for higher  $W$ . Statistical errors are negligible. Accounting for dead area of CLAS in two approaches gives on the average similar results. Though in ranges with large contribution of dead multidimensional bins these approaches may give substantially different results. Probably, the cross section in such ranges should not be used in physics analysis. Error bars give uncertainties related to the extrapolation of the cross section into dead area, which are dominant. Statistical uncertainties are negligible.

### 8.2 2-fold differential cross sections

Twenty four 2-fold differential cross sections were obtained:

$\frac{d^2\sigma}{dM dM'}$ ,  $\frac{d^2\sigma}{dM d\cos(\theta)}$ ,  $\frac{d^2\sigma}{dM d\alpha}$  and  $\frac{d^2\sigma}{d\cos(\theta) d\alpha}$ , where  $M$ ,  $M'$ ,  $\theta$  and  $\alpha$  are kinematics variables as in previous section.

Figs 45 through 48 present examples of 2-fold differential cross sections with they uncertainties including both systematic and statistical. Uncertainties are designated as  $\Delta$  and shown in separate plots. These are extrapolated in simple approach cross sections. As it was mentioned above extrapolation procedure is not reliable when the contribution of dead multidimensional bins becomes large. 2-dimensional bins having more that 50% of dead multidimensional bins are removed from the plots and such 2-dimensional bins are marked with X-like signs.

Fig. 49 through 60 present 2-fold differential cross sections obtained for  $W$  bins from 1.6 to 2.6 GeV with 25 MeV bin width. These are extrapolated in simple approach cross sections.

## 9 Conclusion

Fully integrated cross section as well as 9 1-fold and 24 2-fold differential cross section were obtained in  $W$ -bins from 1.6 to 2.5 GeV with 25 MeV bin width.

Due to the presence of inefficient area of CLAS multidifferential cross section was not measured in some number of multidimensional bins. Two attempts were performed to account for dead area in 1- and 2-fold distributions. In regions, where the contribution of dead multidimensional bins does not exceed  $\approx 30\%$  the cross sections obtained in two approaches coincide within errors at least for  $W < 2.0$  GeV, as JM model has been adjusted to reproduce single differential cross sections for  $W < 2.0$  GeV. This gives us assurance that the extrapolated cross section is reliable within its uncertainty in that regions.

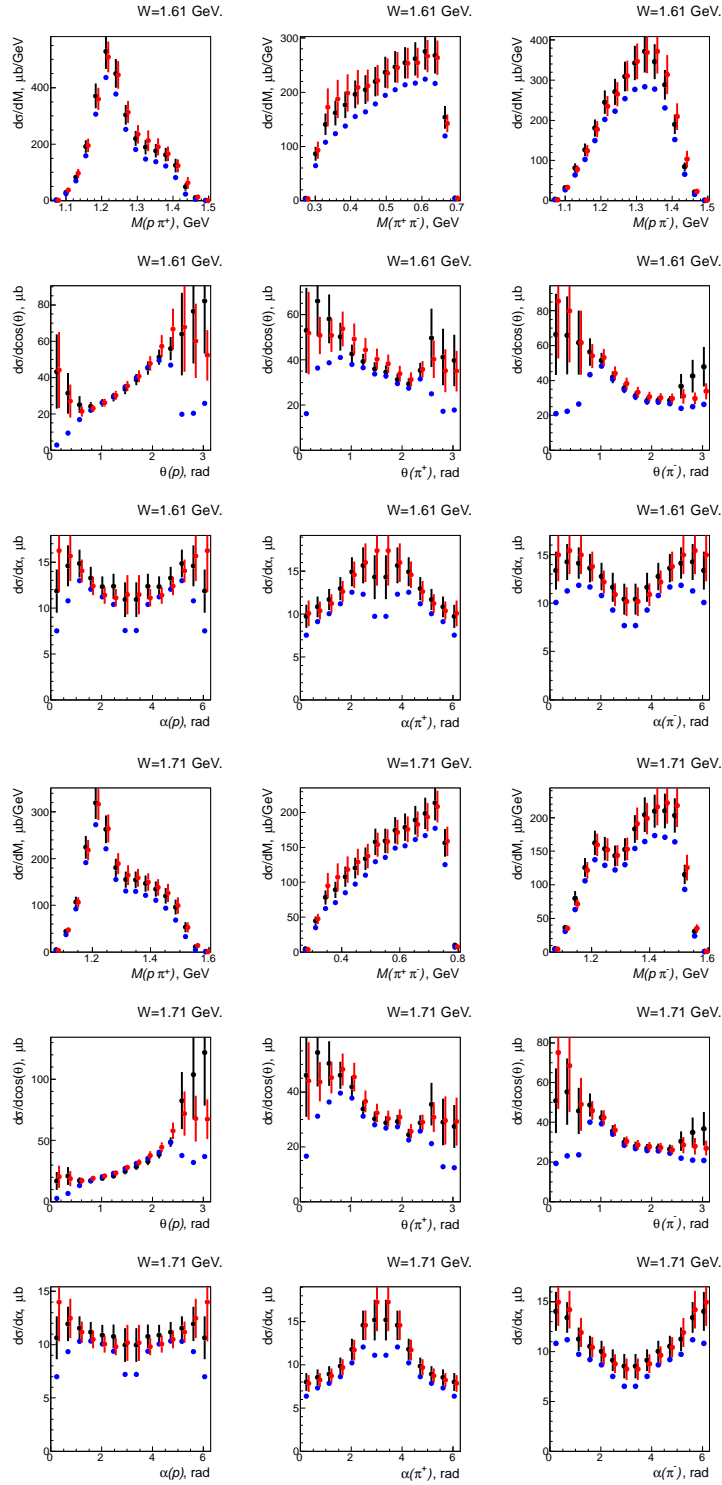


Figure 39: 1-fold differential cross section for W-bins as marked at upper right-hand corner of each plot. Cross section within CLAS acceptance is in blue. Cross section extrapolated in simple approach is in black, in model approach is in red. See text for kinematics variable definitions and uncertainties.

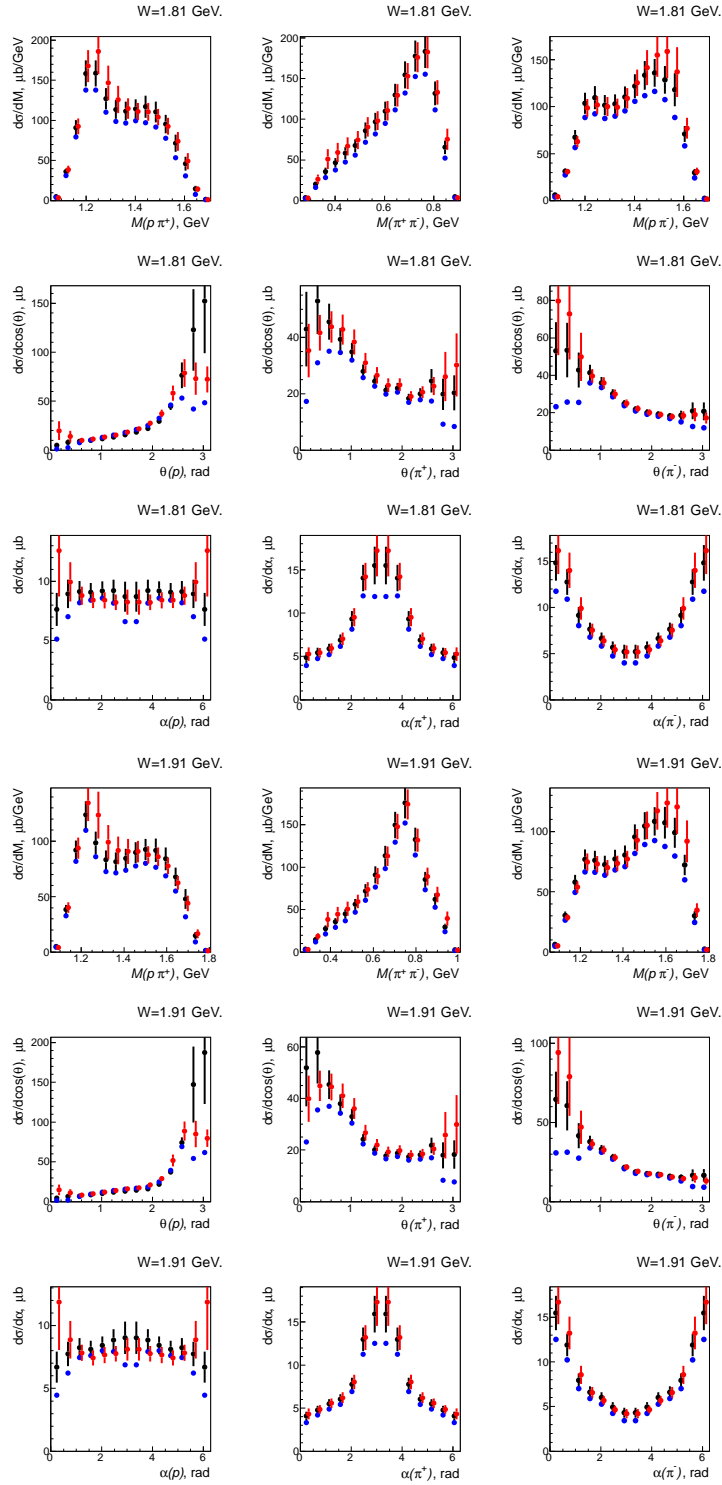


Figure 40: 1-fold differential cross section for W-bins as marked at upper right-hand corner of each plot. Cross section within CLAS acceptance is in blue. Cross section extrapolated in simple approach is in black, in model approach is in red. See text for kinematics variable definitions and uncertainties.



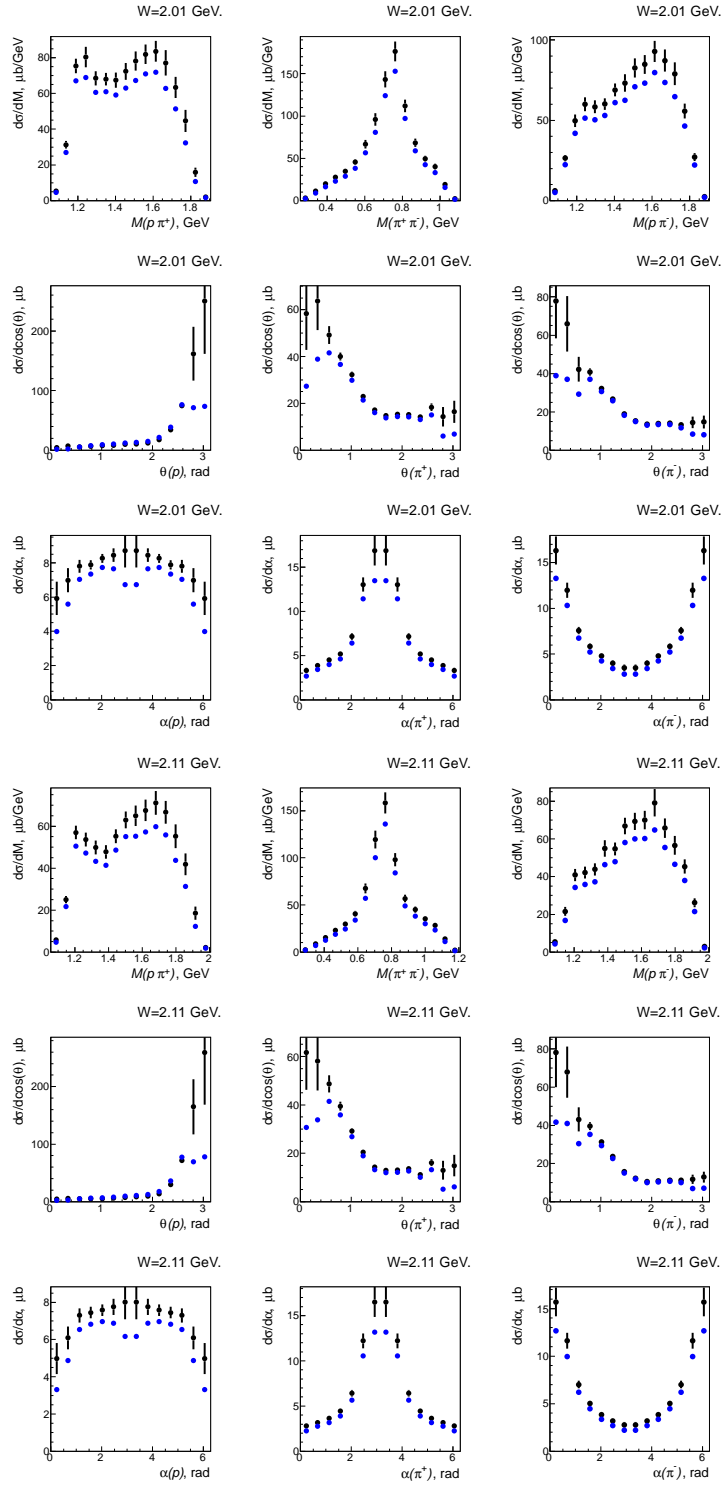


Figure 41: 1-fold differential cross section for W-bins as marked at upper right-hand corner of each plot. Cross section within CLAS acceptance is in blue. Cross section extrapolated in simple approach is in black, in model approach is in red. See text for kinematics variable definitions and uncertainties.

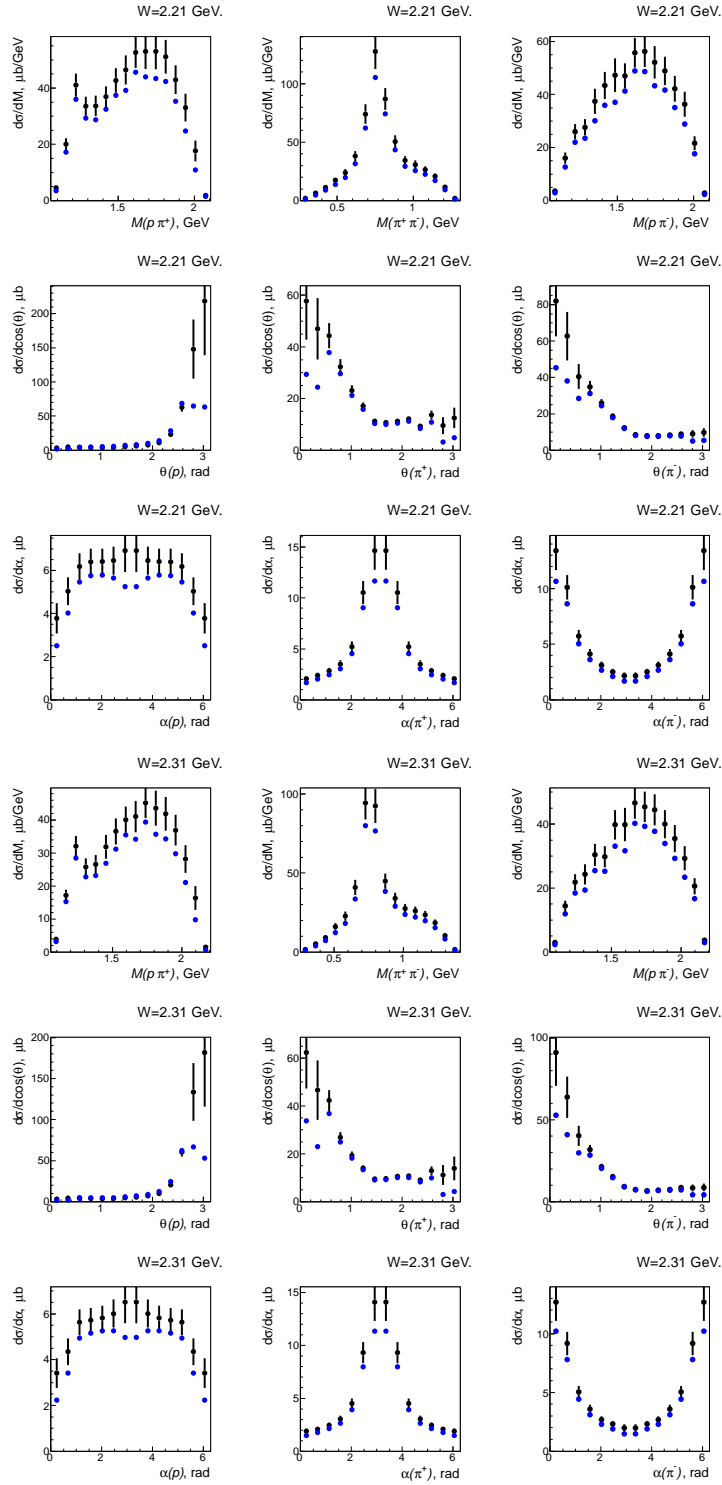


Figure 42: 1-fold differential cross section for W-bins as marked at upper right-hand corner of each plot. Cross section within CLAS acceptance is in blue. Cross section extrapolated in simple approach is in black. See text for kinematics variable definitions and uncertainties.

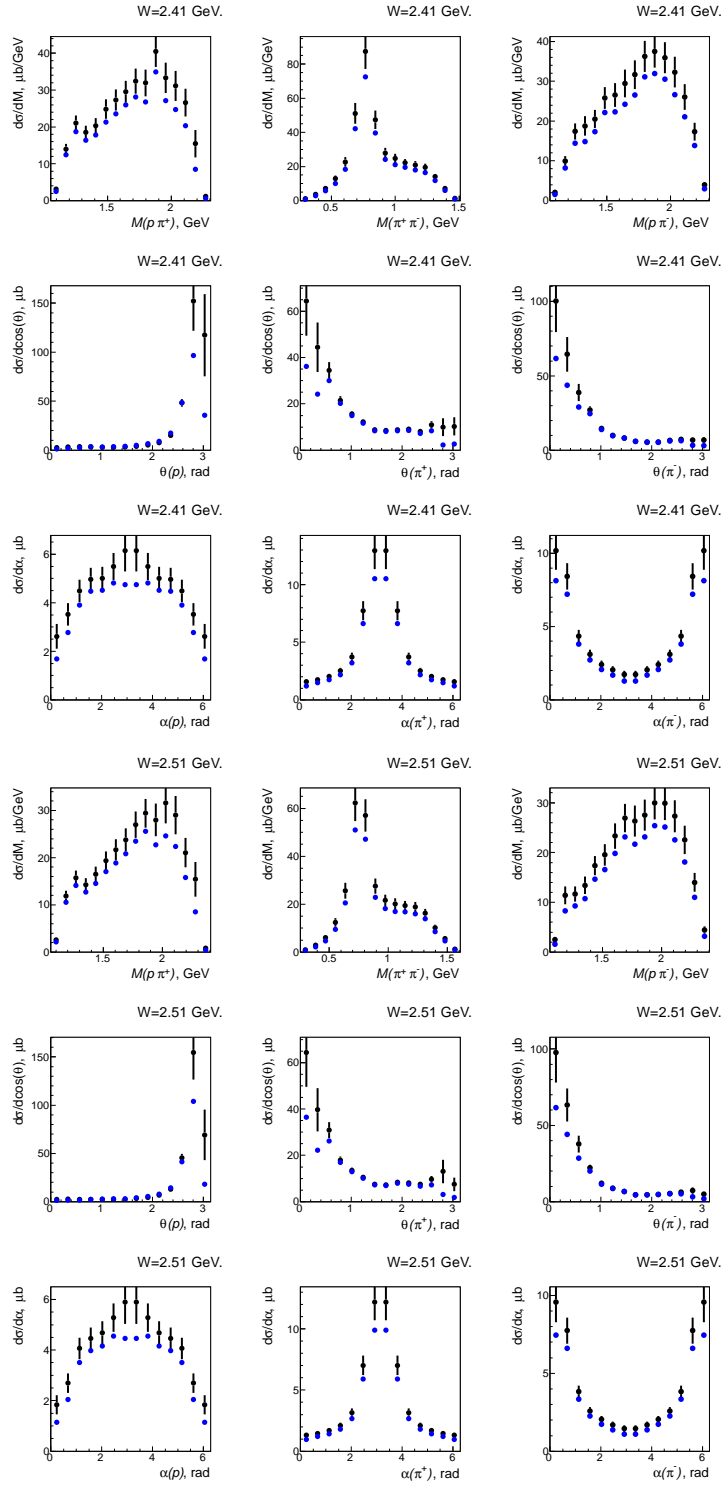


Figure 43: 1-fold differential cross section for W-bins as marked at upper right-hand corner of each plot. Cross section within CLAS acceptance is in blue. Cross section extrapolated in simple approach is in black. See text for kinematics variable definitions and uncertainties.

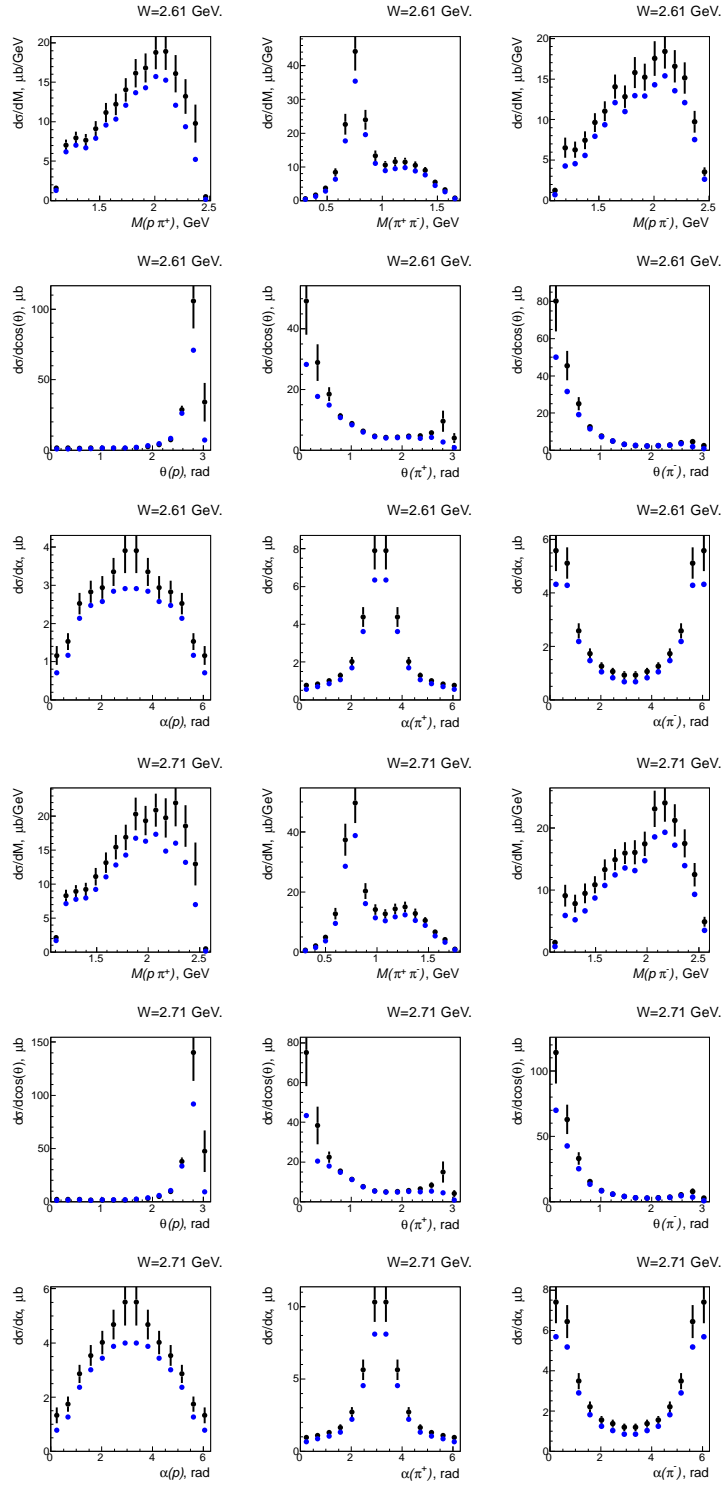
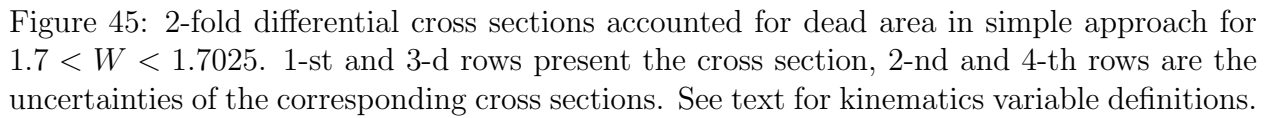


Figure 44: 1-fold differential cross section for W-bins as marked at upper right-hand corner of each plot. Cross section within CLAS acceptance is in blue. Cross section extrapolated in simple approach is in black. See text for kinematics variable definitions and uncertainties.



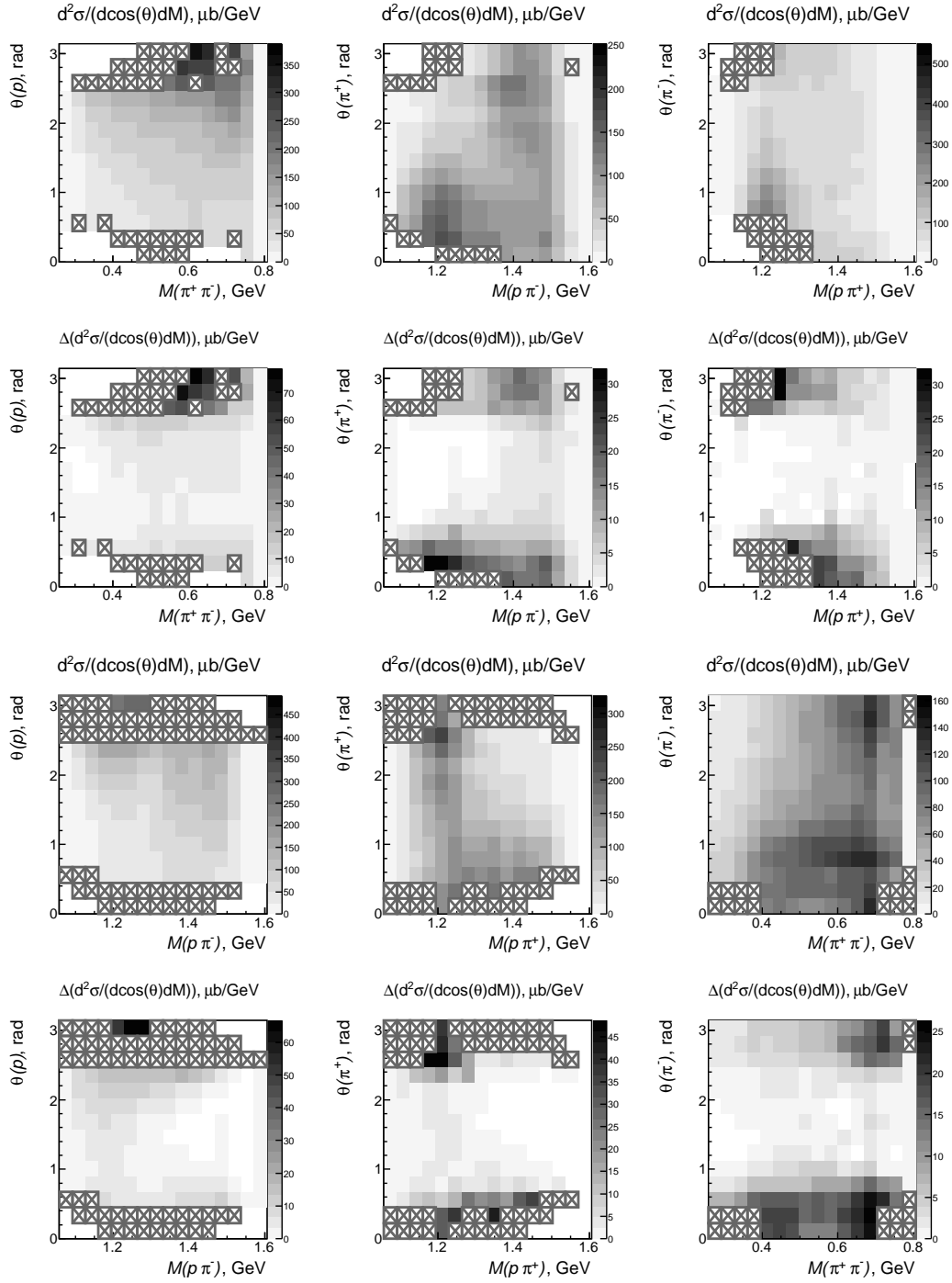


Figure 46: 2-fold differential cross sections accounted for dead area in simple approach for  $1.7 < W < 1.7025$ . 1-st and 3-d rows present the cross section, 2-nd and 4-th rows are the uncertainties of the corresponding cross sections. See text for kinematics variable definitions.

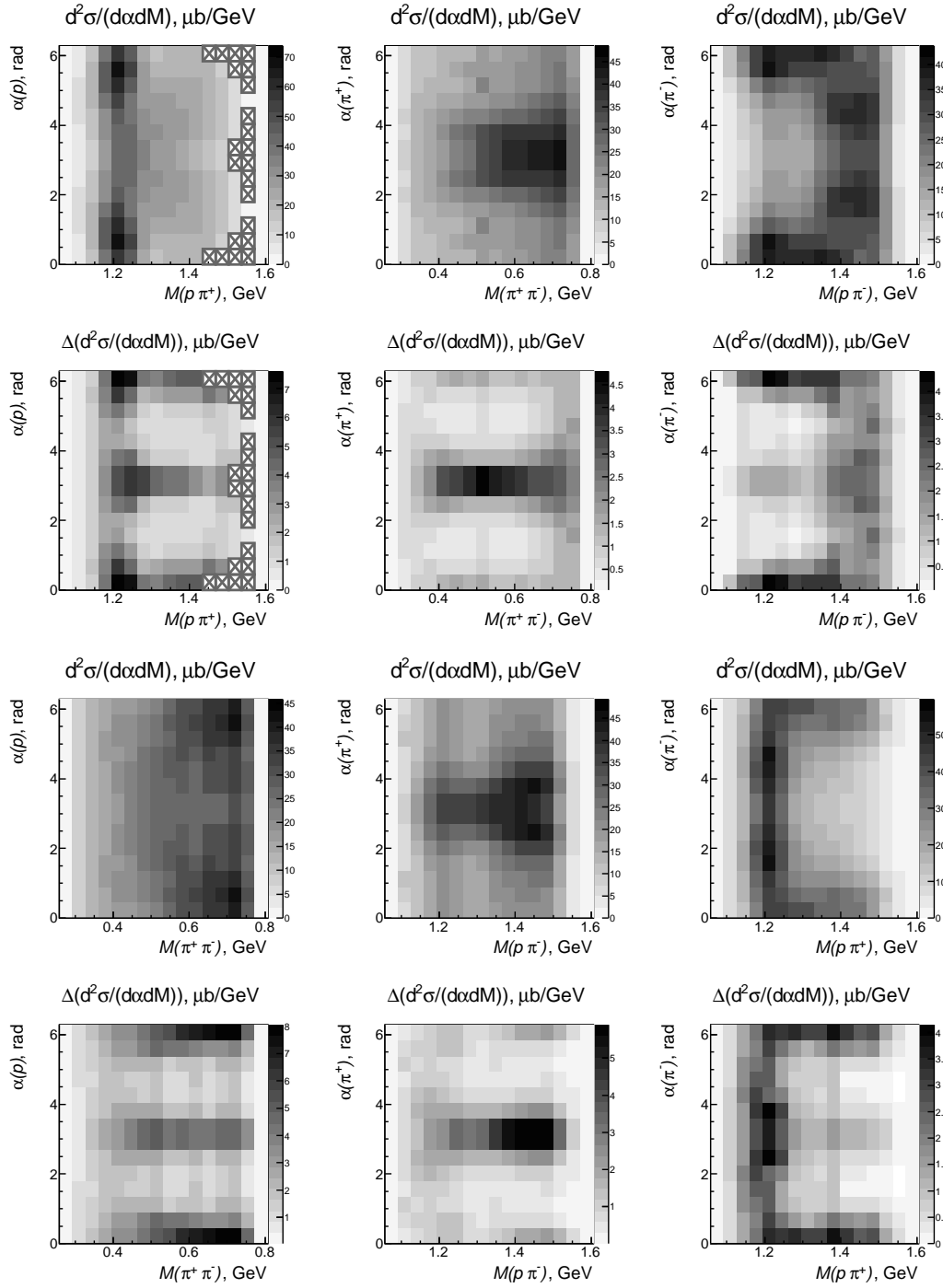


Figure 47: 2-fold differential cross sections accounted for dead area in simple approach for  $1.7 < W < 1.7025$ . 1-st and 3-d rows present the cross section, 2-nd and 4-th rows are the uncertainties of the corresponding cross sections. See text for kinematics variable definitions.

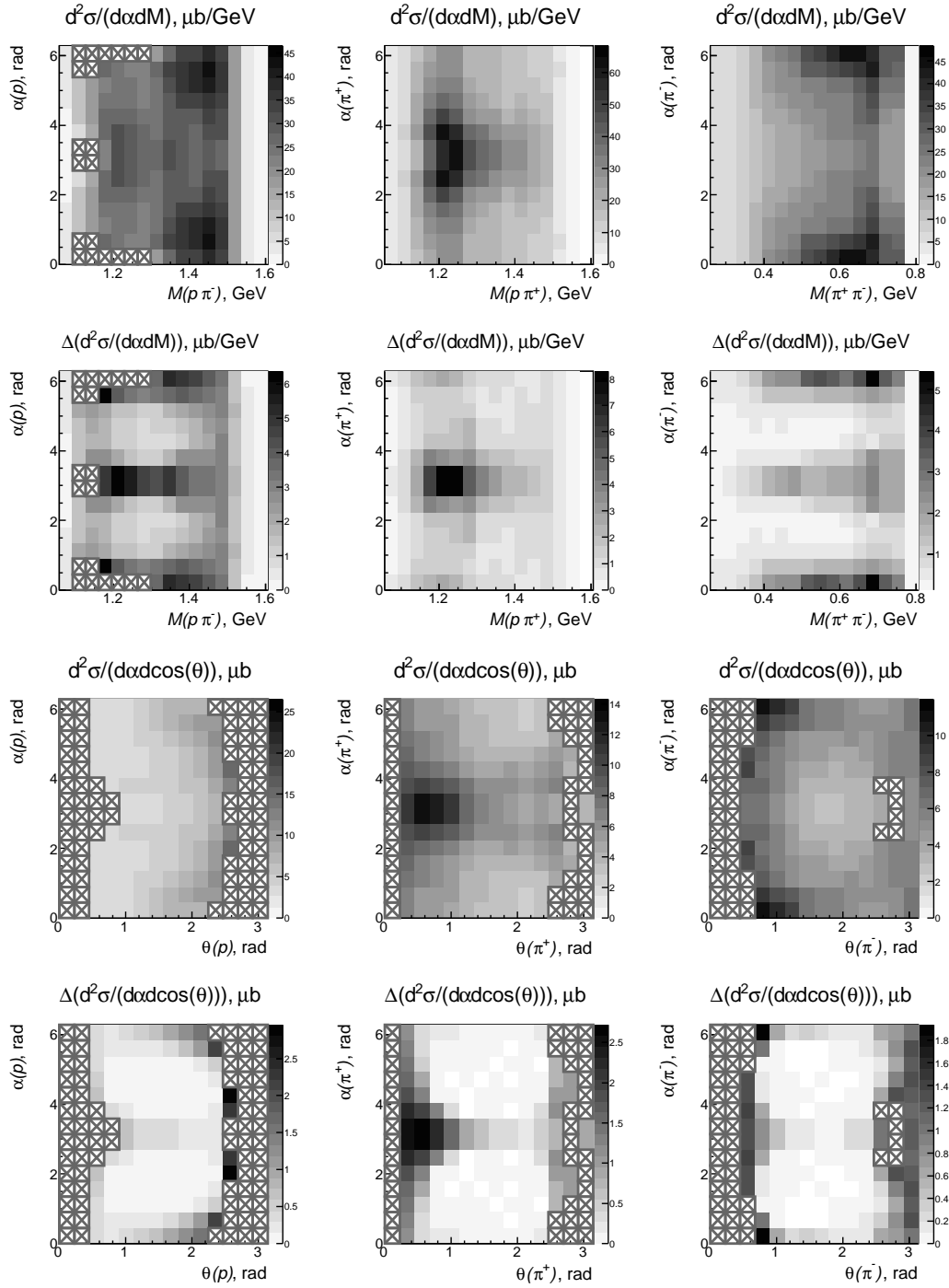


Figure 48: 2-fold differential cross sections accounted for dead area in simple approach for  $1.7 < W < 1.7025$ . 1-st and 3-d rows present the cross section, 2-nd and 4-th rows are the uncertainties of the corresponding cross sections. See text for kinematics variable definitions.



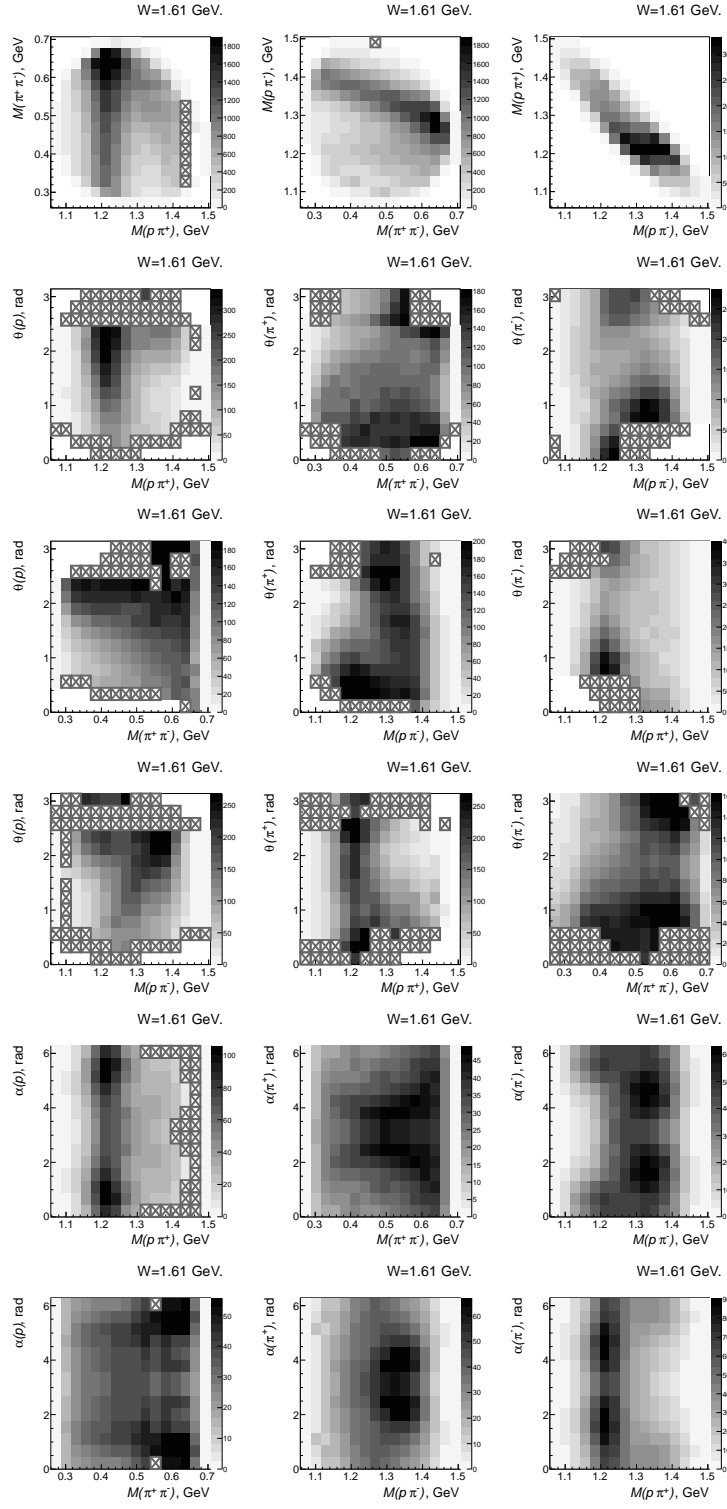


Figure 49: 2-fold differential cross sections accounted for dead area in simple approach. W-bins are marked on tops of the plots. See text for kinematics variable definitions.

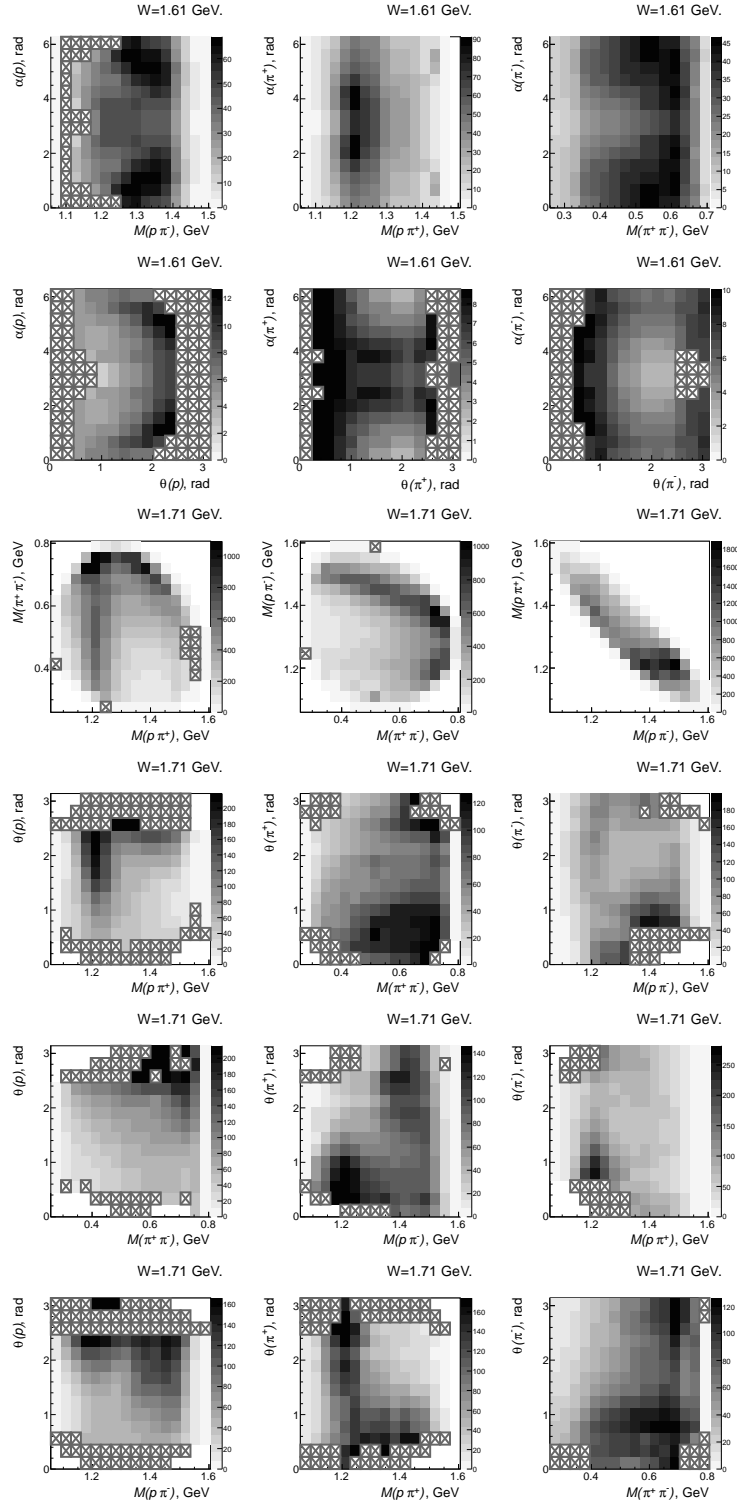


Figure 50: 2-fold differential cross sections accounted for dead area in simple approach. W-bins are marked on tops of the plots. See text for kinematics variable definitions.

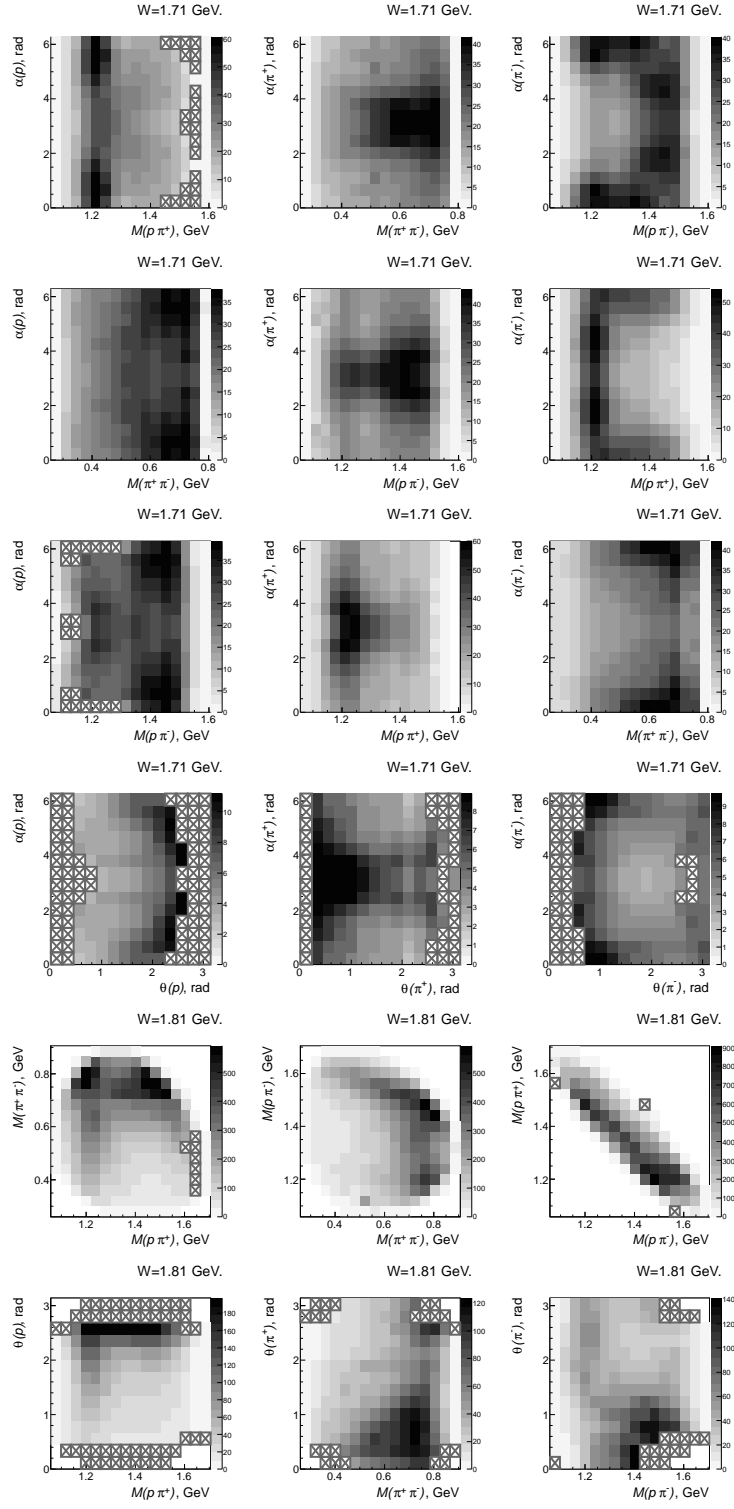


Figure 51: 2-fold differential cross sections accounted for dead area in simple approach. W-bins are marked on tops of the plots. See text for kinematics variable definitions.

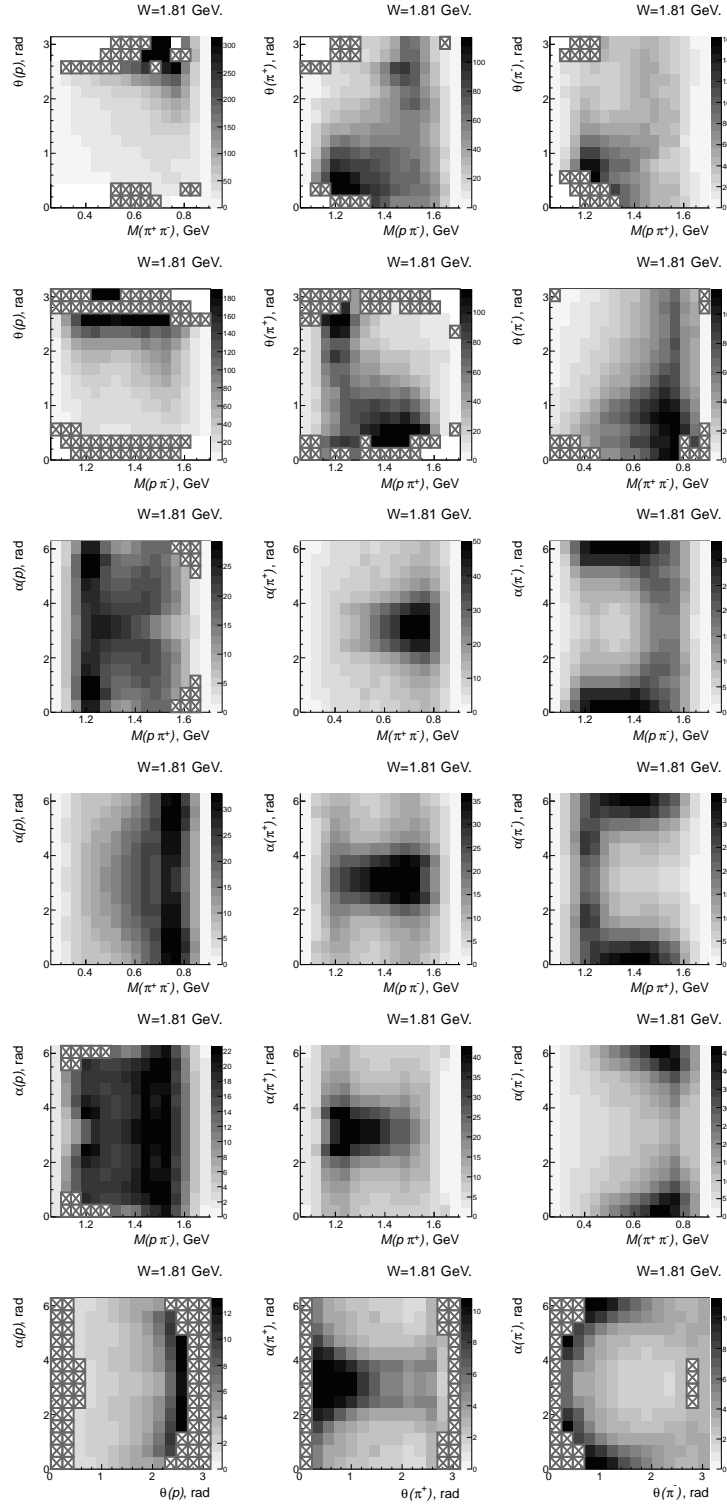


Figure 52: 2-fold differential cross sections accounted for dead area in simple approach. W-bins are marked on tops of the plots. See text for kinematics variable definitions.

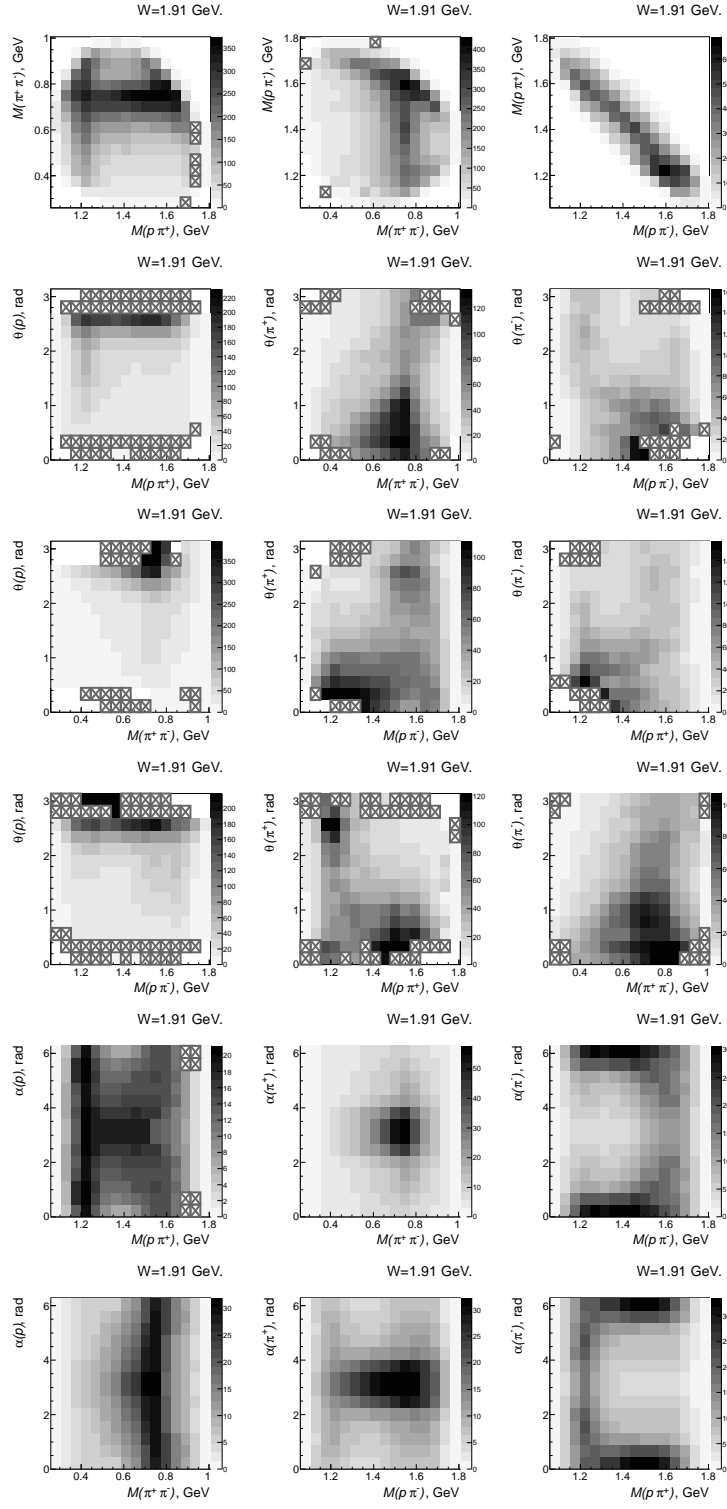


Figure 53: 2-fold differential cross sections accounted for dead area in simple approach. W-bins are marked on tops of the plots. See text for kinematics variable definitions.

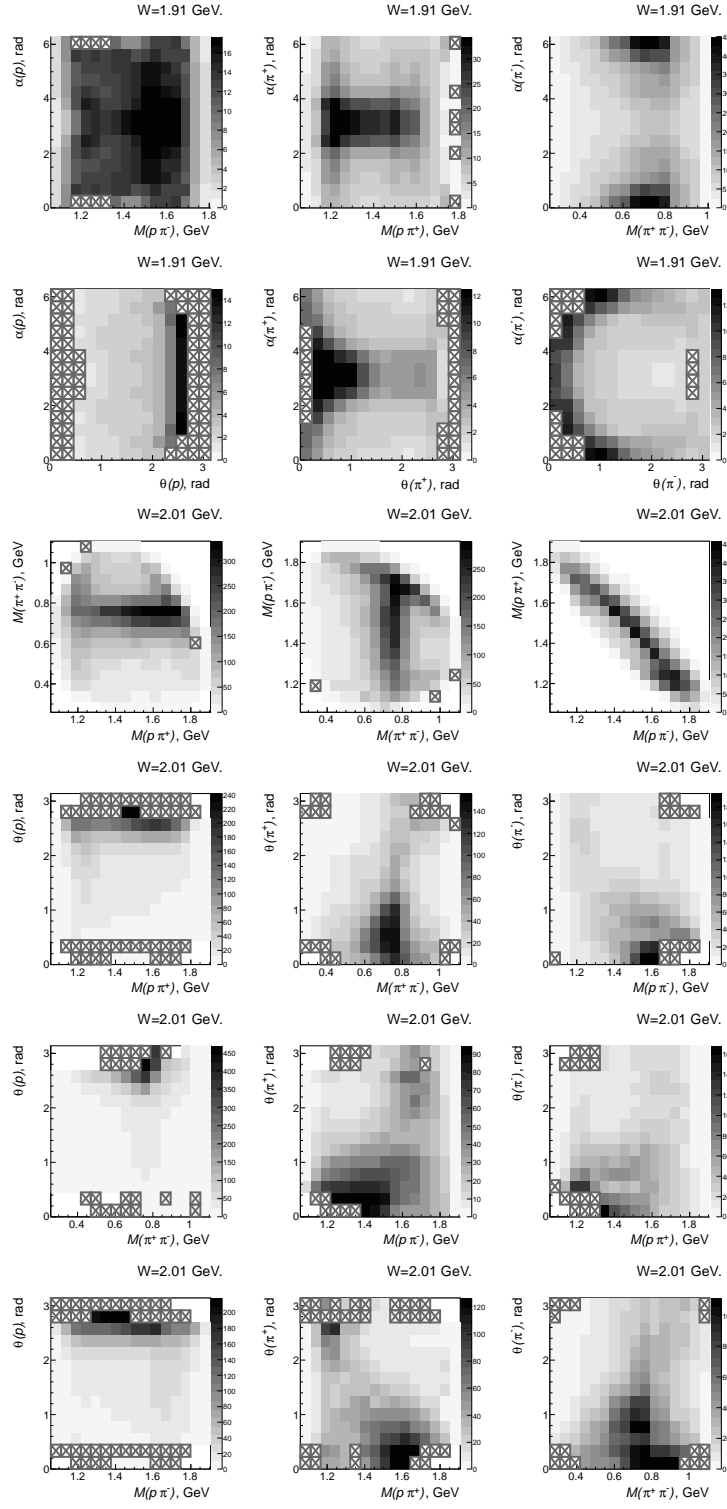


Figure 54: 2-fold differential cross sections accounted for dead area in simple approach. W-bins are marked on tops of the plots. See text for kinematics variable definitions.

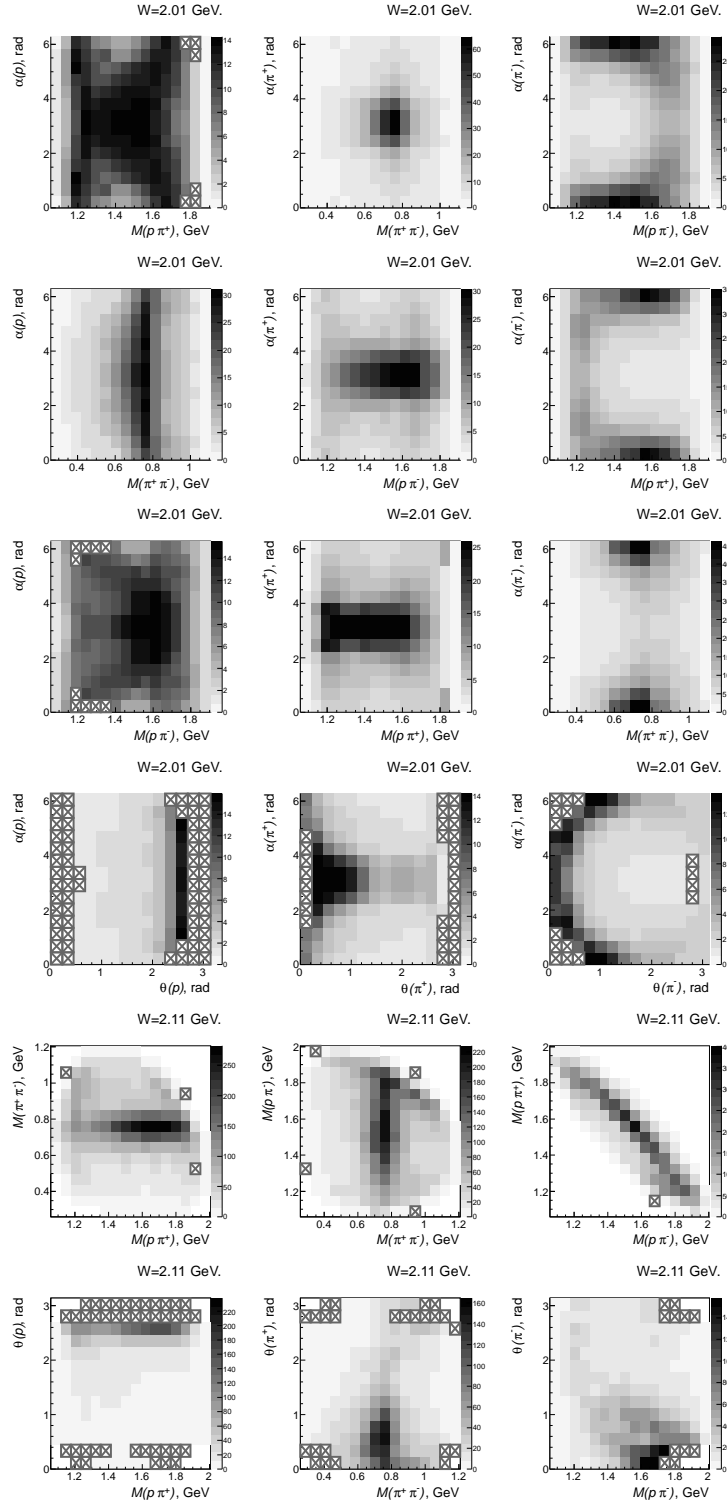


Figure 55: 2-fold differential cross sections accounted for dead area in simple approach. W-bins are marked on tops of the plots. See text for kinematics variable definitions.

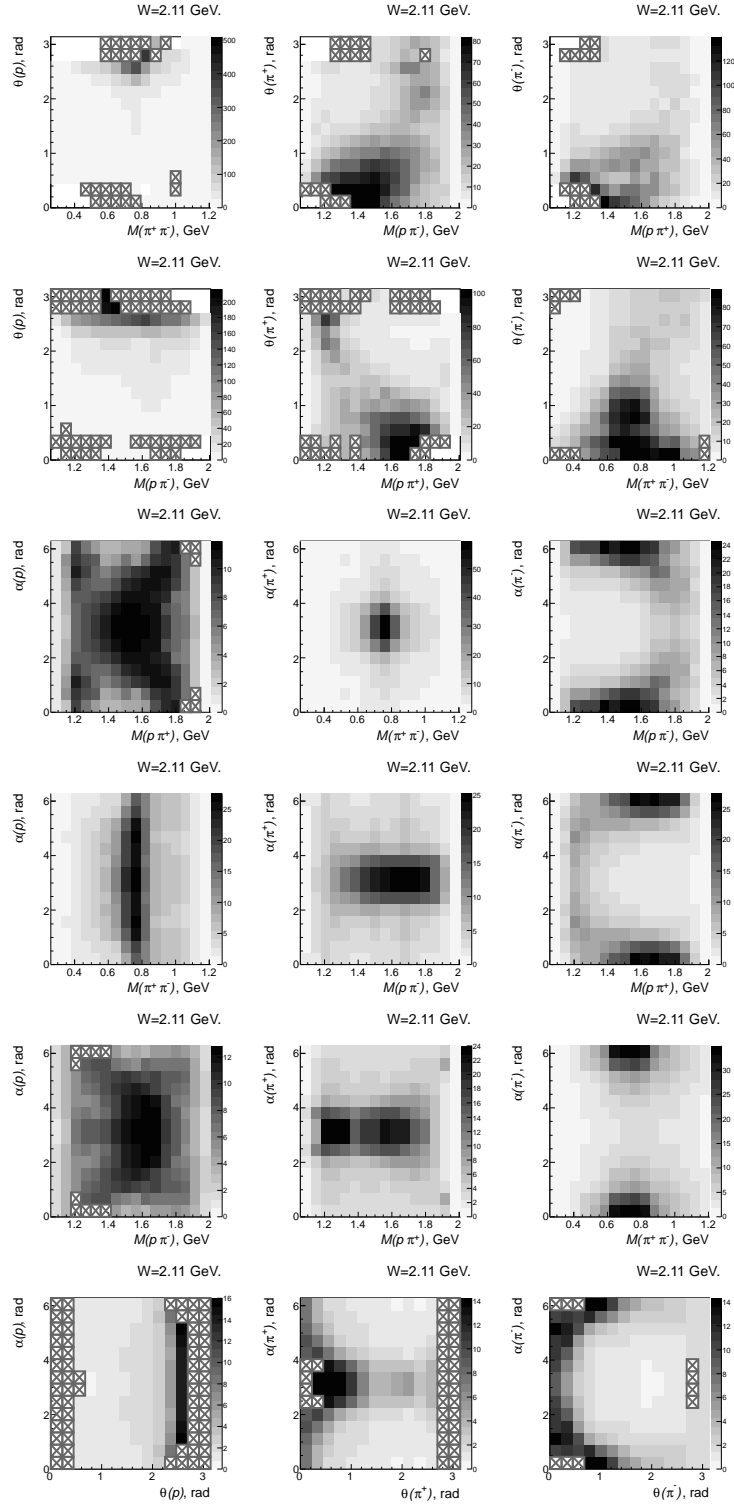


Figure 56: 2-fold differential cross sections accounted for dead area in simple approach. W-bins are marked on tops of the plots. See text for kinematics variable definitions.



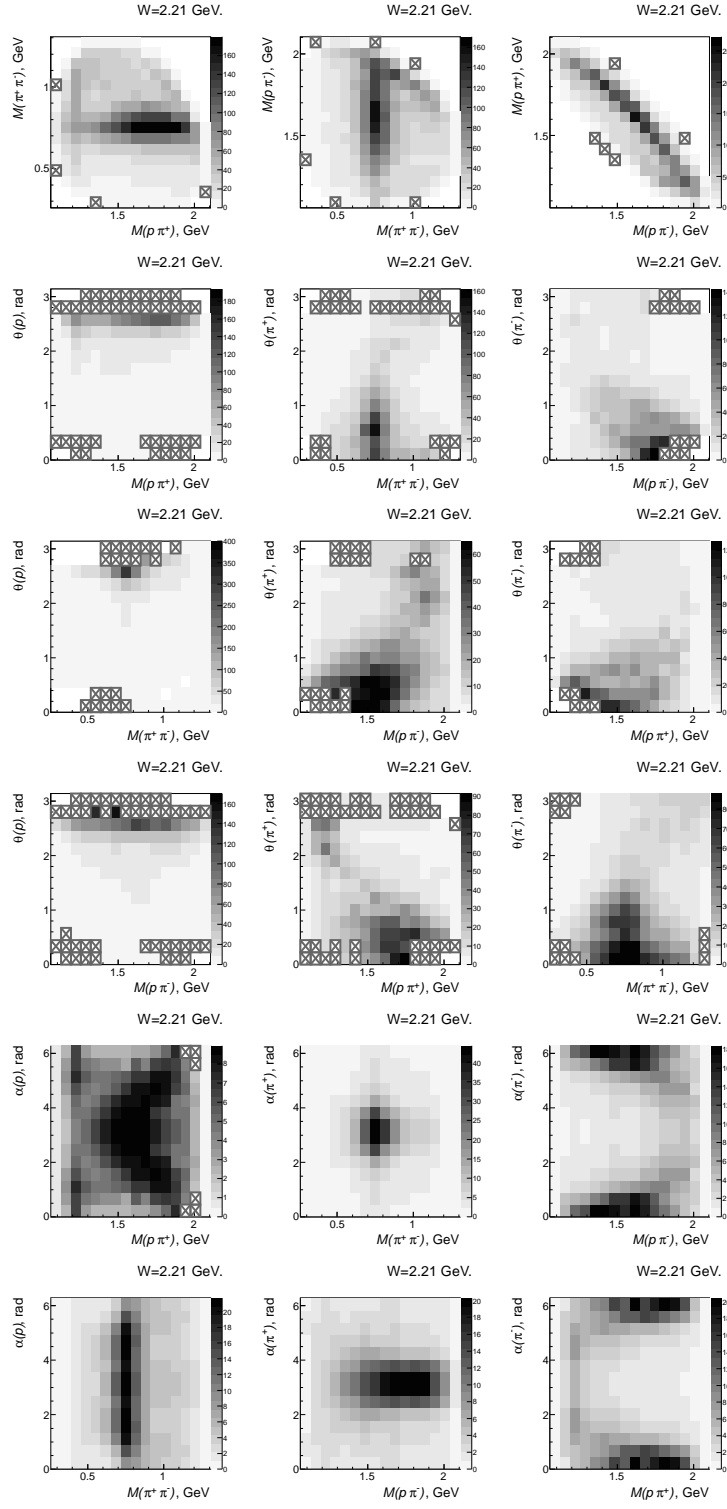


Figure 57: 2-fold differential cross sections accounted for dead area in simple approach. W-bins are marked on tops of the plots. See text for kinematics variable definitions.

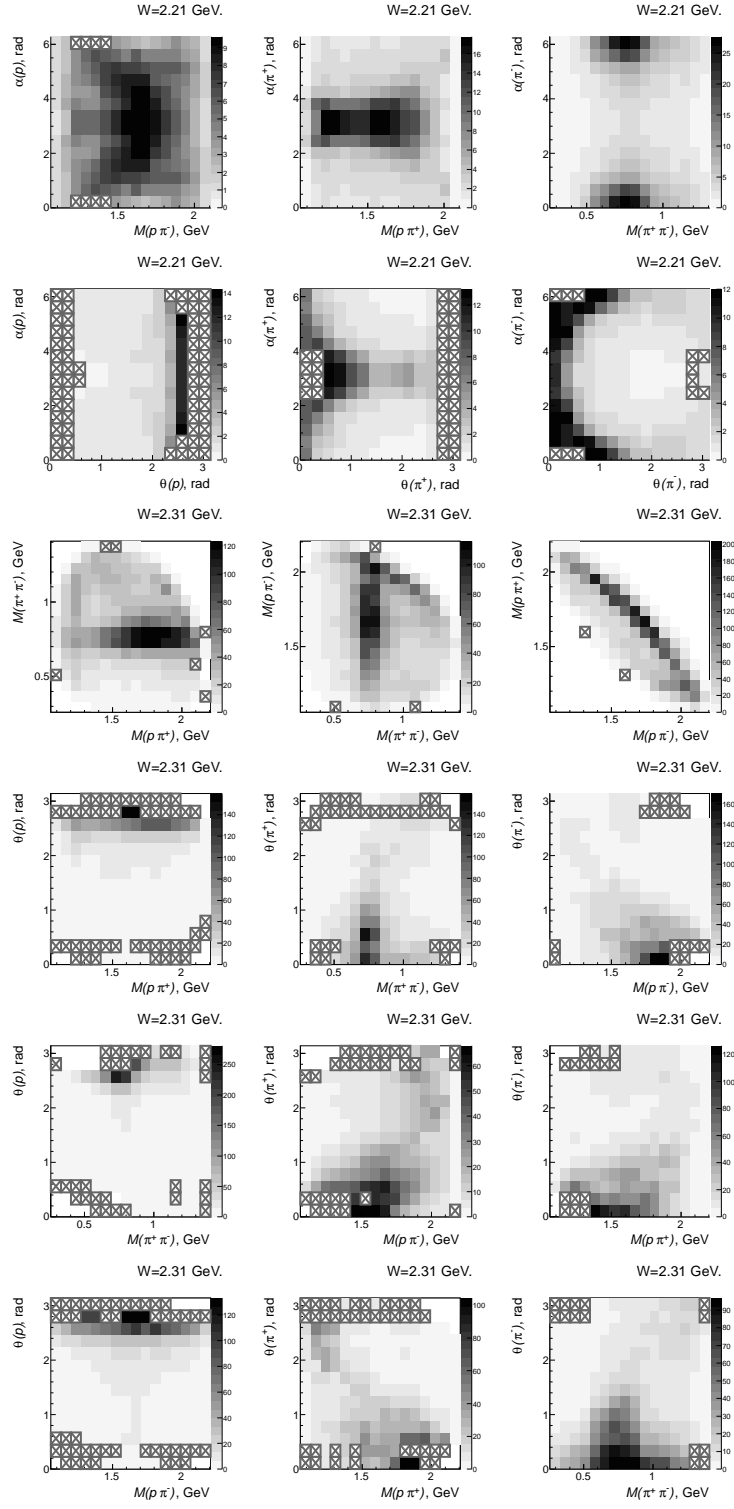


Figure 58: 2-fold differential cross sections accounted for dead area in simple approach. W-bins are marked on tops of the plots. See text for kinematics variable definitions.

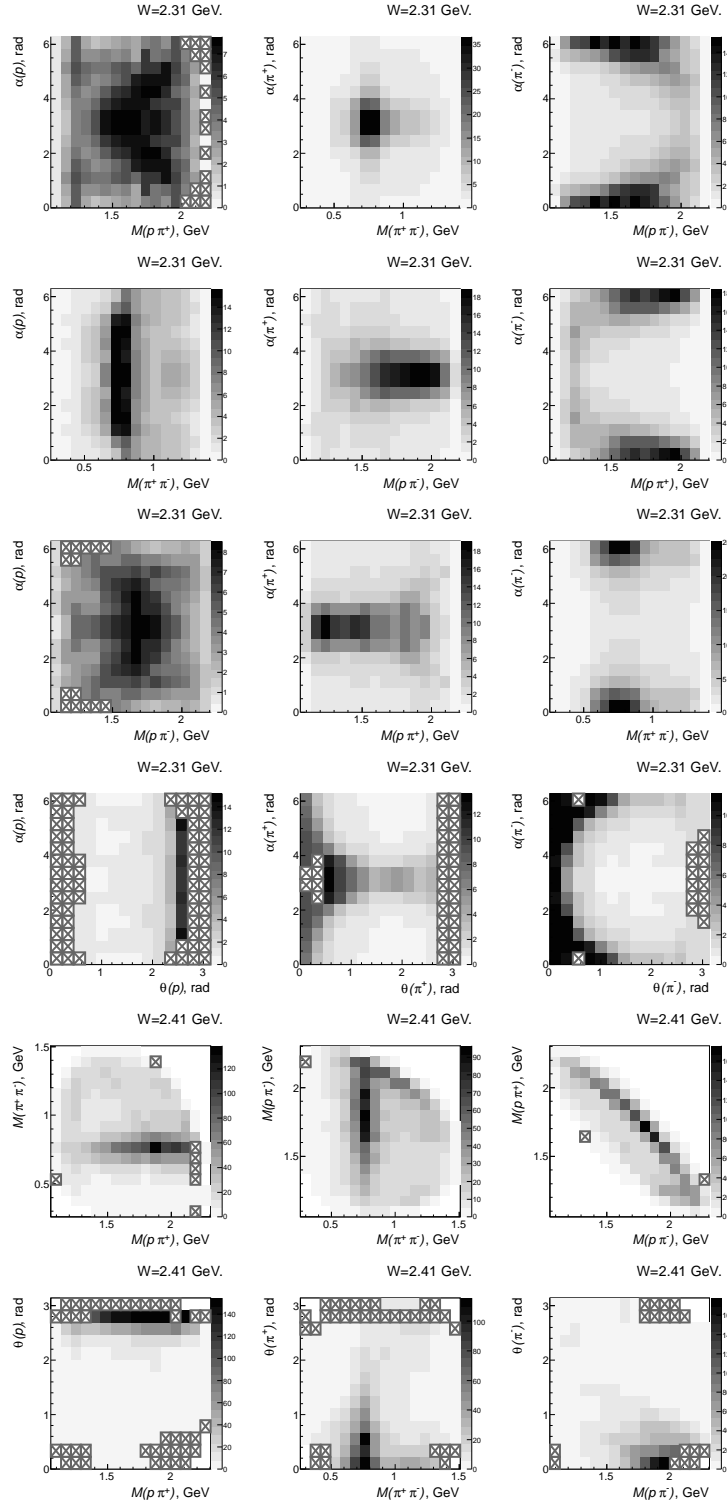


Figure 59: 2-fold differential cross sections accounted for dead area in simple approach. W-bins are marked on tops of the plots. See text for kinematics variable definitions.

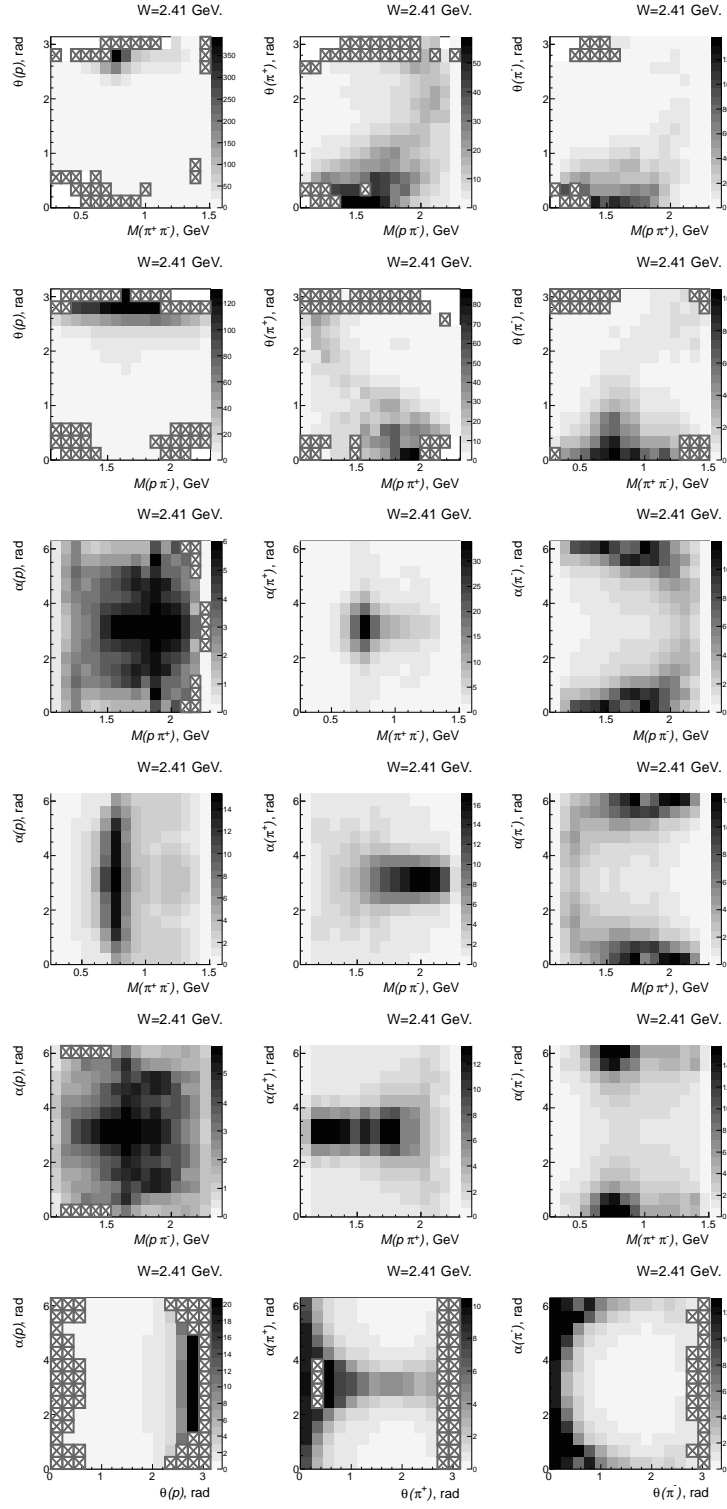


Figure 60: 2-fold differential cross sections accounted for dead area in simple approach. W-bins are marked on tops of the plots. See text for kinematics variable definitions.

# References

- [1] I. G. Aznauryan et al., J.Phys. Conf. Ser, 299, 012008 (2011).
- [2] V.D.Burkert, Int.J.Mod.Phys.Conf.Ser. 26, 1460050 (2014).
- [3] V. I. Mokeev et al., Phys. Rev.C **80**, 045212 (2009).
- [4] V. I. Mokeev et al., Phys.Rev.C **86**, 035203 (2012).
- [5] M. Ripani et al., CLAS Collaboration, Phys. Rev. Lett. **91**, 022002 (2003).
- [6] S. Capstick, N. Isgur. Phys. Rev. D34 (1986) 2809.
- [7] T.-S. H. Lee. AIP Conf. Proc. 1560, 413 (2013). arXiv:1208.5748 (2012).
- [8] M. Williams et al. CLAS-ANALYSIS 2008-102 (2008).
- [9] D. Applegate et al. CLAS-NOTE 2006-017.
- [10] M. Williams, C.A. Meyer. CLAS-NOTE 2003-017.
- [11] M. Williams, Carnegie Mellon University Ph.D. Thesis, (2007).
- [12] M. Williams, C.A. Kinematic Fitting with CLAS. CLAS-NOTE 2003-017 (2003).
- [13] <http://www-meg.phys.cmu.edu/cobra/>
- [14] E. Pasyuk. CLAS-NOTE 2007-016.kinfit2
- [15] S. Stepanyan et al. NIM A575 (2007).
- [16] M. Battaglieri, R De Vita. *The G11 hardware trigger and software reconstruction efficiency* 2006.
- [17] J. Ball, E. Pasyuk. CLAS-NOTE 2005-002.
- [18] ABBHHM Collaboration. Phys. Rev. 188, 2060 (1969).
- [19] ABBHHM Collaboration. Phys. Rev. 175, 1669 (1968).
- [20] V.I. Mokeev et al. Phys.Rev. C86 (2012) 035203.
- [21] C. Wu et al. Eur. Phys. J. A **23**, 317 (2005).